Die approbierte Originalversion dieser Dissertation ist in der Hauptbibliothek der Technischen Universität Wien aufgestellt und zugänglich.
http://www.ub.tuwien.ac.at

The approved original version of this thesis is available at the main library of the Vienna University of Technology.
http://www.ub.tuwien.ac.at/eng

TECHNISCHE
UNIVERSITÄT
WIEN
Vienna University of Technology

DISSERTATION

Encircling of exceptional points: theory and applications

Ausgeführt zum Zwecke der Erlangung des akademischen Grades

Doktor der technischen Wissenschaften

eingereicht von

Dipl. Ing. Jörg Doppler

Matrikelnummer 0625061
Vally-Weigl-Gasse 2/3/19, 1100 Wien

an der
Fakultät für Physik der Technischen Universität Wien

Betreuung:
Univ. Prof. Dipl.-Ing. Dr.techn. Stefan Rotter,
Institut für Theoretische Physik – E136

Diese Dissertation haben begutachtet:

(Prof. Dr. Stefan Rotter)

(Prof. Dr. Ziad H. Musslimani)

Wien, 25. Februar 2016

(Dipl. Ing. Jörg Doppler)

TECHNISCHE
UNIVERSITÄT
WIEN
Vienna University of Technology

DISSERTATION

Encircling of exceptional points: theory and applications

submitted in partial fulfillment of the requirements for the degree of

Doktor der technischen Wissenschaften

by

Dipl. Ing. Jörg Doppler

Registration Number 0625061
Vally-Weigl-Gasse 2/3/19, 1100 Wien

to the Faculty of Physics
at the Vienna University of Technology

Advisor:
Univ. Prof. Dipl.-Ing. Dr.techn. Stefan Rotter
Institute of Theoretical Physics – E136

The dissertation has been reviewed by:

(Prof. Dr. Stefan Rotter)

(Prof. Dr. Ziad H. Musslimani)

Wien, February 25, 2016

(Dipl. Ing. Jörg Doppler)

Erklärung zur Verfassung der Arbeit

Dipl. Ing. Jörg Doppler
Vally-Weigl-Gasse 2/3/19, 1100 Wien

Hiermit erkläre ich, dass ich diese Arbeit selbständig verfasst habe, dass ich die verwendeten Quellen und Hilfsmittel vollständig angegeben habe und dass ich die Stellen der Arbeit - einschließlich Tabellen, Karten und Abbildungen -, die anderen Werken oder dem Internet im Wortlaut oder dem Sinn nach entnommen sind, auf jeden Fall unter Angabe der Quelle als Entlehnung kenntlich gemacht habe.

(Ort, Datum)	(Unterschrift Dipl. Ing. Jörg Doppler)

Kurzfassung

Exceptional points (EPs) bezeichnen Entartungen, die im Spektrum von nichthermiteschen Hamilton Operatoren auftreten und die in letzter Zeit für einiges an Aufsehen gesorgt haben, da sie für viele faszinierende und kontraintuitive Phänomene verantwortlich sind.

Einer der wohl verblüffendsten Effekte in diesem Zusammenhang tritt auf, wenn ein EP mittels einer zeitlichen Variation der Systemparameter dynamisch umrundet wird. Dies führt zu einem chiralen Verhalten, bei dem der Endzustand nur durch die Umrundungsrichtung um den EP bestimmt wird. Trotz erheblichem Forschungsaufwand und einer Vielzahl an praktischen Anwendungsmöglichkeiten konnte solch ein Protokoll jedoch noch nicht erfolgreich in einem Experiment umgesetzt werden, da die experimentelle Implementierung sehr anspruchsvoll ist.

In der vorliegenden Arbeit wird beschrieben, wie die dynamische Umrundung eines EPs auf die Transmission zweier Moden in einem randmodulierten Mikrowellen Wellenleiter übertragen werden kann, in dem sich ein räumlich variierender Absorber befindet. Dadurch erhält man einen asymmetrischen Modenselektor, der eine spezifische transversale Wellenleiter-Mode rein basierend auf der Seite auswählt, von der aus die Wellen in den Wellenleiter eingespeist werden. Die obige Vorgehensweise ermöglicht uns, in Zusammenarbeit mit Kollegen der Universität Nizza, nicht nur die erste experimentelle Realisierung einer dynamischen EP Umrundung, sondern dient auch als Machbarkeitsnachweis für spezifische Anwendungen, wie zum Beispiel der Verallgemeinerung der weit verbreiteten "Rapid Adiabatic Passage" Technik.

Weiters zeigen wir mit numerischen Simulationen und mit analytischen Mitteln, wie neuartige Reflexionsresonanzen den Transport in Wellenleitern mit Oberflächenrauhigkeit entscheidend beeinflussen können. Diese Resonanzen führen zu einer um Größenordnungen verstärkten Rückstreuung und sind deshalb von besonderem Interesse, um Wellenleiter mit spezifischen Transporteigenschaften zu konstruieren.

Abstract

Exceptional points (EPs), degeneracies arising in the spectrum of non-Hermitian Hamiltonians, have attracted considerable attention in the physics community since they are the source of many fascinating and counter-intuitive phenomena.

One of the most intriguing effects inherent to EPs is predicted when such a degeneracy is dynamically encircled by way of a smooth temporal variation of the system's parameters, leading to a chiral behavior for which the final state is solely determined by the direction one chooses for the round-trip. However, despite a substantial research effort and the prospect for interesting practical applications, an experiment implementing this protocol was not yet realized due to the challenging experimental requirements that are involved in a successful demonstration of this effect.

In this thesis, we describe how to map the temporal dynamics in the encircling of an EP onto the transmission of two modes in a boundary modulated microwave waveguide featuring a spatially varying absorber. We thereby obtain an asymmetric mode-switching device that selects a specific transverse waveguide mode based on the direction in which the waves are injected into this waveguide. In collaboration with our colleagues from Nice University, our research not only lead to the first experimental realization of a dynamical EP encircling, but also provides proof of our concept's potential for applications, and may be seen as a generalization of already existing switching protocols like the rapid adiabatic passage technique.

Furthermore, we provide numerical as well as analytical evidence for novel reflection resonances occurring in surface-corrugated waveguides. These resonances lead to an order-of-magnitude enhancement of the waveguide's reflectance and are of special interest for imprinting specific transport properties onto a waveguide.

Contents

1 Introduction **1**

2 Exceptional points **4**

2.1 Hamiltonian 5

2.2 Eigenvector flip 7

2.3 Asymmetric mode-switching 9

2.4 Quasi-adiabatic dynamics and stability-loss delay 10

3 Dynamically encircling EPs in waveguides **15**

3.1 Model 16

3.2 2×2 model 17

3.2.1 Loop parametrization 18

3.2.2 Parametrical vs. dynamical encircling 21

3.2.3 Bulk absorption 25

3.2.4 Position dependent absorption 26

3.3 2D waveguide simulations 32

3.3.1 Backscattering resonances 32

3.3.2 Rapid adiabatic passage 34

3.3.3 Method 35

3.3.4 Results 35

3.3.4.1 Unoptimized waveguide 35

3.3.4.2 Length optimization 38

3.3.4.3 Absorber optimization 40

3.4 Microwave experiment 43
3.4.1 Setup 44
3.4.2 Results 44
3.5 Breaking of reciprocity? 45
3.6 Rabi oscillations 46

4 Reflection resonances in surface-disordered waveguides 49
4.1 Introduction 49
4.2 Model 53
4.3 Analytical method 54
4.4 Numerical method 60
4.5 Comparison between analytical and numerical results 62
4.5.1 Symmetric profiles 62
4.5.2 Antisymmetric profiles 66
4.5.3 Nonsymmetric profiles 73

5 Surface scattering and band gaps in rough waveguides 77
5.1 Strategy 78
5.2 Results 79

6 Conclusion and outlook 82

A Effective 2×2 model derivation 84
A.1 Model 84
A.2 Floquet-Bloch picture 84
A.3 Perturbative approach 86
A.4 Effective 2×2 model 89
A.5 Non-uniform absorption 89
A.6 EP structure 91

B Transitionless quantum driving 92
B.1 Effective model 92

B.2 Transitionless quantum driving 93
B.3 Implementation 93

C Square-gradient scattering from step boundaries 95
C.1 Step-profile $\xi(x)$ 95
C.2 Roughness-height power spectrum $W(k)$ 96
C.3 Square-gradient power spectrum $S(k)$ 98

Bibliography 100

List of Acronyms

AGS	Amplitude-gradient scattering
DP	Diabolical point
EP	Exceptional point
MRGM	Modular recursive Green's function method
PT	Parity-time
RAP	Rapid adiabatic passage
SGS	Square-gradient scattering
STIRAP	Stimulated rapid adiabatic passage
TQD	Transitionless quantum driving

CHAPTER 1

Introduction

In the analysis of states in closed systems, the corresponding real eigenfrequencies and orthogonal eigenmodes are determined from a Hermitian operator or matrix. More realistic descriptions, in which the coupling to additional degrees of freedom is effectively taken into account by employing the concepts of gain and/or loss, however, render the system non-Hermitian: As a consequence, the eigenfrequencies are now complex such that they obtain a finite width, and the corresponding modes cease to be orthogonal [1–4].

Especially intriguing in this context are so-called exceptional points (EPs), which are singularities in the system's complex eigenvalue spectrum where two eigenvalues and their corresponding eigenvectors coalesce, and which are directly related the system's non-Hermiticity. At or close to an EP, several interesting phenomena have been identified that are contrary to physical intuition, like, e.g., lasers that are switched off even though the system is pumped more strongly [5, 6], loss-induced transparency in coupled waveguides [7] or the realization of unidirectional invisibility in gratings with gain and loss [8]. It thus comes as no surprise that EPs have attracted much attention in the physics community (see, e.g., Refs. [4, 9–11] and references therein).

In this thesis we study an effect which is closely related to the specific topological structure near the exceptional point, realized by a self-intersecting Riemann sheet. Reasoning based on the adiabatic theorem [12] would suggest a symmetric switching behavior upon a parametrical round-trip around an EP, i.e., if encircled slowly enough, a state-exchange would occur provided the adiabatic theorem were true also in the presence of loss and gain, which would have many applications ranging from switching to vibrational cooling [13–15]. As it turns out, however, the non-Hermiticity defies the quantum adiabatic theorem and prohibits the usage of many tools that are conventionally used in conservative systems [16–21]. As a result, one observes chiral behavior, in the sense that the encircling-direction alone specifies in which state the system arrives at the end of the evolution. While such an effect offers broad applicability, e.g., for generalized switching protocols like the rapid adiabatic passage, an experiment that *dynamically* cycles an EP has not yet been put forward, despite considerable research effort [22, 23]

In the main part of this thesis, we derive how this peculiar dynamical feature can be transferred onto wave transport in dissipative two-mode waveguides featuring modulated boundaries. Although the hypothesized (adiabatic) state-exchange is not realized due to non-adiabatic transitions inherent to open systems, we exploit the EP encircling such as to obtain a chiral behavior that allows a mode selection based on the direction of the incident wave. More precisely, dependent on which end of the waveguide the system is excited, either one or the other of two propagating modes in the system is strongly suppressed, leading to an asymmetric mode-switch with considerable potential for very practical applications.

In the second part of this thesis, we show that the current state-of-the-art scattering theory for boundary-modulated waveguides fails to provide an accurate picture even for simpler, Hermitian systems: In particular, one might expect that the problem of surface scattering in boundary-modulated waveguides is already thoroughly understood. Most surprisingly, however, we show that already existing techniques do not correctly describe wave transport even in this context. To illustrate the deficiency of presently established techniques, we investigate the transmission of waves through surface-disordered waveguides with a step-like surface profile - a situation that is well studied in the literature [24–27]. Using numerical as well as analytical techniques, we observe resonant enhancements of the reflection in this system, which are due to higher-order effects in the disorder that were previously neglected in earlier studies of the same setup. These reflection resonances, which are very robust and pronounced in their amplitudes, thus provide clear evidence for the incompleteness of conventional techniques and a test case for extending these techniques to include the missing higher-order terms. For the systems at hand we manage to provide these terms fully analytically, such that we can also formulate a condition for the resonances to appear. With these expressions we find quantitative agreement between numerical and analytical results, thereby laying the groundwork for a comprehensive understanding of wave transmission through waveguides with surface disorder [28].

Our results are of particular importance for the engineering of waveguides with predetermined transmission characteristics based on the design of their surface profiles [29]. Ultimately, our approach may provide essential corrections to all the many different scenarios in which surface scattering plays a key role.

CHAPTER 2

Exceptional points

Exceptional points (EPs), also termed non-Hermitian degeneracies or branch points, have recently attracted considerable attention. This is because these singular points have turned out to be at the origin of many counter-intuitive phenomena appearing in physical systems that experience gain or loss [4, 9–11, 30, 31]. Such external influences on a system require a non-Hermitian description that incorporates non-conservation of energy resulting from this external in- or output. Rather than being merely a perturbative correction, gain and loss can entirely turn the behavior of a system upside down when approaching an EP. Consider here, e.g., the recent demonstrations of unidirectional invisibility [8, 32–34], loss-induced suppression and revival of lasing [6, 35], and single-mode lasers with gain and loss [36, 37], all of which were realized at or close to an EP. While these studies already nicely demonstrate the potential of EPs for novel effects and devices, their full capability can be brought to bear when the EP is not just approached or swept across, but parametrically encircled [14, 15]. Originally, it was believed that a slow encircling of an EP would result in an adiabatic evolution of states and a corresponding state flip [13], but more recent work has rigorously shown that the very same non-Hermitian components necessary for the observation of an EP actually prevent an application of the adiabatic theorem [17–19, 21, 38–42]. Instead, as we show below, the non-adiabatic terms lead to a chiral behavior, in the sense that encircling an EP in a clockwise and a counter-clockwise direction results in different final states [19].

2.1 Hamiltonian

An EP arises when an open system described by a Schrödinger-type equation $i\partial_t\psi = H\psi$ features two resonant modes that coalesce. Such a scenario can conveniently be captured already by the following non-Hermitian 2×2 Hamiltonian,

$$H = \begin{pmatrix} \delta - i\gamma_1/2 & g \\ g & -i\gamma_2/2 \end{pmatrix} \tag{2.1}$$

where g denotes the coupling and δ the detuning between the two modes, γ_1 and γ_2 are the respective loss rates. Evidently, the above operator is non-Hermitian, i.e., $H \neq H^\dagger$, and the eigenvalue spectrum $E_{1,2}$ is thus not guaranteed to be real,

$$E_{1,2} = \frac{\delta}{2} - i\frac{\gamma_1 + \gamma_2}{4} \pm \frac{1}{2}\sqrt{\Delta}\,, \quad \Delta \equiv \left(\delta - i\frac{\gamma_1 - \gamma_2}{2}\right)^2 + 4g^2\,. \tag{2.2}$$

Additionally, we have for the eigenvectors

$$\Phi_1 = \begin{pmatrix} \cos\frac{\theta}{2} \\ \sin\frac{\theta}{2} \end{pmatrix}\,, \quad \Phi_2 = \begin{pmatrix} -\sin\frac{\theta}{2} \\ \cos\frac{\theta}{2} \end{pmatrix}\,, \tag{2.3}$$

$$\tan\frac{\theta}{2} = \frac{g}{E_1 + i\gamma_2/2}\,, \tag{2.4}$$

satisfying the corresponding eigenvalue equation $H\Phi_{1,2} = E_{1,2}\Phi_{1,2}$. This allows us to diagonalize the Hamiltonian, $H = XDX^{-1}$, with $D = \mathrm{diag}(E_1, E_2)$ and $X = (\Phi_1, \Phi_2)$.

An exceptional point is characterized by the vanishing of the discriminant Δ, i.e., both the real and imaginary part of Δ have to simultaneously satisfy

$$\mathrm{Re}\Delta = 0 \quad \text{and} \quad \mathrm{Im}\Delta = 0\,, \tag{2.5}$$

yielding the EP at the specific parameter configuration

$$\begin{aligned} g_{\mathrm{EP}} &= \pm\frac{|\gamma_1-\gamma_2|}{4} \\ \delta_{\mathrm{EP}} &= 0\,. \end{aligned} \tag{2.6}$$

If $\gamma_1 \neq \gamma_2$, there is then a single eigenvalue $E_{\mathrm{EP}} = -i\frac{\gamma_1+\gamma_2}{2}$ and eigenvector $\Phi_{\mathrm{EP}} = (1, \pm i)^T$. Thus, both the eigenvalues $E_{1,2}$ and the eigenvectors $\Phi_{1,2}$ coalesce and render the Hamiltonian (2.1) defective, which property is the hallmark of the EP (note that the sign ± stems from the fact that the Hamiltonian (2.1) supports two parameter configurations directly at which an EP emerges).

We might add that, although the specific nomenclature "exceptional point" was coined in the 1960s by T. Kato [43], the non-diagonalizability of a matrix has been known already for a very long time and is not specific to non-Hermitian systems. Whereas directly at the EP, H becomes defective and does no longer support diagonalization, it is still possible to express H by a (Jordan) block-diagonal matrix J via the similarity transformation $H = PJP^{-1}$ [44,45], with $P = (\Phi_{\mathrm{EP}}, h_{\mathrm{EP}})$ being composed of the eigenvector Φ_{EP} and the generalized eigenvector h_{EP}, and the block-diagonal matrix

$$J = \begin{pmatrix} E_{\mathrm{EP}} & 1 \\ 0 & E_{\mathrm{EP}} \end{pmatrix}\,. \tag{2.7}$$

In Fig. 2.1 we show the eigenvalue spectrum $\mathrm{Re}E_{1,2}$ and $\mathrm{Im}E_{1,2}$ as a function of the two parameters g and δ, producing the intricate topology of a square-root branch point in the center of each figure [11]. Physically, the self-intersecting Riemann surface corresponds to an avoided or anti-crossing of the energies $\mathrm{Re}E_{1,2}$ for values $g > g_{\mathrm{EP}}$, and a crossing for $g < g_{\mathrm{EP}}$, if $\delta = \delta_{EP}$. Remarkably, the widths $\mathrm{Im}E_{1,2}$ show the exact opposite behavior: Here, we find a crossing of widths for $g > g_{\mathrm{EP}}$, and an anti-crossing for $g < g_{\mathrm{EP}}$, if δ is fixed to δ_{EP}. For completeness we note that in the context of parity-time ($\mathcal{PT}$) symmetry, the EP represents the point which separates the $\mathcal{PT}$-broken and unbroken phases [11,30].

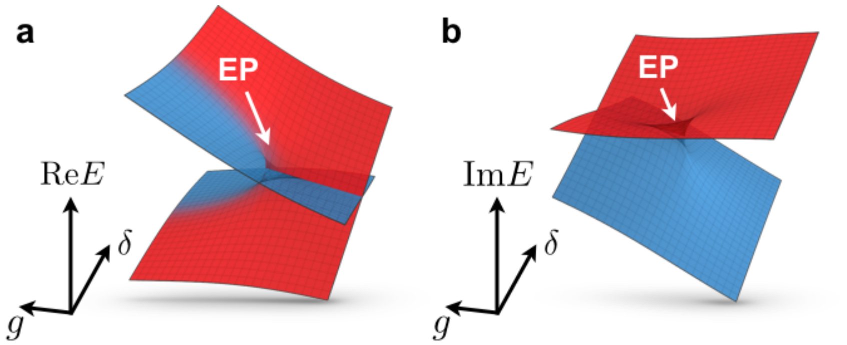

Figure 2.1: Parameter-dependent eigenvalue spectrum obtained in the vicinity of an exceptional point (indicated by white arrows). Both the real and imaginary part is shown in panels a and b, respectively. The coloring is chosen such that red (blue) corresponds to an eigenvalue with relative gain (loss).

2.2 Eigenvector flip

It is the specific topological structure of the eigenvalue surfaces shown above that allows one to encircle the EP such that the two eigenvectors interchange: For such a state-flip two system parameters need to be changed in time t (e.g., the coupling $g = g(t)$ and the detuning $\delta = \delta(t)$) along a closed loop in parameter space around the EP. This system evolution is described by the now time-dependent Hamiltonian (2.1) in the corresponding Schrödinger-type equation $i\partial_t\psi(t) = H(t)\psi(t)$.

To illustrate such a state-flip, we parametrize g and δ as follows to encircle the EP:

$$\begin{aligned} g(t) &= g_{\mathrm{EP}} + r\cos\phi(t) \\ \delta(t) &= 2r\sin\phi(t)\ , \end{aligned} \tag{2.8}$$

with $\phi(t) \in [0, 2\pi)$, resulting for small radii in

$$E_{1,2} \approx r\sin\phi(t) - i\frac{\gamma_1+\gamma_2}{4} \pm \frac{i}{2}\sqrt{r g_{\mathrm{EP}}}e^{i\phi(t)/2}\ . \tag{2.9}$$

Due to the $\exp(i\phi(t)/2)$ term we have a switching of eigenvalues $E_{1,2} \to E_{2,1}$ for phase transformations originating from a full EP encircling

$$\phi(t) \to \phi(t) \pm 2\pi\ , \tag{2.10}$$

where the sign ± corresponds to the encircling direction. For the tangent of the mixing-angle (2.4) we obtain

$$\tan\frac{\theta}{2} \approx -i + 2\frac{\sqrt{2r}}{\sqrt{\gamma_2-\gamma_1}}e^{i\phi(t)/2}\;, \tag{2.11}$$

such that we finally have [46]

$$\mathrm{Re}\,\frac{\theta}{2} \approx \frac{\pi}{4} - \frac{\phi(t)}{4}\;. \tag{2.12}$$

An EP round-trip $\phi \to \phi \pm 2\pi$ for encircling directions $\circlearrowleft$ and $\circlearrowright$ therefore yields

$$\frac{\theta}{2} \to \frac{\theta}{2} \mp \frac{\pi}{2}\;. \tag{2.13}$$

Consequently, the eigenvectors Φ_i show a more intricate behavior while traversing the loop due to the appearance of a geometric phase of π [47] ,

$$\circlearrowleft\!: \begin{pmatrix}\Phi_1\\ \Phi_2\end{pmatrix} \to \begin{pmatrix}\Phi_2\\ -\Phi_1\end{pmatrix}\;,\quad \circlearrowright\!: \begin{pmatrix}\Phi_1\\ \Phi_2\end{pmatrix} \to \begin{pmatrix}-\Phi_2\\ \Phi_1\end{pmatrix}\;. \tag{2.14}$$

Only after 4 consecutive loops around the EP the original order of eigenvectors is restored [22,46,47]:

$$\begin{pmatrix}\Phi_1\\ \Phi_2\end{pmatrix} \circlearrowleft \begin{pmatrix}\Phi_2\\ -\Phi_1\end{pmatrix} \circlearrowleft \begin{pmatrix}-\Phi_1\\ -\Phi_2\end{pmatrix} \circlearrowleft \begin{pmatrix}-\Phi_2\\ \Phi_1\end{pmatrix} \circlearrowleft \begin{pmatrix}\Phi_1\\ \Phi_2\end{pmatrix}\;, \tag{2.15}$$

and

$$\begin{pmatrix}\Phi_1\\ \Phi_2\end{pmatrix} \circlearrowright \begin{pmatrix}-\Phi_2\\ \Phi_1\end{pmatrix} \circlearrowright \begin{pmatrix}-\Phi_1\\ -\Phi_2\end{pmatrix} \circlearrowright \begin{pmatrix}\Phi_2\\ -\Phi_1\end{pmatrix} \circlearrowright \begin{pmatrix}\Phi_1\\ \Phi_2\end{pmatrix}\;, \tag{2.16}$$

where we have used the shorthand notation

$$a \underset{\circlearrowright}{\overset{\circlearrowleft}{\ }} b \equiv \underset{\circlearrowright}{\overset{\circlearrowleft}{\ }} : a \to b \tag{2.17}$$

that was introduced in Ref. [22] for brevity.

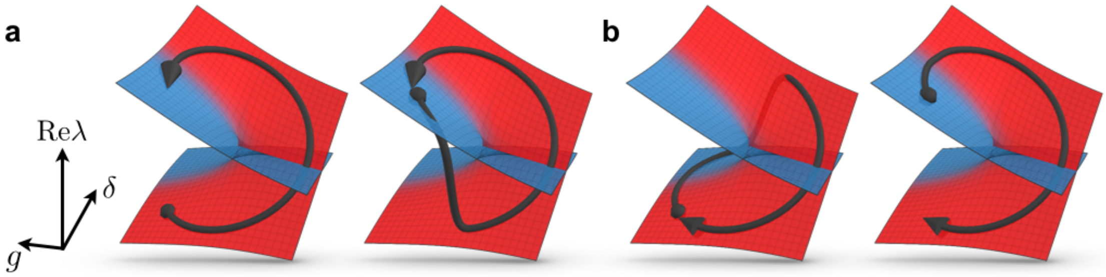

Figure 2.2: To demonstrate the non-adiabatic nature of dynamically encircling an EP degeneracy, we show trajectories with different encircling directions, starting on opposing parts of the self-intersecting Riemann sheet (shown as red and blue surfaces). The results for the state evolution of the Schrödinger-type equation $i\partial_x\psi(x) = H(x)\psi(x)$, projected onto their respective Riemann sheets are shown as black lines: the larger the contribution of an eigenvector, the closer it follows the corresponding eigensheet. **a**, The dynamics of two states with starting points on different sheets during a counter-clockwise loop around the EP (as seen from the top). **b**, Same as in **a** for a clockwise loop. In both **a** and **b** the end points of the loops depend only on the encircling direction, not on their starting point.

2.3 Asymmetric mode-switching

Thus, if the system dynamics is fully adiabatic, a flip between the two states is realized upon encircling the EP such that the lower state becomes the upper one (Fig. 2.2a left).

As was found only recently [17], however, contributions due to the breakdown of adiabaticity in non-Hermitian systems always enter dominantly whenever both encircling directions are considered: In the case above, traversing the same parameter loop in the opposite direction thus leads to the situation that the lower state returns to itself rather than to the upper state (Fig. 2.2b left). This enforces an overall asymmetric behavior such that the state that is selected at the end of a loop depends only on the loop's encircling direction, but not on its starting point - compare here Fig. 2.2a and 2.2b for a counter-clockwise and clockwise encircling, respectively. This opens the door to engineer a device which yields a specific system state, depending only on the direction in which the EP is encircled (see section 3.2.2 for a more elaborate treatment of the difference between parametrical and dynamical encircling).

2.4 Quasi-adiabatic dynamics and stability-loss delay

On a very fundamental level, the above features are connected to deep-rooted mathematical concepts: One is the Stokes phenomenon of asymptotics [39, 40] and, as we showed in a joint work with Thomas J. Milburn and Peter Rabl, as well as Stefano Portolan and Catherine A. Holmes, another one is the theory of singular perturbations [41]. For the results presented therein, I have contributed numerical simulations and participated in the discussion of both the theoretical and the numerical data.

To review the main points of this joint work, I will give here a very basic introduction to the concept of stability loss delay that allows an intuitive understanding of the chiral behavior found in EP encirclings. For details and in-depth derivations, see Ref. [41].

A convenient starting point is to transform the Schrödinger equation $i\partial_t\psi(t) = H(t)\psi(t)$, with the Hamiltonian Eq. (2.1), using $\psi \to \tilde{U}\tilde{\psi}$, with

$$\tilde{U} = e^{-i\int_0^t \operatorname{tr} H(t')/2 \, \mathrm{d}t'} \; , \quad \operatorname{tr} H(t') = \delta(t') - \frac{i}{2}\left(\gamma_1 + \gamma_2\right) \; , \tag{2.18}$$

such that we arrive at the following dynamical equation with the traceless Hamiltonian $\tilde{H}$,

$$i\partial_t\tilde{\psi} = \tilde{H}\tilde{\psi} \; , \quad \tilde{H} = \begin{pmatrix} \tilde{\delta} + i\tilde{\gamma}/2 & g \\ g & -\tilde{\delta} - i\tilde{\gamma}/2 \end{pmatrix} \; , \tag{2.19}$$

which will be more convenient in the following. Here, we have introduced $\tilde{\delta} = \delta/2$ and $\tilde{\gamma} = (\gamma_1 - \gamma_2)/2$, and $\tilde{\psi} = (\tilde{c}_1, \tilde{c}_2)^T$ corresponds to the amplitudes. For the sake of simplicity, and for complying with the notation introduced in Ref. [41], we will from here on remove the tilde from the variable names. Thus, the eigenvalues are given by $\lambda_\pm = \pm\lambda = \pm\sqrt{(\delta + i\gamma/2)^2 + g^2}$. We continue by transforming into the respective eigenbasis of H, and investigate the equation of motion for the evolution operator U, defined by $\psi(t) = U(t)\psi(0)$,

$$\dot{U}(t) = -i \begin{pmatrix} -\lambda(t) & f(t) \\ f(t) & \lambda(t) \end{pmatrix} U(t) \ , \quad U = \begin{pmatrix} U_{-,-} & U_{-,+} \\ U_{+,-} & U_{+,+} \end{pmatrix} \ , \tag{2.20}$$

with $U(0) = \mathbb{1}$. This representation allows us to conveniently read off the non-adiabatic contributions to the system's evolution, $f(t)$, given by

$$f(t) = \frac{g(t)\Big(\dot{\delta}(t) + i\dot{\gamma}(t)/2\Big) - \Big(\delta(t) + i\gamma(t)/2\Big)\dot{g}(t)}{2i\lambda^2(t)} \ . \tag{2.21}$$

From Eq. (2.20) one might argue that for

$$\epsilon := |f(t)/2\lambda(t)| \ll 1 \ , \tag{2.22}$$

achievable by increasing the duration of the evolution T, i.e., $f \propto 1/T$, the off-diagonals can be neglected and the evolution operator becomes diagonal, yielding the adiabatic solution

$$U^{\mathrm{ad}}(t) = \begin{pmatrix} e^{i\int_0^t \lambda(t')\mathrm{d}t'} & 0 \\ 0 & e^{-i\int_0^t \lambda(t')\mathrm{d}t'} \end{pmatrix} \ . \tag{2.23}$$

The above adiabatic dynamics are however only realized if $f(t) = 0$. For finite, yet small, non-adiabatic contributions the full dynamics cannot be obtained by means of a perturbative correction to U^{ad}, since the problem is *singularly perturbed* [48]. Due to this property, it is more appropriate to call $\epsilon \ll 1$ the *quasi-adiabatic* condition.

We continue by building the non-adiabatic transition amplitudes

$$R_-(t) := \frac{U_{+,-}(t)}{U_{-,-}(t)} \ , \quad R_+(t) := \frac{U_{-,+}(t)}{U_{+,+}(t)} \ , \tag{2.24}$$

which contain the information about how much of an eigenvector's population has leaked into the other one during the course of the evolution. In an adiabatic system, such transitions can be neglected, and $R_\pm(t) \ll 1$. In contrast, dominant non-adiabatic contributions, lead to values $R_\pm(t) \gg 1$. An important insight is that the dynamical variable $R_\pm(t)$ itself satisfies the Ricatti equation

$$\dot{R}_\pm(t) = \pm 2i\lambda(t)R_\pm(t) \pm if(t)\left(1 + R_\pm^2(t)\right) , \tag{2.25}$$

with $R_\pm(0) = 0$. Without loss of generality and to keep our notation simple in the following, we can set $R(t) := R_-(t)$. All the essential dynamical features of quasi-adiabatic evolution can be inferred from Eq. (2.25) in the quasi-adiabatic limit $\epsilon \to 0$.

Looking at the dynamics of $R(t)$ in Fig. 2.3a obtained numerically for multiple consecutive encircling loops, one observes a square-wave that follows two quasi-stationary values, interrupted by rapid transitions in between. This behavior can be attributed to two time scales that are inherent to the problem: For short times both the non-adiabatic contributions f and the eigenvalues λ are slowly varying and can be assumed to be approximately constant, such that R evolves towards the two fixed points that are obtained by assuming a vanishing time derivative $\dot{R} = 0$ and solving for R,

$$R^{\text{ad}} \approx -\frac{f}{2\lambda} , \tag{2.26}$$

$$R^{\text{nad}} \approx -\frac{2\lambda}{f} . \tag{2.27}$$

These fixed points correspond to the two quasi-stationary values observed in Fig. 2.3a. It is an interesting question to ask whether these two fixed points are stable or not: Depending on the sign of λ, the adiabatic fixed point R^{ad} is stable for Im$\lambda < 0$, while the non-adiabatic fixed point R^{nad} is stable for Im$\lambda > 0$. For long times, however, the parameters $\lambda(t)$ and $f(t)$ may change considerably, such that the fixed points may change their stability. This happens exactly at critical times t_*, where the stability of the two fixed points swaps and a dynamical bifurcation occurs (see Fig. 2.3b).

Before a critical time t_*, the adiabatic solution is attracting, the non-adiabatic one is repelling; at a time t_*, we are passing a bifurcation where R^{ad} is a center and neither attracting nor repelling. For times $t > t_*$, the stability is swapped

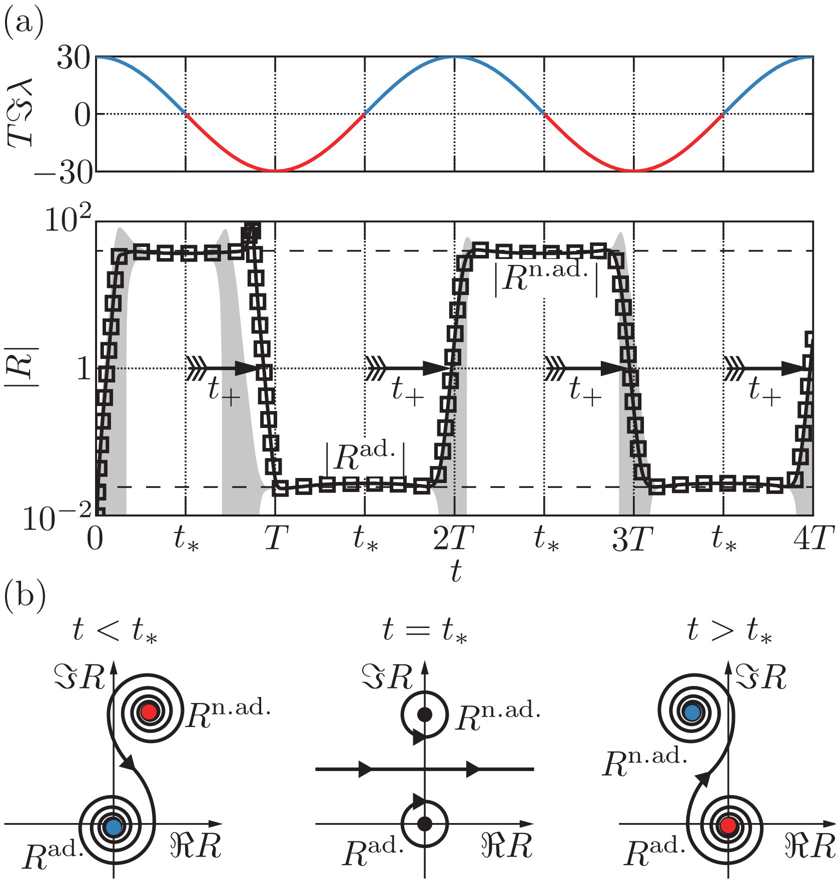

Figure 2.3: (a) Plot of $\Im\lambda(t)$ (upper panel), and a typical solution for $R \equiv R_-$ (lower panel). The solid curve is the analytic solution from Refs. [39, 40], and the squares are the numerical solution. The arrows denote delay times. The lower and upper dashed grid lines denote $|R^{\text{ad}}(t)|$ and $|R^{\text{nad}}(t)|$, respectively. The shaded area is one standard deviation about the mean of R_- obtained from $10{,}000$ stochastic numerical integrations of c_- and c_+ in the presence of noise (see Ref. [41] for more details). (b) Cartoons of the phase portraits of the equation of motion for R near t_*. Arrows denote the direction of time-evolution along an integral curve. The fixed point near the origin corresponds to $R^{\text{ad}}(t)$, and the fixed point far from the origin corresponds to $R^{\text{nad}}(t)$. This figure and caption was taken from Ref. [41].

compared to the time $t < t_*$, even though one would expect that, as soon as the stability changes, $R(t)$ would make an immediate transition. Surprisingly, this is not the case. Instead, there is a persistence in following of fixed points which are in the meantime not attracting anymore, i.e., the loss of stability is *delayed* by the *stability-loss delay* time t_+. Such a delay time is a common phenomenon in singularly perturbed systems that feature dynamical bifurcations [49], and may be intuitively understood from the phase portraits in Fig. 2.3b: If the solution tracks a stable fixed point, and suddenly the stability is lost, it takes a finite time to spiral away from the now unstable fixed point.

The above framework now allows us to naturally explain the breakdown of adiabaticity: In Hermitian systems, the eigenvalues λ are strictly *real*, such that the fixed point's stability is not subject to changes. Within the realm of non-Hermitian physics, this restriction is however lifted. Following a path around the EP, we may cross the line $\mathrm{Im}\lambda = 0$ at which the stability changes, leading to a decisive change in the dynamics after a delay-time t_+. The exact value for this time depends on the exact path one chooses to encircle the EP, and may be calculated (see Refs. [41, 49] for details). If one prepares the system such that a state with $\mathrm{Im}\lambda > 0$ is populated initially, the system starts close to the adiabatic (unstable) fixed point. Thus, after a delay, the system switches to tracking the non-adiabatic fixed point that is stable under these conditions.

CHAPTER 3

Dynamically encircling EPs in waveguides

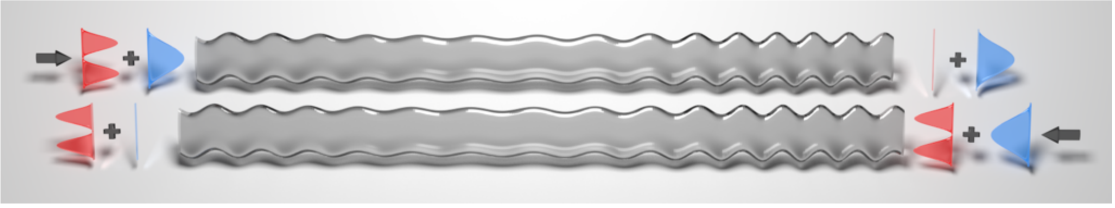

Figure 3.1: Schematic of an asymmetric mode-switch that projects the EP-encircling shown in Fig. 2.2 to a waveguide that strongly attenuates one of its two transverse modes depending on the injection direction. The parameter-space trajectories describing counter-clockwise and clockwise loops around the EP shown in panels **a** and **b** of Fig. 2.2 correspond to left and right injection shown here at the top and bottom, respectively.

While the fascinating features of non-adiabatic, chiral behavior has great potential for quantum control and switching protocols, it has so far defied any experimental realization. This is because to observe the non-adiabatic contributions requires a fully dynamical encircling of the EP that goes beyond the quasi-static experiments reported so far [23,50,51]. A dynamically resolved experiment is, however, extremely challenging, because of the required precise control of exponentially amplified or damped resonant modes which meet at the EP, which, in addition, must be decoupled from all other modes present in a system.

Proposals to these problems have meanwhile been put forward, such as to map the dynamical encircling of an EP to the polarization evolution in a stratified non-transparent medium [39], but the involved implementation requirements have so far prevented an experimental realization. Here, we overcome such difficulties by demonstrating that waveguides with two transverse modes can be suitably engineered such that the transmission through them is equivalent to a slow dynamical encircling of an EP (as sketched in Fig. 3.1, where the working principle of an asymmetric switch is shown). In this way we make the recently discussed dynamical features of EPs directly accessible through established waveguide technology as used for the transmission of sound, light, micro- and matter waves.

This work was executed in terms of a collaboration with Alexei A. Mailybaev, Julian Böhm, Ulrich Kuhl, Adrian Girschik, Florian Libisch, Thomas J. Milburn, Peter Rabl and Nimrod Moiseyev [52]. My contribution to this project was to develop the theoretical framework, to perform all numerical simulations, to assist with the design of the experiment and, in addition to the analysis, interpretation and discussion of the experimental and numerical findings, to co-write the manuscript and the accompanying supplemental material. Correspondingly, this chapter largely follows the manuscript in which these results are reported [52].

3.1 Model

To observe an asymmetric mode-switch in a realistic environment, we now map the Hamiltonian in Eq. (2.1) onto the problem of microwave transmission through a smoothly deformed metallic waveguide in the presence of absorption (see Fig. 3.1). The waveguide is extended along the x-axis and we restrict the following discussion to a single transverse dimension y. Within this framework, the parametric encircling of the EP from the 2×2 model shown above translates to a slow variation of a periodic boundary modulation along the waveguide. Directly at the EP, both the Bloch wavenumber K and the Bloch modes Λ of the electric field distribution $\phi(x, y) = \Lambda(x, y)e^{iKx}$ coalesce. More specifically, the harmonic solutions $\Phi(x, yt) = \phi(x, y)e^{-i\omega t}$ for fields oscillating with frequency ω obey the Helmholtz equation

$$\Delta\phi(x, y) + V(x, y)\phi(x, y) = 0 \;, \tag{3.1}$$

where Δ is the Laplace operator in 2D, $V(x, y) = \varepsilon(x, y)\, \omega^2/c^2$ is a complex potential proportional to the dielectric constant ε and c is the speed of light. For a straight rectangular waveguide with a fixed width W in y-direction the solutions of Eq. (2) in the absence of losses are $\phi_n(x, y) = u_n(y)e^{ik_n x}$ with transverse mode functions $u_n(y) = \sin(n\pi y/W)$ and wavevectors $k_n = \sqrt{\omega^2/c^2 - n^2\pi^2/W^2}$.

3.2 2×2 model

By choosing an appropriate input frequency ω, the transmission problem can naturally be reduced to only two propagating modes $n = 1, 2$. To implement a controlled coupling between these modes, we consider a waveguide subject to a boundary modulation $\xi(x) = \sigma \sin k_b x$, as shown in Fig. 3.1. By choosing the boundary wavenumber $k_b = k_1 - k_2 + \delta$, where $|\delta| \ll k_b$, near resonant scattering between the otherwise very different modes ϕ_1 and ϕ_2 occurs. The full solution for the propagating field can be written in the form

$$\phi(x, y) = \frac{c_1(x)}{\sqrt{k_1}} \sin \frac{\pi}{W} y + \frac{c_2(x)}{\sqrt{k_2}} \sin \frac{2\pi}{W} y e^{-ik_b x} \;. \tag{3.2}$$

Employing a Floquet-Bloch ansatz, we obtain a Schrödinger-type equation for the slowly varying modal amplitudes $\psi(x) = (c_1(x), c_2(x))^T$,

$$i\partial_x \begin{pmatrix} c_1(x) \\ c_2(x) \end{pmatrix} = \begin{pmatrix} \delta(x) - i\gamma_1/2 & g(x) \\ g(x) & -i\gamma_2/2 \end{pmatrix} \begin{pmatrix} c_1(x) \\ c_2(x) \end{pmatrix} , \tag{3.3}$$

where we present a more detailed derivation in appendix A – note that we have not made use of the paraxial approximation in our derivation since the present system defies this ansatz. The slow variation of $\delta = \delta(x)$ and $g = g(x) \propto \sigma(x)$ in Hamiltonian (2.1) is then directly implemented in the waveguide through a smooth variation of the modulation potential, which leaves the validity of Eqs. (3.2) and (3.3) intact. Finally, due to the even and odd symmetry of $u_1(y)$ and $u_2(y)$, an absorbing material placed close to the center of the waveguide gives rise to the required losses $\gamma_1 \gg \gamma_2$. With the above, all parameters in the non-Hermitian Hamiltonian H in Eq. (3.1) are determined. However, instead of governing the temporal dynamics (in time), H determines here the mode propagation in the longitudinal direction x. Correspondingly, the requirement of encircling the EP slowly (in time t) is transferred here to a slow variation of the boundary parameters along the propagation direction x (see Fig. 3.1). Quite remarkably, a right and left injection into the waveguide corresponds to a clockwise and counter-clockwise encircling direction of the EP, respectively, yielding a specific and different output mode depending only on the side from which the signal is injected.

3.2.1 Loop parametrization

Using the model (3.3), we now investigate the scattering in a waveguide for which the boundary modulation and the loss parameter change slowly along the propagation-axis x. Specifically, we choose a parametrization for the parameter evolution that conveniently ensures flat boundaries at the waveguide entrance and exit, allowing us to extend the applicability of our protocol to finite waveguides (see, e.g., the insets in Fig. 3.4),

$$\begin{aligned}
\sigma(x) &= \frac{\sigma_0}{2}\left(1-\cos\frac{2\pi}{L}x\right) , \\
\delta(x) &= \delta_0\left(2\frac{x}{L}-1\right)+\rho , \\
\eta(x) &= \frac{\eta_0}{4}\left(1-\cos\frac{2\pi}{L}x\right)^2 , \qquad (3.4)
\end{aligned}$$

where $0 \leq x \leq L$, with the waveguide length $L \gg \ell$. We emphasize that with this choice of parametrization our waveguide is not infinitely extended anymore (as assumed in the Bloch-picture employed in the derivation of the effective 2×2 model above), but rather of finite length. This procedure is well justified if the parameter variations over a distance $\ell \ll L$ are small. The constants σ_0 and δ_0 determine the amplitude and detuning strength of the boundary $\xi(x)$, respectively, η_0 denotes the dissipation strength and ρ corresponds to a constant detuning offset.

Note that the effective model has been derived with respect to a (locally) constant boundary frequency Ω, giving rise to the boundary $\xi(x) = \sigma \sin(\Omega x)$. If allowing for a spatially varying frequency $\Omega(x)$, the boundary phase $\varphi(x) \equiv \Omega(x)x$ has to be linearized in order to be translated into a periodic system that corresponds to the instantaneous and fixed oscillation frequency at a specific point x_0 [53]. Thus, instead of naively using $\xi(x) = \sigma \sin(\Omega(x_0)x)$, one has to employ $\xi(x) = \sigma \sin\left(\varphi^{\mathrm{lin}}(x)\right)$, with $\varphi^{\mathrm{lin}}(x) = \Omega^{\mathrm{lin}} x = \frac{d}{dx}\left(\varphi(x)\right)|_{x=x0} x$. This phase transformation also enables us to convert the frequency parametrization of the full 2D system Eq. (3.4) into the effective model picture.

Values of the boundary parameters used in the simulations are given in the captions of Figs. 3.3 and 3.5. The above is not, however, the only path in (δ, σ)-space suitable for an EP-encircling. In fact, quite general parameter trajectories for which the boundary amplitude σ is switched on and off smoothly and for which the detuning is swept through $\delta = 0$ are valid candidates for this task (a popular choice is, e.g., the Allen-Eberly scheme [53]). We refer to section 3.3.4.2 for a (hindsight) justification of our particular parametrization choice.

We emphasize that the systems realized at positions $x = 0$ and $x = L$ are identical, since both correspond to a uniform waveguide without absorption. A waveguide with parameters (3.4) therefore emulates a closed loop in parameter space and we will show that this loop encircles an EP degeneracy. To facilitate this, let us consider the plane (δ, σ), where the parameters (3.4) are presented in Fig. 3.2 by a solid black curve. The two black dots mark the start and end

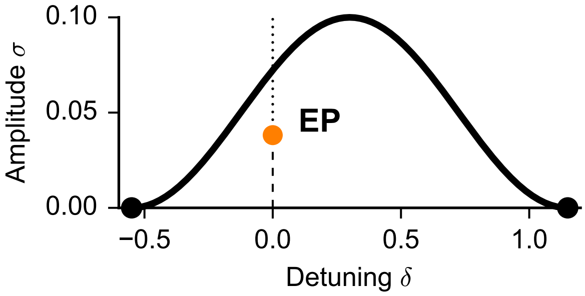

Figure 3.2: Path (3.4) in parameter space (δ, σ). The EP is indicated by an orange point. Black dots denote the start and end points of the trajectory, corresponding to identical uniform waveguides. The respective lines where $\mathrm{Re}E_1 = \mathrm{Re}E_2$ and $\mathrm{Im}E_1 = \mathrm{Im}E_2$ are shown by dashed and dotted lines, respectively.

points. For arbitrary δ and σ, we choose the Hamiltonian (A.24) with the damping parameter

$$\eta = \frac{\eta_0}{4}\left[1 + \cos\left(\pi\frac{(\delta - \rho)}{\delta_0}\right)\right]^2 , \tag{3.5}$$

providing an extension from the loop (3.4) to the whole (δ, σ)-plane. Using Eq. (A.33) with $g = B\sigma$ and $\gamma_i = \eta k/k_i$, one finds that there is a single EP degeneracy corresponding to

$$\delta_{\mathrm{EP}} = 0 \, , \quad \sigma_{\mathrm{EP}} = \frac{|\gamma_1 - \gamma_2|}{4B} = \frac{\eta_0}{16B}\left[1 + \cos\left(\pi\frac{\rho}{\delta_0}\right)\right]^2 \left|\frac{k}{k_1} - \frac{k}{k_2}\right| , \tag{3.6}$$

shown by an orange dot in Fig. 3.2. There are two lines at which either the real or the imaginary part of the energies $E_{1,2}$ coincide, starting at the EP in opposite directions: the one corresponding to equal energies $\mathrm{Re}E_1 = \mathrm{Re}E_2$ is shown by a dashed line, while the other, given by equal widths, i.e., $\mathrm{Im}E_1 = \mathrm{Im}E_2$, is indicated by a dotted line.

To assure ourselves that the loop indeed encircles the EP degeneracy (the orange dot), we note that since an EP represents a codimension-2 degeneracy in parameter space, it is a point for two-parameter systems (a curve for three-parameter systems, etc.) [54]. Thus, any closed loop in parameter space either has the topological property of encircling the EP, or it does not have this property. A loop is closed if its initial and final states describe identical physical systems, as considered in our work, even if the corresponding points on the parameter plane are different (marked by black dots in Fig. 3.2). In the present case this translates into curves that either go above the EP (encircling it), or curves that stay below the EP (not encircling it). As a result, the loop passing above the EP realizes the state-switch characteristic for an EP encircling (see the next section for more details).

3.2.2 Parametrical vs. dynamical encircling

A central theme of our work is that one must distinguish between a *parametrical* and a *dynamical* encircling of an EP. In the former case, we follow the change of eigenstates continuously along the loop, while in the latter case the parameters change slowly in time (here, in longitudinal direction x), and we follow the true solution of the time-dependent Schrödinger equation (3.3).

The instantaneous eigenvalues $E_i(x)$ and the (right) eigenvectors $\Phi_i(x)$ satisfy

$$H(x)\Phi_i(x) = E_i(x)\Phi_i(x)\,, \qquad i = 1, 2\,, \tag{3.7}$$

and we impose the normalization condition $|\Phi_i(x)|^2 = \Phi_i^\dagger(x)\Phi_i(x) = 1$. Here, the time (or position) x plays the role of a parameter. The fact that the EP is encircled parametrically by the loop leads to a state-flip if the eigenvectors $\Phi_i(x)$ are defined continuously dependent on x:

$$\begin{aligned} \text{mode 1} &= \Phi_1(0) = \Phi_2(L)\,, \\ \text{mode 2} &= \Phi_2(0) = \Phi_1(L)\,. \end{aligned} \tag{3.8}$$

Within the above framework, a *parametrical* encircling around the EP (traversing the loop in Fig. 3.2 from left to right) turns one instantaneous eigenvector continuously into the other, i.e.,

$$\circlearrowright\!: \Phi_1(0) \to \Phi_1(L) = \Phi_2(0)\,, \tag{3.9}$$

$$\circlearrowright\!: \Phi_2(0) \to \Phi_2(L) = \Phi_1(0)\,. \tag{3.10}$$

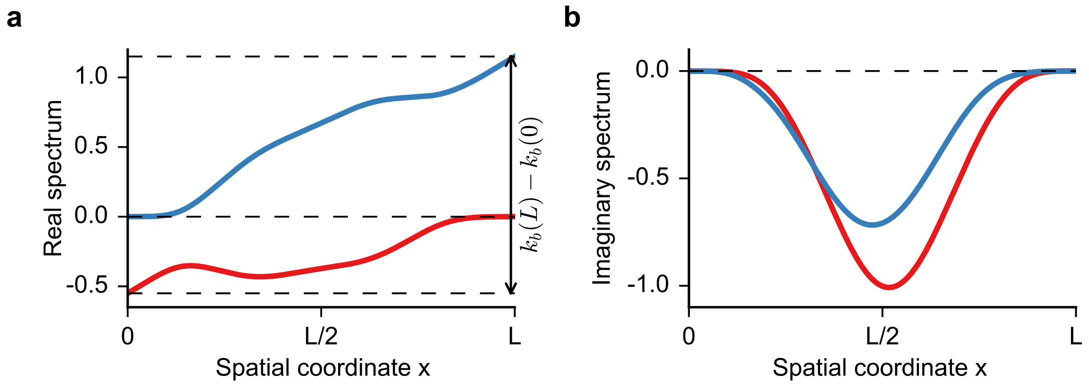

Figure 3.3: **a**, Real part of the parameter-dependent eigenvalue spectrum $E_{1,2}(x)$ Eq. (A.32) in the presence of bulk absorption, parametrized according to Eq. (3.4) (shown by solid lines). The coloring is such that red (blue) corresponds to the eigenvalue of the first (second) eigenstate at the beginning of the evolution at $x = 0$. **b**, Imaginary part of the spectrum. Here we employ a loss potential which is uniform in y-, and slowly varying in x-direction. In both panels the dashed lines indicate that the spectrum at the loop endpoints $x = 0$ and $x = L$ differs only by integer multiples of $k_b(0)$ and $k_b(L)$ in the employed Floquet-Bloch picture (we refer to the text for more details). In the above plots, the following set of values has been used to determine the waveguide parameters through Eq. (3.4): $L/W = 100$, $kW/\pi = 2.05$, $\sigma_0/W = 0.1$, $\delta_0 W = 0.85$, $\rho W = 0.3$, $\eta_0 W = 0.6$.

The same happens when traversing the loop in the opposite direction (from right to left):

$$\circlearrowleft\!: \Phi_1(0) \to \Phi_1(L) = \Phi_2(0) \, , \tag{3.11}$$

$$\circlearrowleft\!: \Phi_2(0) \to \Phi_2(L) = \Phi_1(0) \, , \tag{3.12}$$

realizing a symmetric switch of the initial states $\Phi_{1,2}(0)$ and final states $\Phi_{1,2}(L)$. Note that we ignore here the additional geometric phase factor since it is of no relevance for the present work.

The corresponding parameter-dependent eigenvalues $E_i(x)$ are shown in Fig. 3.3.

Note that at the endpoints $x = 0$ and $x = L$, the eigenvalues E_i are brought together again, i.e., $E_1(0) = E_2(L)$ and $E_1(L) = E_2(0)$, if we recall from Eq. (A.4) that K, and thus the eigenvalue E, is only determined $\mathrm{mod}\ k_b$. Here we take into account that k_b has an x-dependence as well, $k_b(x) = k_r + \delta(x)$, see Eq. (A.5). Directly at the loop endpoints, both the boundary modulation strength $\sigma(x)$ and dissipation $\eta(x)$ vanish, with the eigenvalues $E_i(x)$ then being given by $\delta(x)$ and 0. Thus, $E_2(0) - E_1(L) = 0$ and $E_2(L) - E_1(0) = \delta(L) - \delta(0) = k_b(L) - k_b(0)$, i.e., the respective eigenvalues coincide at $x = 0$ and $x = L$ due to the underlying Floquet-Bloch picture (see the dashed lines and the arrow in Fig. 3.3).

The above symmetric switching between states $\Phi_{1,2}$ is, however, not what happens when encircling an EP *dynamically*. Upon a numeric integration of Eq. (A.24) following the path defined in Eq. (3.4), we expand the solution vector in the instantaneous eigenbasis Eq. (3.7) as

$$\psi(x) \equiv \begin{pmatrix} c_1(x) \\ c_2(x) \end{pmatrix} = b_1(x)\Phi_1(x) + b_2(x)\Phi_2(x)\ . \tag{3.13}$$

Despite the flip of the instantaneous eigenvectors, the solution $\psi(x)$ initialized in one of the eigenmodes Φ_i generally follows the adiabatic prediction $b_i^{\mathrm{ad}}(x) \sim \exp\left(-i \int_0^x E_i(x')\mathrm{d}x'\right)$ only for one specific encircling direction if transported truly dynamically around the EP. The condition for this to happen (given in Ref. [19]) requires the non-adiabatic contribution to be small, and it is satisfied if the loop remains most of the time on the energy sheet of the longest lived state (see, also, Fig. 2.2a,b). For the other eigenmode, strong non-adiabatic effects appear, such that the state does not follow the instantaneous eigenvector but rather returns to itself, apart from some prefactor (see, e.g., Ref. [17]). If the encircling direction is reversed, the inverse behavior is found: the eigenstate that evolved adiabatically before now undergoes non-adiabatic transitions due to the system's non-Hermiticity, while the other eigenmode follows the adiabatic prediction (see the right column of Fig. 3.4). This means that, depending on the input direction, a specific dominating mode is obtained, realizing an asymmetric switch between the eigenmodes.

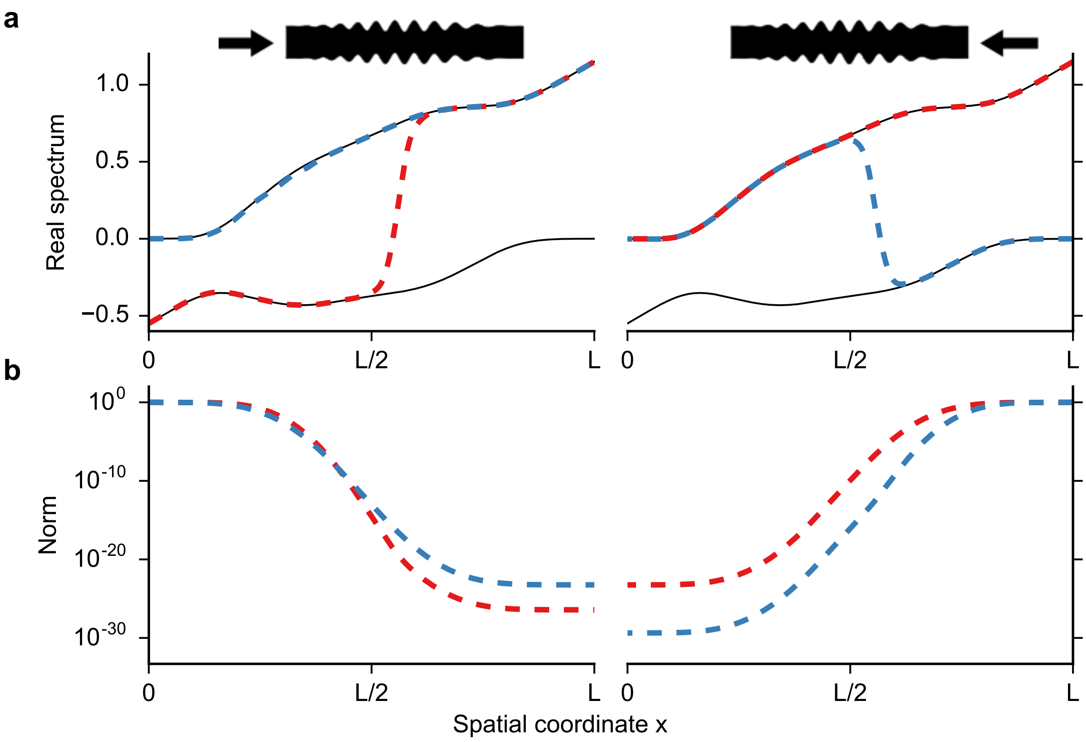

Figure 3.4: Counter-clockwise loops correspond to injection from the left (starting at $x = 0$, left column), clockwise loops correspond to injection from the right (starting at $x = L$, right column), see also the insets at the top. **a**, Position-dependent eigenvalue spectrum $E_{1,2}(x)$ (shown by black lines, corresponding to the data shown in Fig. 3.3), as well as $P(x)$, the real eigenvalue spectrum weighted by the respective eigenvector populations $|b_i(x)|^2$, shown in dashed colored lines. The coloring of $P(x)$ corresponds to the initial condition: Red (blue) corresponds to the state being injected in the first (second) eigenmode, for injection from the right the coloring is reversed since the instantaneous eigenmodes are flipped. The x position at which non-adiabatic transitions occur is located approximately at $x = L/2$, where $P(x)$ departs from the eigenvalue surface it initially follows. **b**, The norm $|b_1(x)|^2 + |b_2(x)|^2$, showing the magnitude of the overall decay for trajectories of the same color as in panel **a**. The corresponding model parameters can be found in the caption of Fig. 3.3.

3.2.3 Bulk absorption

In Fig. 3.4a we show the real eigenvalues $E_i(x)$ weighted by the respective eigenvector populations $|b_i(x)|^2$,

$$P(x) \equiv \frac{\mathrm{Re}E_1(x)|b_1(x)|^2 + \mathrm{Re}E_2(x)|b_2(x)|^2}{|b_1(x)|^2 + |b_2(x)|^2} \,, \tag{3.14}$$

for different initial conditions and encircling directions. When describing a loop around the EP in a counter-clockwise direction (which we identify with injection in the waveguide from the left), states initialized in either the first mode (red dashed line in Fig. 3.4a) or in the second mode (blue dashed line Fig. 3.4a) result in a population $|b_2(L)|^2$ that is much larger than the corresponding population $|b_1(L)|^2$, such that $P(x)$ from Eq. (3.14) follows closely the upper ($\mathrm{Re}E_2$) eigensheet. This corresponds to the first mode being dominant at the end of the waveguide at $x = L$ for both initial conditions:

$$\begin{aligned} &\circlearrowleft\colon \psi(0) = b_1(0)\Phi_1(0) \to b_2(L)\Phi_2(L) = b_2(L)\Phi_1(0) \,, \\ &\circlearrowleft\colon \psi(0) = b_2(0)\Phi_2(0) \to b_2(L)\Phi_2(L) = b_2(L)\Phi_1(0) \,. \end{aligned} \tag{3.15}$$

Upon reversing the encircling direction (trajectories now start at $x = L = 100$ and propagate leftwards to the final position $x = 0$, see the right column of Fig. 3.4), both initial states yield a much higher population for the other coefficient $|b_1(0)|^2$, which becomes much larger than $|b_2(0)|^2$:

$$\begin{aligned} &\circlearrowright\colon \psi(L) = b_1(L)\Phi_1(L) \to b_1(0)\Phi_1(0) = b_1(0)\Phi_2(L) \,, \\ &\circlearrowright\colon \psi(L) = b_2(L)\Phi_2(L) \to b_1(0)\Phi_1(0) = b_1(0)\Phi_2(L) \,. \end{aligned} \tag{3.16}$$

Thus, the system ends in a different final state Φ_2 as compared to Eqs. (3.15).

Furthermore, we want to emphasize that with a dissipation like in Eq. (3.5), both eigenstates experience equal dissipation at the start and end of the parameter trajectory, i.e., with $\mathrm{Im}E_1 = \mathrm{Im}E_2$ (see Figs. 3.3b and 3.7a). In this way a loop is realized that avoids multiple non-adiabatic flips during the evolution. See, e.g., Refs. [39–41] for a study on the consequences of different starting points in parameter space on the dynamics.

With this example we have already demonstrated the basic principle of our asymmetric switching device: suppose that a superposition of two modes is injected from the left and from the right. Due to the EP encircling induced by the spatial variation of the boundary amplitude and frequency (in the presence of loss), the initial state will result in different dominating pure modes at the end of the loop, depending only on the encircling direction. In the waveguide setup, this leads to a mode-selection depending on the direction from which the state is injected. With the boundary parametrization Eq. (3.4), our concept can be readily applied to the actual waveguide system (see section 3.3).

3.2.4 Position dependent absorption

It is evident from Fig. 3.4b, where we plot the norm of the propagating state ψ, that the device quality is strongly limited by the large absorption both propagating modes suffer from, leading to a decay by many orders of magnitude. For uniform absorption, this behavior is impossible to overcome: To induce a non-adiabatic transition during an EP encircling, the system size L and/or the absorption strength η have to be large. A reduction of either of the two quantities inevitably reduces the quality of the whole mode-selection scheme. Also, the relative dissipation strength of both modes, $|\gamma_1 - \gamma_2|$, is largest directly at the mode-opening $k \approx 2\pi/W$, where the wavenumber k_2 is much smaller than k_1 (see Eq. (A.3)). As shown in section A.5, these problems can be conveniently solved by introducing non-uniform absorption in the waveguide, which removes the absorption of one eigenmode and simultaneously increases the losses for the second considerably.

The non-uniform absorption is facilitated by identifying the nodes of the wavefunction $\phi(x, y)$ in Eq. (3.2) obtained for a system with no absorption, $\eta_0 = 0$, and placing absorbers at the node positions, yielding the loss distribution $\tilde{\eta}(x, y)$ which in turn determines Γ_{nm} in Eq. (A.28).

Wavefunction nodes In a first approximation we use the nodes of the unperturbed Bloch modes to determine the damping positions. We thus search for points where $|\phi(x, y)| = 0$, i.e., where both the imaginary and the real part vanish simultaneously,

$$\mathrm{Re}\, \phi(x, y) = 0 \quad \text{and} \quad \mathrm{Im}\, \phi(x, y) = 0. \tag{3.17}$$

If the components of the jth eigenvector, $(\Phi_{j1}, \Phi_{j2})^T = \Phi_j$, are non-zero for $\eta = 0$, the node positions in the unit cell restricted by $x_k \in [0, \ell_0]$ and $y_k \in [0, W]$ are given by

$$x_k = -\frac{i}{k_b} \ln \left(\pm \frac{\Phi_{j1}\Phi_{j2}^*}{|\Phi_{j1}||\Phi_{j2}|} \right), \quad \text{and} \tag{3.18}$$

$$y_k = \frac{W}{\pi} \arccos \left(\pm \frac{1}{2} \sqrt{\frac{k_2}{k_1}} \left| \frac{\Phi_{j1}}{\Phi_{j2}} \right| \right). \tag{3.19}$$

For $\sigma \neq 0$ and $\theta = 0$, the equation for the x-coordinates can be further simplified by inserting the corresponding expressions for the eigenvector Φ_j, the purely real $\Phi_{j1} = g = \sigma B$ and the purely real $\Phi_{j2} = E_j$, such that we obtain

$$\begin{aligned} x_k &= -\frac{i}{k_b} \log (\pm i) \\ &= \pm \frac{1}{k_b} \left(\frac{\pi}{2} + 2\pi n \right), \quad n = 0, 1, \ldots \\ &= \pm \frac{1}{k_b} \frac{\pi}{2} \pm \ell_0 n, \quad n = 0, 1, \ldots \end{aligned} \tag{3.20}$$

Thus, the x-coordinates are independent of the configuration (σ, δ). The y-coordinates, however, are still variable. Also, since we have $\ell = \frac{2\pi}{k_b + \delta}$, the unit cell size is variable with detuning δ.

Loss integrals Choosing a Gaussian shape to model an absorbing element at a position (x_k, y_k), with the standard deviation $\tilde{\sigma}$, we have

$$\tilde{\eta}(x, y) = \sum_k f(x, x_k, \tilde{\sigma}_x) f(y, y_k, \tilde{\sigma}_y), \quad f(z, \mu, \tilde{\sigma}) = \frac{1}{\sqrt{2\pi}\tilde{\sigma}} e^{-\frac{(z-\mu))^2}{2\tilde{\sigma}^2}}, \tag{3.21}$$

where the index k runs over all wavefunction nodes in the unit cell. To obtain the loss-matrix elements Γ_{nm} (A.28), we have to evaluate integrals of the form

$$\Gamma_{nm} = \frac{1}{\pi W} \frac{k k_b}{\sqrt{k_n k_m}} \int_0^{\ell_0} \int_0^W \tilde{\eta}(x,y) \sin\left(\frac{n\pi}{W} y\right) \sin\left(\frac{m\pi}{W} y\right) e^{-i(k_n - k_m)x} \mathrm{d}x \mathrm{d}y \,. \tag{3.22}$$

Since $\tilde{\eta}(x,y)$ can be separated into an x- and y-dependent part, we have

$$\begin{aligned} \Gamma_{nm} = \frac{1}{\pi W} \frac{k k_b}{\sqrt{k_n k_m}} \sum_k \underbrace{\int_0^{\ell_0} f(x, x_k, \tilde{\sigma}_x) e^{-i(k_n - k_m)x} \mathrm{d}x}_{I_x(x_k, \tilde{\sigma}_x)} \times \\ \underbrace{\int_0^W f(y, y_k, \tilde{\sigma}_y) \sin\left(\frac{n\pi}{W} y\right) \sin\left(\frac{m\pi}{W} y\right) \mathrm{d}y}_{I_y(y_k, \tilde{\sigma}_y)} \,, \end{aligned} \tag{3.23}$$

These integrals can be evaluated analytically, but due to the rapid vanishing of the Gaussian function $f(z, \mu, \tilde{\sigma})$ for $z \to \infty$, we can simplify the resulting expressions by integrating over the whole $\mathbb{R}^2$, yielding the analytical expressions

$$\begin{aligned} I_x(x_n, \tilde{\sigma}_x) &= e^{\frac{1}{2}(k_m - k_n)\left(\tilde{\sigma}_x^2 (k_n - k_m) + 2 i x_n\right)} \,, \\ I_y(y_n, \tilde{\sigma}_y) &= -\frac{1}{4} e^{-\frac{(m+n)\pi\left(2iWy_n + (m+n)\pi\tilde{\sigma}_y^2\right)}{2W^2}} \times \\ &\qquad \left(1 + e^{\frac{2\pi i (m+n) y_n}{W}} - e^{\frac{2\pi n\left(iWy_n + m\pi\tilde{\sigma}_y^2\right)}{W^2}} - e^{\frac{2\pi m\left(iWy_n + n\pi\tilde{\sigma}_y^2\right)}{W^2}}\right) \,, \end{aligned} \tag{3.24}$$

with which we obtain an analytical expression also for the loss-matrix Γ_{nm} in Eq. (3.23).

Results In Fig. 3.5 we plot the spectrum corresponding to the placement of loss as described by Eq. (3.23), where the imaginary part $\mathrm{Im} E_i$ now differs decisively from the system shown in Fig. 3.3: Now, the imaginary eigenvalue is close to zero for one mode, while the other mode exhibits a very large absorption.

One can immediately appreciate the benefit of the above strategy by comparing the results in Fig. 3.6 with Fig. 3.4: Injected from the left, one mode propagates adiabatically and approximately undamped, the other mode however is

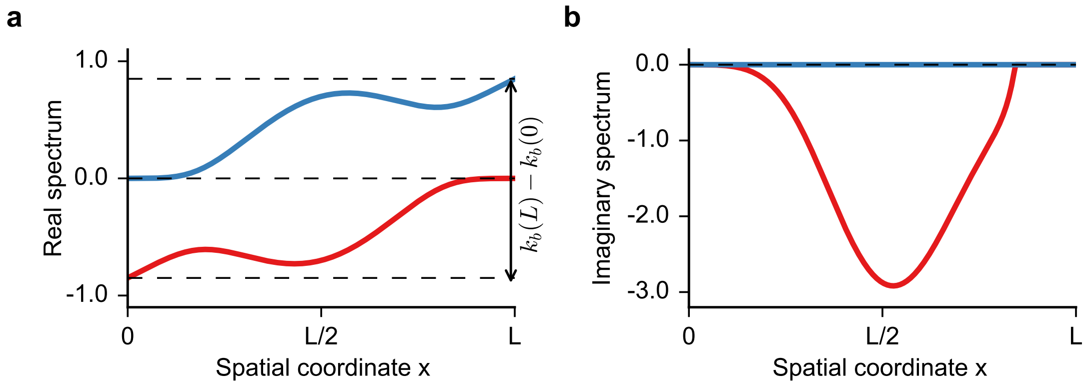

Figure 3.5: Here we show the same as in Fig. 3.3, with the difference that we are now employing position dependent absorption in the waveguide setup. Note that the respective imaginary part of the eigenvalue, $\mathrm{Im}\, E_n$, is almost zero for one mode, while it is very large for the other. The following set of values has been used to determine the waveguide parameters through Eq. (3.4): $L/W = 100$, $kW/\pi = 2.05$, $\sigma_0/W = 0.1$, $\delta_0 W = 0.85$, $\rho W = 0.0$, $\eta_0 W = 1.0$.

strongly dissipated while traversing the undulated waveguide and undergoes the non-adiabatic transition to the first mode. By way of this, we have realized a high-quality asymmetric switch that is based on the injection direction.

Furthermore, the designed absorber placement makes it possible to greatly reduce the device dimensions to lengths considerably smaller than a length-to-width ratio of $L/W = 100$, up to the limit at which additional non-adiabatic contributions inevitably set in due to the fast evolution.

To obtain the EP position, it is here also necessary to extend the Hamiltonian from the parameter trajectory to the inside of the loop, i.e., to extend the spectrum from the path $(\delta(x), \sigma(x))$ to all other points in the (δ, σ)-plane, and to show that the EP is encircled in the process. To extend the Hamiltonian, we choose

$$H(\sigma, \delta) = H_0 - i\frac{\eta_0}{2}\tilde{\Gamma}(\sigma, \delta) , \tag{3.25}$$

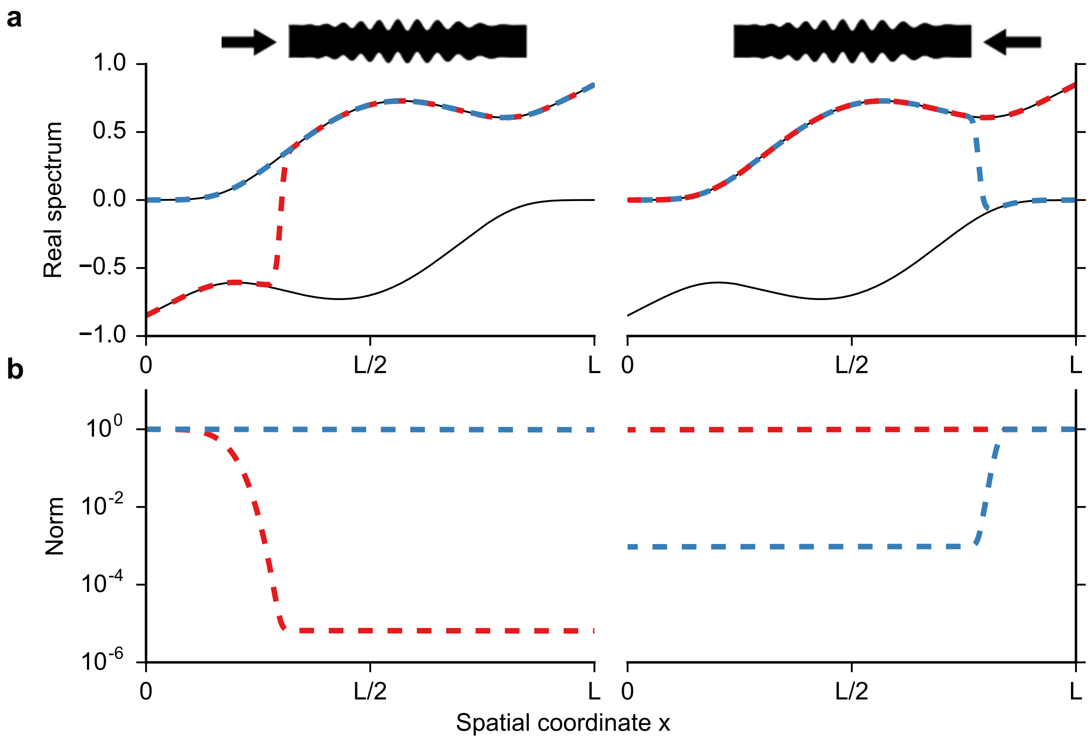

Figure 3.6: Here we show the same as in Fig. 3.4, with the difference that we are now employing position dependent absorption in the waveguide setup. The corresponding model parameters can be found in the caption of Fig. 3.5.

with

$$H_0 \equiv \begin{pmatrix} \delta & B\sigma \\ B\sigma & 0 \end{pmatrix} \quad , \quad \tilde{\Gamma}(\sigma,\delta) \equiv \begin{pmatrix} \frac{k}{k_1} & 0 \\ 0 & \frac{k}{k_2} \end{pmatrix} \Delta_\sigma + (1-\Delta_\sigma)\left(\frac{\sigma}{\sigma_0}\right)^2 \Gamma\left(f(\delta),\delta\right) \ , \tag{3.26}$$

$$f(\delta) \equiv \frac{1}{4}\left[1+\cos\left(\pi\frac{(\delta-\rho)}{\delta_0}\right)\right]^2 , \quad \Delta_\sigma \equiv f(\delta) - \left(\frac{\sigma}{\sigma_0}\right)^2 , \tag{3.27}$$

which interpolates between position dependent absorption at the parameter loop and a uniform dissipation at $\sigma = 0$. Here, the function $\Gamma(\sigma,\delta)$ denotes the matrix Γ_{nm} which is based on the node positions of Eq. (A.22), which in turn depends on $H_0 = H_0(\sigma,\delta)$ (i.e., the waveguide system in the absence of dissipation, $\eta_0 = 0$). In the above extension of the Hamiltonian, Γ depends only on δ, $\Gamma = \Gamma(f(\delta),\delta)$. The procedure to show that an EP is encircled is analo-

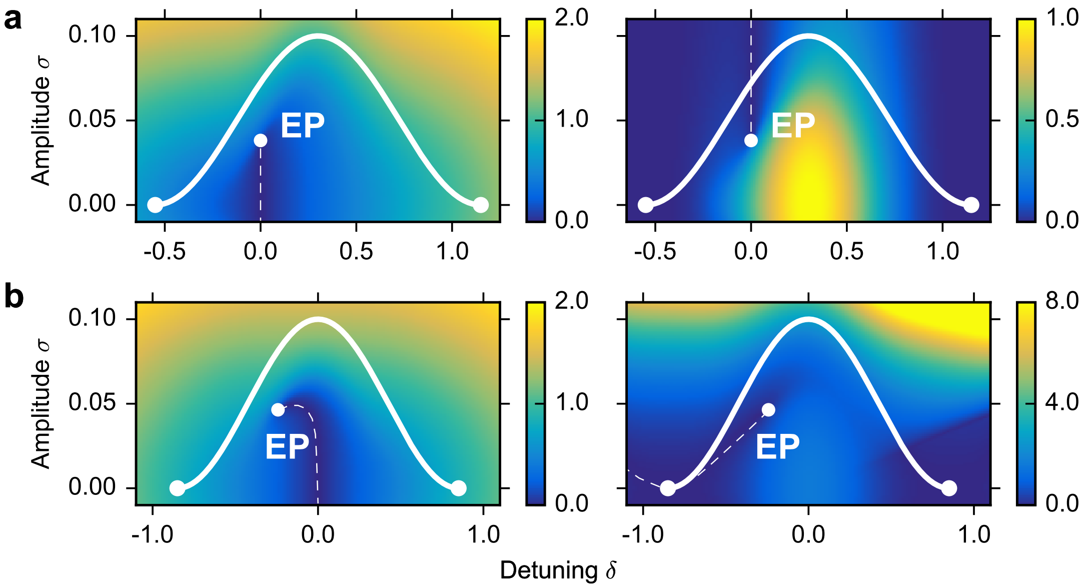

Figure 3.7: Paths in parameter space taken in Figs. 3.4 and 3.6 (solid white lines in panels **a** and **b**, respectively), on top of heatmaps of the eigenvalue sheets showing $|\mathrm{Re}E_1 - \mathrm{Re}E_2|$ (left column) and $|\mathrm{Im}E_1 - \mathrm{Im}E_2|$ (right column). Start and end points of the trajectories, as well as the EP, are indicated by white dots. The corresponding minima are highlighted by dashed white lines.

gous to the uniform absorption case, we thus refer here to section 3.2.1 for this argument. Here, we resort to obtaining the EP position numerically, since the analytic expressions are cumbersome and do not offer any additional insight (see Fig. 3.7b).

3.3 2D waveguide simulations

In the 2×2 model derived in section A.4 and employed in the previous chapter, we have introduced the parametrization Eq. (3.4) to describe the closed curve around the EP, and have shown that the desired asymmetric switch can be observed within the 2×2 model dynamics. Here, we go an important step further by numerically simulating the EP encircling in the full 2D geometry. Note that the 2D model we introduce here is readily applicable to 3D waveguides that feature a rectangular cross section (like, e.g., the experimental setup described in section 3.4) if the system resides in the lowest quantized mode between the top and bottom plates. As a consequence, the z-axis pointing out of the xy-plane can be neglected, justifying a 2D description (see Fig. A.1).

3.3.1 Backscattering resonances

As opposed to the 2×2 model, the full 2D waveguide system now supports 4 scattering channels instead of 2: In addition to 2 forward moving modes, the incoming flux may also be coupled to 2 backward moving channels. Thus, particular care has to be taken such that the injected intensity is not reduced by any resonant backscattering events. Although one might still accomplish a mode-filter by depopulating a given mode through reflection resonances, backscattering is detrimental to our aim of building a device that does not leak any flux in the backward direction, while simultaneously blocking a specific mode from moving forward.

For completeness, we note that the frequency-dependence of the resonances can be described by way of so-called amplitude-gradient scattering contributions induced by the waveguide boundary $\xi(x)$, originating from a surface-scattering theory that will be introduced in more detail in section 4. Here, we simply state that the mechanisms which attenuate the wave inside the waveguide can be understood via the mode-dependent attenuation length L_{nm}, which depends on the boundary profile's power spectrum $W(k_x)$ (see Eq. (4.3) in section 4). The quantity $1/L_{nm}$ may quantify the scattering in the waveguide: the larger (smaller) $1/L_{nm}$, the more (less) probable a specific event from mode n into mode m (and, simultaneously, from mode m into mode n). Neglecting a variation of σ and δ and assuming an infinite waveguide length L, the Fourier transform of

$$\xi(x) = \sigma \sin\Big((k_r + \delta)x\Big) \tag{3.28}$$

yields two delta functions peaked at $k_x = k_r + \delta$ and $k_x = -(k_r + \delta)$, respectively. For systems that possess a finite extent, the resonances acquire a finite width that is approximately given by $1/L$.

The mode's attenuation length L_{nm} is approximately given by

$$\frac{1}{L_{nm}^{b/f}} \propto W(k_n \pm k_m), \tag{3.29}$$

with k_n being the longitudinal wavenumber of the nth mode. The plus sign corresponds to backscattering (b) from mode n to mode m, whereas the minus sign denotes forward scattering (f); thus, Eq. (3.29) allows us to qualitatively relate the δ dependence of the reflection probabilities $|r_{nm}|^2$ with the respective maxima of the inverse attenuation lengths.

Since forward scattering $n \rightarrow n$ does not attenuate the mode, we identify the following mechanisms to be responsible for a mode's depopulation:

$$W(2k_1) \leftrightarrow |r_{11}|^2 \tag{3.30}$$

$$W(2k_2) \leftrightarrow |r_{22}|^2 \tag{3.31}$$

$$W(k_1 + k_2) \leftrightarrow |r_{12}|^2 \tag{3.32}$$

$$W(k_1 - k_2) \leftrightarrow |t_{12}|^2 \tag{3.33}$$

It is therefore crucial to choose the wavenumber k such that at $\delta = 0$, where we wish to resonantly couple both modes in forward direction, no other resonances in backward direction are located.

As mentioned in section 3.2.4, directly at the mode-opening k_1 and k_2 differ greatly, leading to large relative dissipation rates since, $\gamma_i = \eta k/k_i$. If the input wavenumber k is however chosen to be close to k_2, we have $k_1 + k_2 \approx |k_1 - k_2|$, i.e., the backward scattering resonance $1 \leftrightarrow 2$ is close to the corresponding forward scattering resonance on which our parametrization builds upon. Thus, for bulk dissipation in a 2D waveguide, the frequency at which an asymmetric switch can be conveniently operated with respect to its modal losses is unfavorable due to strong resonant backscattering. To counteract this limitation, we will introduce below a sophisticated absorber design which completely removes the necessity to use frequencies close to the mode-opening.

3.3.2 Rapid adiabatic passage

Before we investigate dissipative systems, however, we will analyze the transport properties of a system with vanishing dissipation, $\eta \to 0$. In this limit, the Hamiltonian is Hermitian, $H = H^\dagger$, and the adiabatic theorem applies: Assuming the parameters to be varied sufficiently slowly, a state follows the instantaneous eigenstate given that the eigenvalues are ensured to be non-degenerate [12]. Among the many applications of the above theorem, the rapid adiabatic passage (RAP) technique is particularly noteworthy, since it allows to robustly transfer the whole population of one eigenstate into another by adiabatically changing the system's parameters (see, e.g., Refs. [53,55,56]). For completeness, we mention that if the loss is removed, the two exceptional points collapse into a diabolical point (DP) [57] located at the parameter configuration $\sigma_{\mathrm{DP}} = 0$ and $\delta_{\mathrm{DP}} = 0$ (which can be seen from Eq. (2.6) by taking the limit $\eta \propto \gamma_{1,2} \to 0$).

As will become clear below, the adiabatic passage is the cornerstone of the implementation of our direction dependent asymmetric switch that is based on the path defined in Eq. (3.4) (for which the detuning is swept through resonance, $\delta = 0$, while the coupling σ is switched on and off simultaneously). These are already two of the three quintessential ingredients to accomplish adiabatic passage. An additional crucial point is that the Hermitian system is in the adiabatic limit, i.e., that the two-mode system investigated here shows the characteristic symmetric switching behavior $1 \leftrightarrow 2$ and $2 \leftrightarrow 1$ for injection from each side, prior to the application of any dissipation. This is readily accomplished at a critical waveguide length L^*, which value strongly depends on the channel parameters. It is thus the quantity L^* which will be the target of optimization procedures (see below).

We add that, if a loop is parametrized differently to achieve an EP-encircling (like, e.g., by a circle that directly starts and ends at $\sigma = 0$ and $\delta = 0$), the removal of absorption will in general not lead to a successful RAP scheme. For the above mentioned circular path, this is a direct consequence of the non-degeneracy requirement that is violated in this case.

3.3.3 Method

In our numerical simulations we solve the Helmholtz equation Eq. (3.1) on a finite-difference grid by means of the modular recursive Green's function method (MRGM) [58,59]. The transmission (reflection) amplitudes from mode n into mode m, t_{nm} (r_{nm}), are then determined by projecting the system's Green's function onto the flux-carrying modes in the semi-infinite leads which are attached to the scattering geometry. The corresponding modal intensities are given by $T_{nm} = |t_{nm}|^2$ and $R_{nm} = |r_{nm}|^2$, respectively. We choose the real part of the potential $V(x, y)$ to be finite (infinite) inside (outside) the cavity, corresponding to Dirichlet boundary conditions, and the imaginary part of the potential is determined such as to satisfy the protocol described in later sections.

3.3.4 Results

3.3.4.1 Unoptimized waveguide

First numerical results are shown in Fig. 3.8, where we implement the RAP protocol Eq. (3.4) on the basis of an example system with a length-to-width ratio of $L/W = 100$. The perfect switch is easily observed in the modal pattern for injections from either side of the waveguide (see Fig. 3.8a,b for left-, and pan-

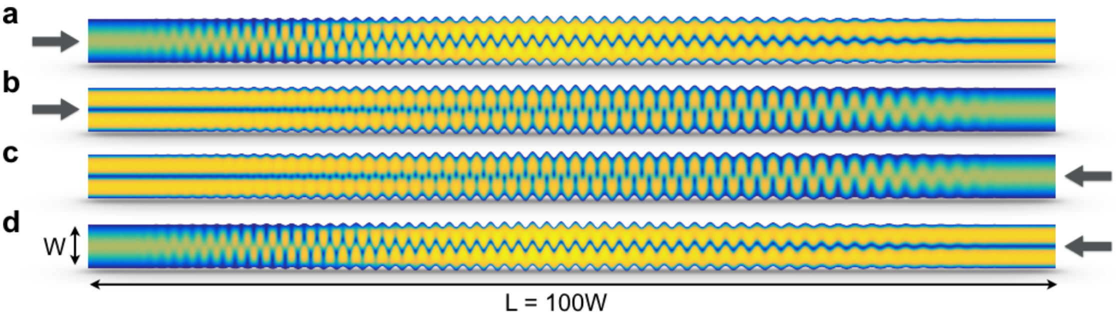

Figure 3.8: Numerically simulated modal wavefunction intensities $|\phi_n(x,y)|^2$ for a waveguide well in the adiabatic limit $L \gg L^*$, with a length-to-width ratio of $L/W = 100$ and with vanishing dissipation, $\eta = 0$ (the depicted dimensions are not to scale). Shown are results for different input modes and injection directions, corresponding to the encircling directions presented in Fig. 2.2. Arrows indicate the side from which the waveguide is excited, the first mode is injected in panels **a** and **c**, the second mode in **b** and **d**, respectively. In both cases we obtain a perfect switch, as can be seen from the transmission probabilities T_{nm} describing the transmission from mode n into mode m: $T_{21} \approx T_{12} > 0.9997$ and T_{nn} on the order of 10^{-5}. The following parameters have been used: $kW/\pi = 2.05$, $\sigma_0/W = 0.07$, $\delta_0 W = 0.5$ and $\rho W = -0.5$.

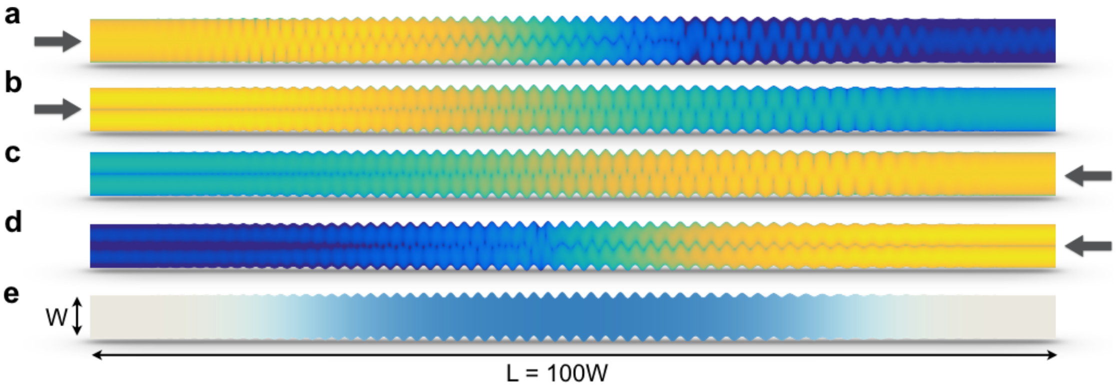

Figure 3.9: Same as shown in Fig. 3.8, except that here we allow for bulk absorption, with $\eta \neq 0$. Note that we employ a logarithmic scale for the respective intensities since the overall dissipation is very strong. This is evident from the corresponding transmission probabilities T_{nm}: $T_{11} = 2.5 \cdot 10^{-11}$, $T_{21} = 8.9 \cdot 10^{-7}$, $T_{12} = 7.0 \cdot 10^{-14}$ and $T_{22} = 8.4 \cdot 10^{-12}$. The normalized mode profiles at the waveguide exit are shown in Fig. 3.10. **e**, Plot of the absorption strength that is gradually switched on and off according to $\eta(x)$ in Eq. (3.4) with $\eta_0 W = 0.9/kW$, but otherwise uniform in transverse direction. The parameters used to describe a loop around the EP determine the waveguide boundary modulation: Its amplitude σ is proportional to the coupling g, the oscillation frequency k_b in turn is controlled by the detuning δ (see Fig. 3.13 for an example that displays the actual L/W dimensions and where the change in detuning is readily visible).

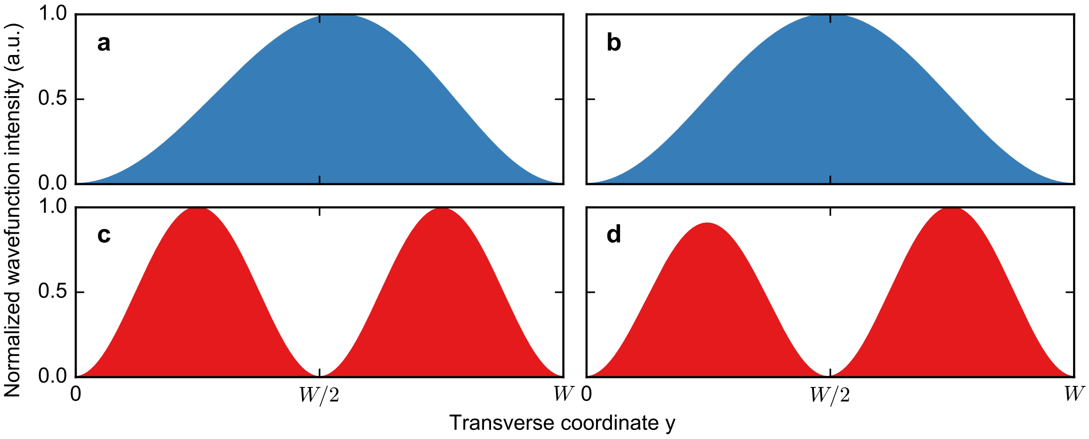

Figure 3.10: Numerically simulated modal wavefunction intensities $|\phi_n(x,y)|^2$ for a waveguide with a length-to-width ratio $L/W = 100$, obtained at the waveguide exit $x = L$ ($x = 0$) for injection from the left (right). This plot complements the data shown in Fig. 3.9 (with **a-d** corresponding to the panels with matching labels in Fig. 3.9). It is evident that we obtain close to pure modes at the device exits.

els c,d for rightwards injection). However, if one wishes to obtain a direction-dependent transmission characteristic, this symmetry has to be broken.

The desired asymmetric switching of modes in the above waveguide is realized by way of uniform (bulk) loss in transverse direction: Either mode entering from the left (Fig. 3.9a,b) is scattered into the first mode at the right exit lead. By contrast, any mode injected from the right side of the waveguide yields the second mode at the left exit lead (Fig. 3.9c,d; see, also, the wavefunction intensities directly at the waveguide exits, shown in Fig. 3.10). On the downside, however, the quality of this switching mechanism is extremely low, due to the large overall losses both states have to acquire in order to manifest this asymmetry. Additionally, the requirement of slow encircling translates into a long and bulky device with many boundary oscillations. To overcome both of the above obstacles, we devised the following two strategies to optimize the waveguide setup.

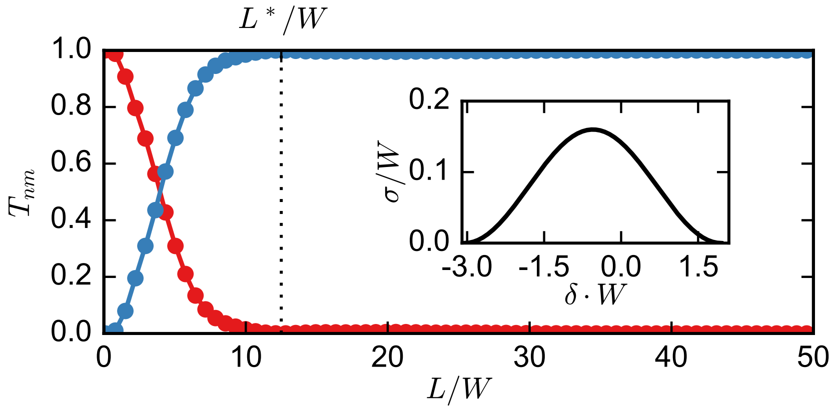

Figure 3.11: The transmission probabilities T_{11} (red) and T_{21} (blue) as a function of the relative system length L/W, where W denotes the waveguide width. For the employed optimized waveguide boundary the adiabatic limit is reached for lengths larger than a critical value of $L^* = 12.5W$, for which the transmission probability exceeds 99.5% (indicated by a vertical dotted line). The corresponding values of T_{12} and T_{22} have been omitted since they almost exactly coincide with the plotted values of T_{21} and T_{11}, respectively. To obtain the data points we have used $kW/\pi = 2.6$, the adiabatic threshold length L^*/W thus corresponds to 16.25λ, with the wavelength $\lambda = 2\pi/k$. In the inset we show the path taken in parameter space spanned by the oscillation amplitude σ and the detuning δ. Note that the δ value has been linearized to translate it into a system with fixed frequency (see 3.2.1).

3.3.4.2 Length optimization

Firstly, to optimize the waveguide dimensions, the figure of merit is the critical length-to-width ratio L^*/W from which value onward the system displays a close to perfect transmission probability from mode n into mode m, $T_{n\neq m} \approx 1$ (corresponding to a succesful RAP). For the actual optimization procedure to find the different optimal values δ_0, σ_0 and ρ (or, alternatively, different optimal boundary parametrizations), we have followed many approaches, ranging from employing different parametrization schemes [53,55], basic gradient-based optimization algorithms or global optimizers such as the differential-evolution techniques [60] to brute force scans over a grid of geometry parameters.

The characteristic curve for the (at the time of writing) optimal waveguide geometry can be seen in Fig. 3.11, in which we plot the length dependence of the transmission probability T_{nm} against the reduced waveguide length L/W. The adiabatic limit is reached at a threshold value $L^* = 12.5W$, after which the intermode transmission probabilities $T_{n \neq m}$ exceed 99.5%. For lengths smaller than this critical value a perfect mode switch is not realized, consequently rendering such waveguides unsuitable for a device that operates as an asymmetric mode-switch if losses are added.

The system employed in Fig. 3.11 corresponds to the smallest L^*/W value obtained as of yet through optimization techniques – it may, however, still be possible to obtain systems for which the threshold is even smaller. Candidates for this may be found using the *transitionless quantum-driving* (TQD) technique put forward by M. V. Berry in Ref. [61], which theoretically removes any non-adiabatic contribution in the dynamics of Hermitian systems and which should allow a perfect mode-switch at arbitrary device lengths [62, 63].

We have investitated if transitionless quantum driving can lead to an increased performance with respect to the system length (see appendix B for a derivation in terms of our effective model). Unfortunately, a system which accomplishes the RAP for even smaller system sizes has not been found by means of this method. We speculate that the reasons for this are twofold: Firstly, employing Berry's technique leads to waveguides with large boundary amplitudes that are out of phase with respect to each other, resulting in the unphysical situation that the waveguide walls start to overlap at some point. This results in the entrance and exit leads to be separated by an infinitely high potential wall, trivially leading to the absence of any transmitted flux (the smaller the system size, the larger the boundary amplitudes are becoming if using the TQD technique). For system sizes that are smaller than the best current value of $L^*/W = 12.5$, this basically results in a closed channel. Secondly, one has to keep in mind that the effective model derived in section A is a perturbatively obtained result for which the boundary amplitude σ and the detunings δ and ρ are assumed to be small. The present system with the best length-to-width ratio L^*/W however features values for these quantities which are not at all negligible. Therefore, any optimization procedure based on the first-order 2×2 model can be expected to fail for the full 2D system. Deriving the corresponding 2×2 model to higher orders in the waveguide parameters however may allow TQD to be applicable.

Bearing an experimental realization in mind, we will not make use of the smallest L/W ratio permitted by the waveguide parameters found above (for which $L^*/W \approx 12.5$). The reason is that the implementation of dissipation is much more difficult in an experimental setting than in a corresponding numerical simulation: Instead of tuning a single numerical parameter, different absorber materials have to be identified that provide the necessary damping, while simultaneously dissipating only in a narrow frequency interval. For the present case, the potential absorbers fit for the task were limited to only three potential candidates (two solid absorbers of type UD-12300 and DD-10017, respectively, and a foam absorber of type LS-10211, all from ARC technologies). Additionally, we speculate that if the waveguide would have been built at a length of $L/W = 12.5$, the total cumulative dissipation would have been too small to produce an asymmetric switch. We thus rely on a waveguide channel with a length-to-width ratio $L/W = 25$ in the following, while emphasizing that the waveguide presented in Fig. 3.12 readily accomplishes the same RAP quality as the waveguide shown in Fig. 3.8 at only a quarter of the length.

3.3.4.3 Absorber optimization

As shown in section 3.2.4, uniform dissipation may only lead to the breakdown of adiabaticity if η is sufficiently strong (or, alternatively, that the length L is sufficiently large, i.e., we demand $\eta L \gg 1$). Thus, short waveguides would require large losses that inevitably reduce the wave intensity at the device exits. We thus designed the absorption in the waveguide to follow a spatial pattern that minimizes (maximizes) the dissipation for the mode featuring the adiabatic (non-adiabatic) transition. In practice, we numerically extracted the coordinates of the modal intensity nodes that can, after a smoothing procedure, be directly

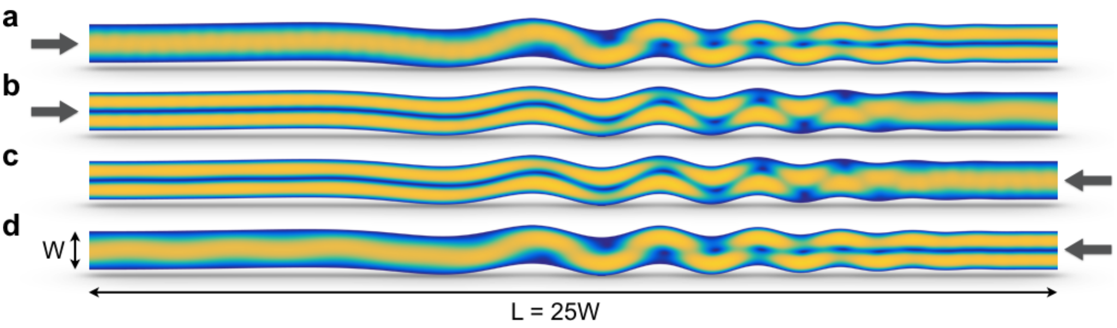

Figure 3.12: Modal wavefunction intensities $|\phi_n(x, y)|^2$ obtained numerically for injection from left (**a**) and right (**b**) for a system length $L = 25W = 32.5\lambda$ and vanishing dissipation, $\eta = 0$. In both cases we obtain a perfect switch, i.e., $T_{21} \approx T_{12} > 0.997$ and T_{ii} on the order of 10^{-3}. Note that the plots are to scale, i.e., the ratio of length L to width W reflects the actual waveguide dimensions. The following parameters have been used: $kW/\pi = 2.6$, $\sigma_0/W = 0.16$, $\delta_0 W = 1.25$ and $\rho W = -1.8$.

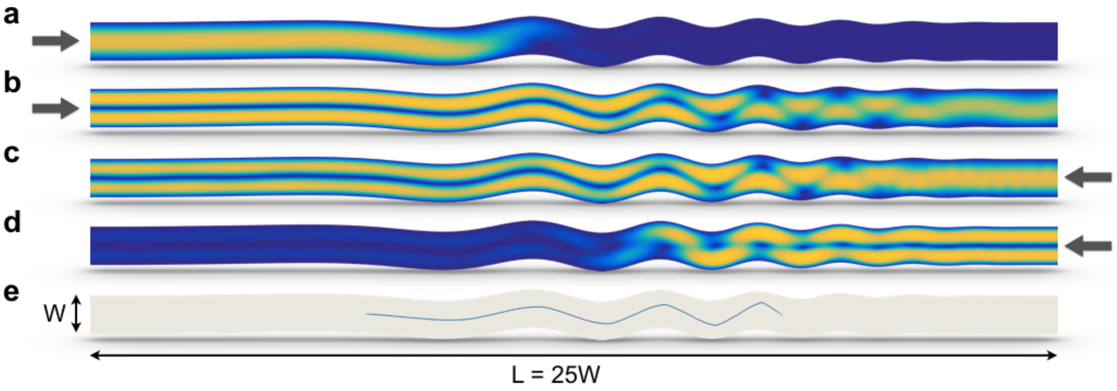

Figure 3.13: Numerically simulated modal wavefunction intensities $|\phi_n(x, y)|^2$ for a waveguide with a length-to-width ratio $L/W = 25$ (depicted dimensions are to scale). Shown are results for different input modes and injection directions, corresponding to different encircling directions. Arrows indicate the side from which the waveguide is excited, the first mode is injected in panels **a** and **c**, the second mode in **b** and **d**, respectively. **e**, Plot of the dissipation intensity $\tilde{\eta}(x, y)$. Since the respective reflection intensities R_{nm} are not accessible in the experiment, we have explicitly checked numerically that backscattering is negligible compared to the forward scattering contributions (see the text for details).

used as the absorbing element. As a consequence, the mode taking part in the transition $1 \leftrightarrow 2$ is strongly damped, while the corresponding mode in the transition $2 \leftrightarrow 1$ is left unperturbed and ideally transmits close to 100%. Note that this position-dependent loss in the waveguide leaves the topology of the loop around the EP intact (see section 3.2.4); additionally, the reciprocity principle ensures that our design principle works for both transmission directions equivalently.

For the system in Fig. 3.12, the absorber that is non-uniformly distributed in both the x- and y-direction is shown in Fig. 3.13e. The efficiency of the device is reflected in the transmission intensity $T_{21} = T'_{12} = 0.66$, where primed quantities correspond to injection from the right side of the waveguide. To ensure that the asymmetry observed in T_{nm} indeed stems from an effective EP encircling, we have explicitly checked numerically that backscattering is negligible compared to the forward scattering contributions. This fact is evident from the respective ratios of the dominant transmission intensity $T_{21} = T'_{12}$ vs. all reflection intensities R_{nm}, R'_{nm}, i.e., T_{21}/R_{nm}, T'_{12}/R'_{nm}, which are well above a value of 10^3.

Note that we choose a line-absorber as shown in Fig. 3.13e, where we exploit the fact that one has ample freedom in choosing the absorber position while still retaining the asymmetric switching effect. The most effective strategy relies on placing the absorbers directly at the modal node positions, as used for the effective model calculations shown in section 3.2.4. As found numerically in the corresponding 2D simulations, however, such a loss placement would result in undesirably large back-reflections in the experimental realization of the waveguide. To mitigate this shortcoming, we thus rely on a continuous stripe-absorber to obtain the decay necessary to encircle the EP, although it comes at the expense of an additional parasitic absorption for the other, previously undamped, mode. However, as we show in the Figs. 3.13 and 3.14, this alternative absorber design still readily allows to build an asymmetric switching device that qualitatively follows the predictions made with the help of the effective model presented in

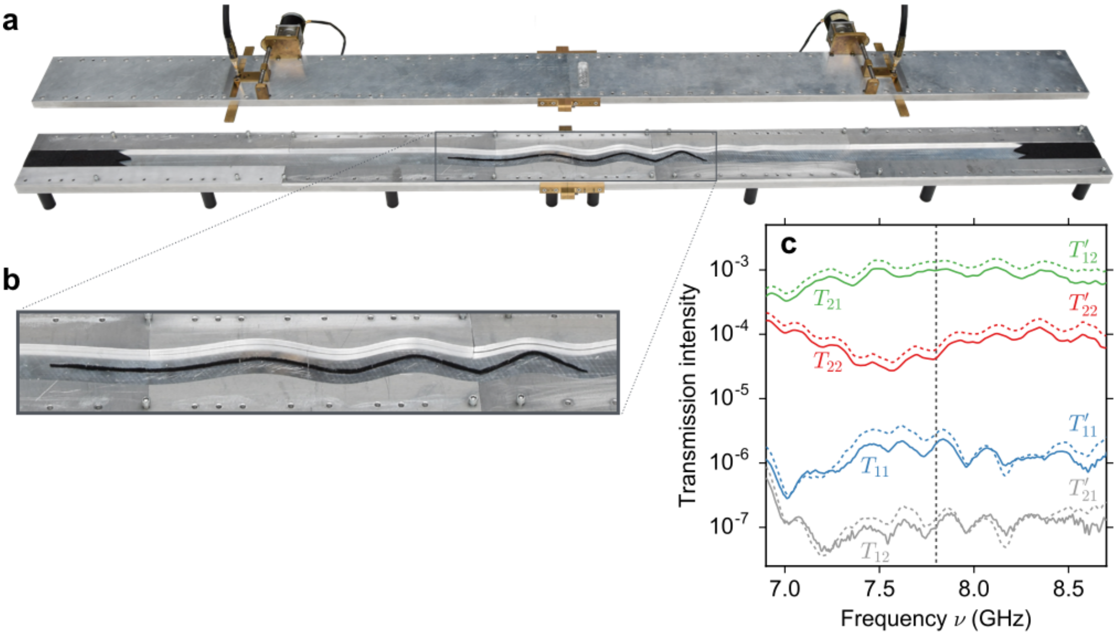

Figure 3.14: **a**, Photograph of the optimized waveguide channel used in the experiment, with a surface modulated region of length $L = 1.25$m and width $W = 5$cm. Within this setup, input and output antennas are placed 1.5m apart (shown on the top plate). Black foam is used both as an absorber in the center of the waveguide (magnified in panel **b**) and to mitigate the reflection into entrance and exit leads. The setup is engineered for a target frequency of $\nu = 7.8$GHz (shown by a dashed vertical line in **c**), however, the design ensures applicability over a broad frequency interval. **c**, Measured frequency dependent transmission intensities T_{nm} (T'_{nm}) from mode n into mode m for injection from left (right) are shown by solid (dashed) lines.

Eq. (A.29).

3.4 Microwave experiment

To demonstrate its potential for real-world applications, the first experimental realization of a dynamical EP-encircling has been implemented by Julian Böhm and Ulrich Kuhl of Nice University in a surface-modulated microwave setup following the proposed efficient design of Fig. 3.13 (the experiment is shown in Fig. 3.14a,b).

3.4.1 Setup

The experimental device itself is an aluminium waveguide with dimensions $L \times W \times H = 2.38\text{m} \times 5\text{cm} \times 8\text{mm}$. Fig. 3.14a shows the surface modulation that steers the modes around the EP. The microwave experiment allows to define the corresponding boundary conditions very accurately and to place the magnetized absorbing foam material ($W \times H = 1.2\text{mm} \times 5\text{mm}$) with sub-wavelength ($< 0.5\text{mm}$) precision. Additional absorbers ($W \times L = 5\text{cm} \times 17.5\text{cm}$) are employed at the waveguide entrance and exit to mimic semi-infinite leads.

In order to probe the sinusoidal modes formed by the z-component of the electric field E_z [29, 64], two microwave antennas 1.5m apart from each other are used. The antennas are fixed onto motor-controlled, moveable slides and measure the complex transmission signal outside of the modulated surface area at 2×2 points along the y-axis of the antennas. For the measurements we employ microwaves with a frequency around $\nu = 7.8\text{GHz}$, which is well below the cutoff frequency for TM$_0$ modes ($\nu_c = c/2H = 18.75\text{GHz}$), such that only the first two sinusoidal TM$_0$ modes contribute to the transport.

3.4.2 Results

Measuring the modal transmission intensities T_{nm} from mode n into mode m as a function of the input signal frequency, we unambiguously confirm the asymmetric switching effect (see Fig. 3.14c): An arbitrary combination of modes injected from the left side of the waveguide is transmitted into the first mode when arriving at the exit lead on the right (T_{11} and T_{21} dominate the transmission of the first and second mode, respectively, with transmission intensity ratios $T_{11}/T_{12} = 20.6$ and $T_{21}/T_{22} = 23.0$). At the same time, the second mode is produced on the left for injection from the right (T'_{12} and T'_{22} dominate the respective modal transmission, where the primed quantities are those for injection from the right, with ratios $T'_{12}/T'_{11} = 463.4 \approx T_{21}/T_{11} = 488.6$ and $T'_{22}/T'_{21} = 425.9 \approx T_{22}/T_{12} = 438.4$). Note that the slight violation of the reciprocity property $T'_{nm} = T_{mn}$ observed in the experiment (see Fig. 3.14c) is due to the magnetized absorber material (see the setup details above) that is needed to obtain a sufficiently strong absorption in the corresponding frequency range (without the absorber, the experiment is fully reciprocal). This small non-reciprocity is, however, not essential for the operation of our device, since the respective intensity ratios are approximately the same for both injection directions. Most importantly, the experimental data proves the very strong robustness of these transmission values with respect to variations of the input frequency - a broad-band feature that is a direct consequence of our design principle, which ensures operability also in the presence of small variations of the waveguide parameters. The shortened device for which the length-to-width ratio is now $L/W = 25$ also vastly outperforms the longer device in Fig. 3.9 (for which $L/W = 100$), not only in terms of length-to-width ratio, but also in terms of the output intensity which is here increased by six orders of magnitude.

3.5 Breaking of reciprocity?

A word of caution is required here, since the (alleged) breaking of reciprocity in modal transport has been a frequent source of confusion in the literature. In a prominent example, Feng et al. [65] claimed that non-reciprocal light transport had been achieved in a silicon photonic circuit, basing their reasoning on the modal intensity patterns at the waveguide exits that were asymmetric with respect to the injection direction. This conclusion was met with harsh criticism [66–68] which culminated in a comment [69] on the original work and a separate dedicated paper on the issue of optical isolation that appeared in Nature Photonics [70]. The main culprit was identified to be the unjustified reasoning that an asymmetric modal transport is sufficient for non-reciprocity. As has been thoroughly discussed in the above references, non-reciprocity requires the system to possess non-linearities, a time-dependence in its refractive indices or a breaking of time-reversal symmetry (as in the presence of a magnetic field).

All of the above mechanisms were not present in the our numerics – in the experiment, even though the magnetic absorber material induces a slight breaking of time-reversal symmetry, the quality of the asymmetric mode conversion we observe is not influenced by this small non-reciprocity.

We emphasize that the device we put forward and discuss here is thus not to be confused with a non-reciprocal one, since this would require, in its strict sense, an S-matrix which is *not* transposition symmetric, i.e., $S^T \neq S$ [70]. Instead, we study linear, time-independent systems which preserve (Lorentz-) reciprocity. The direction-dependent effect, i.e., the asymmetric mode-switch, we investigate here must therefore not be mistaken with optical isolation. Indeed, throughout all of our numerical simulations we always have $S = S^T$. Nonetheless, we are able to put forward a design for which we demonstrate high performance asymmetric switches for which the relative population of the damped mode compared to the dominating one is less than 5%.

3.6 Rabi oscillations

For completeness, we also mention that our scheme which relies on a clever absorber placement is not restricted to systems in the adiabatic limit. A similar effect can be achieved by a boundary featuring no frequency sweep, $\delta = 0$, and a constant boundary amplitude, $\sigma = \sigma_0$, for which we expect Rabi oscillations such that the mode's populations alternate periodically (note that this is in complete analogy to a two level atom that is driven resonantly by a light field [53]). In our waveguide system, however, it is the boundary modulation σ that is responsible for the coupling of the two levels. Thus, we obtain transmission peaks at periodic intervals of the reduced length

$$L_n/W = \frac{\pi}{2gW}\,(1+2n)\ , \quad n \in \mathbb{N}^0\ , \tag{3.34}$$

where the quantity $g = \sigma B$ plays here the role of the Rabi frequency. An example of these oscillations is shown in Fig. 3.15, where transmission peaks close to

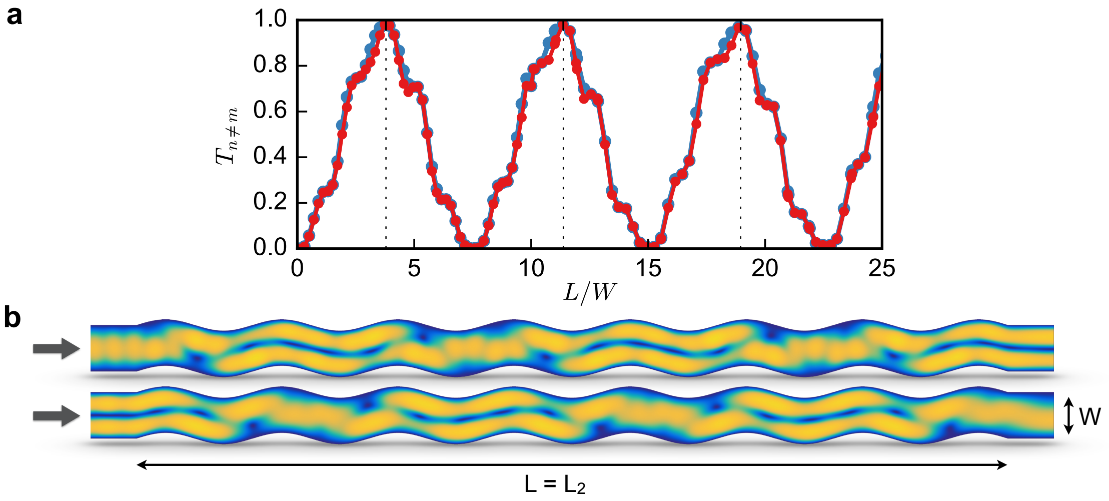

Figure 3.15: **a**, The transmission probabilities T_{12} (red) and T_{21} (blue) as a function of the relative system length L/W, where W denotes the waveguide width. Note that the transmission peak positions (with $T_{n\neq m}^{\mathrm{peak}} \approx 97\%$) are very well described by the effective model predictions (the L_n values found in Eq. (3.34) are indicated by vertical dotted lines). The following waveguide parameters have been used in the numerical simulations to parametrize the boundary $\xi(x) = \sigma \sin(k_r x)$: $kW = 2.5\pi$ and $\sigma/W = 0.12225$. **b**, Modal wavefunction intensities in a waveguide of length $L/W = L_2/W = 5\pi/2gW$. The periodic intervals Eq. (3.34) at which the whole population of one mode has completely switched to the other mode are clearly visible.

100% are clearly visible. We note that each of the waveguide systems of length L_n, at which we obtain these peak values, may be used to build an asymmetric switch (necessitating, however, the addition of tailored absorbers to induce the asymmetry in the transport).

The obvious advantage of Rabi oscillations is that the system size can be shortened radically, the oscillation frequency only depending on the product of the parameter B and oscillation amplitude σ. On the other hand, however, we are less robust against perturbations in the wave frequency, a feature reserved for systems in the adiabatic limit. Moreover, the transmission $T_{n\neq m}$ is not as large as in the RAP case where the boundary amplitude is switched on and off smoothly, and any absorption has to be applied in a very short length interval (rendering the specific implementation details very challenging even in the numerics).

Lastly, it is doubtful that the EP is actually encircled if any losses are introduced. Note that while in this case the exceptional point is definitely not encircled adiabatically, the non-crossing model might correspond to a discrete "loop" around the singularity: since the boundary modulation is switched on and off abruptly, the parameter configuration may represent a jump from $(0, 0)$ to $(0, \sigma)$ and back to $(0, 0)$ in parameter space space. We close this section by speculating that this could be the situation realized in the controversal paper mentioned already above [65].

CHAPTER 4

Reflection resonances in surface-disordered waveguides

Complementary to the previous chapters in which we have realized a direction-dependent asymmetric mode switch by way of exploiting exceptional points in boundary modulated waveguides, we focus here on a different aspect of surface scattering, namely the scattering due to higher-order effects of the disorder. This work was done in collaboration with José A. Méndez-Bermúdez, Johannes Feist, Otto Dietz, Dmitry O. Krimer, Nykolay M. Makarov, and Felix M. Izrailev [28]. My contribution to this project was to perform all numerical calculations, to extend the analytical framework originally developed by Nykolay M. Makarov and Felix M. Izrailev, and to analyze the analytical results as well as the numerical data. Finally, I have co-authored the manuscript which this chapter is based on [28].

4.1 Introduction

The problem of scattering off a rough surface is by itself a central topic in physics which occurs for many different types of waves and on considerably different length scales [71–74]. Phenomena induced by surface corrugations

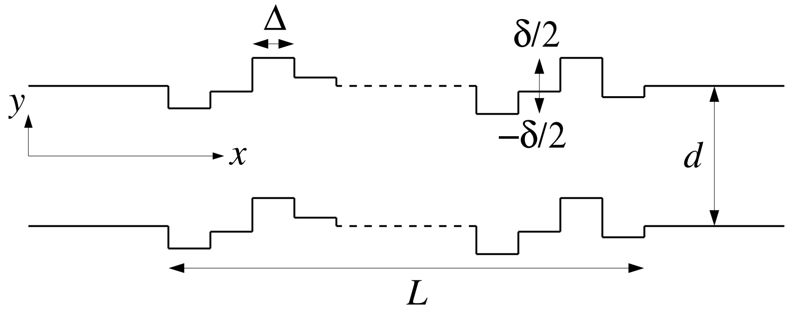

Figure 4.1: Illustration of the considered surface-disordered waveguide of length L attached to semi-infinite collinear leads of width d. The step-like surface disorder is characterized by a constant step width Δ and a maximum disorder-strength δ, respectively (see text for details). Flux is injected from the left. An example of an *antisymmetric* geometry is shown in which the upper and the lower surface disorder are identical.

play a major role in the study of acoustic, electromagnetic and matter waves alike and appear in macroscopic domains such as acoustic oceanography and atmospheric sciences [75, 76], but also emerge on much smaller length scales, e.g., for photonic crystals [77,78], optical fibers and waveguides [79–82], surface plasmon polaritons [83], metamaterials [84], thin metallic films [85–88], layered structures [89], graphene nanoribbons [59, 90], nanowires [24, 91–93] and confined quantum systems [94,95]. While having a detrimental effect on the performance of many of the above systems, surface roughness can also be put to use, e.g., for the fabrication of high-performance thermoelectric devices [96, 97] and for light trapping in silicon solar cells [98]; rough surfaces also cause anomalously large persistent currents in metallic rings [25] and provide the necessary scattering potential to manipulate ultra-cold neutrons which are bound by the earth's gravity potential [99].

In view of this sizeable research effort it might come as a surprise that even quite fundamental effects emerging in surface disordered systems are still not fully understood. Consider here, in particular, the problem of wave transmission through a surface-corrugated guiding system which we will study in the following. As demonstrated in detail below, even a very elementary and well-studied model system, consisting of a two-dimensional (2D) waveguide with a step-like surface disorder on either boundary (see Fig. 4.1), can only be inadequately described with conventional techniques. The reason why the knowledge on surface-disordered waveguides is still far behind the state-of-the-art for bulk-disordered systems is mainly due to the difficulties arising from the non-homogeneous character of transport via different propagating modes (channels). As was numerically shown in [100, 101], the transmission through multi-mode waveguides depends on many characteristic length scales which are specific for each mode. As a result, one can observe a coexistence of ballistic, diffusive, and localized regimes in the *same* waveguide when exploring mode-dependent transport coefficients (see, also, the related work in [102] where similar behavior has been observed in three-dimensional structures). Such effects lead to non-homogeneous scattering matrices which prevents the application of well developed analytical tools such as Random Matrix Theory [103,104] or the Ballistic Sigma Model [105, 106]. Additionally, the prospect of *engineering* the transmission through a waveguide by imprinting a specific surface profile [29] requires a theory which is not based on some general assumptions on randomness in the surface disorder, but one which relates an arbitrary but *given* surface profile to the transmission of each transporting channel.

An analytical surface scattering theory developed in [107,108] is a promising candidate to fulfil this task. According to this theory the transmission through waveguides with a weak surface corrugation is determined by *two* principally different correlators embedded in the surface profile, where the $\mathcal{W}$-correlator typically gives the main contribution to scattering which also appears in conventional approaches. This standard binary correlator measures the correlations between the profile *amplitudes* at the points x and x'. The $\mathcal{S}$-correlator, on the other hand, is due to the correlations between the *squares of the slopes* (squares of the derivatives) of the profiles at the points x and x'. In most theoretical studies, this $\mathcal{S}$-correlator is, however, neglected since it constitutes a higher-order term in the weak disorder expansion where the disorder amplitude is the relevant expansion parameter. In this work, we will provide conclusive evidence that this term, although being of higher-order, can dominate the transmission through a surface-disordered waveguide and that it needs to be taken into account in a comprehensive description.

First numerical and experimental indications that the $\mathcal{S}$-correlator plays, indeed, an important role have been put forward in a recent experimental study, where a specific waveguide geometry was designed such as to highlight the presence of this new term [29]. This joint work will be reviewed in section 5. Here we build upon this result to demonstrate that the influence of this correlator shows up not just for carefully chosen waveguide geometries, but in a quite general class of waveguides.

In particular, we will show that waveguides with a step-like surface disorder which have been well-studied by the community yield unambiguous and very pronounced signatures for the influence of the $\mathcal{S}$-correlator which, to the best of our knowledge, have so far been overlooked. In these waveguides (see Fig. 4.1), the surface disorder features steps of random height (in the direction transverse to propagation) and of constant width (in longitudinal direction). Such waveguides have been considered in quite a few recent studies [24–27], as they are attractive model systems both for an experimental implementation as well as for a numerical computation. This is because waveguides with the above specifics can be easily built up by combining a series of rectangular waveguide stubs, each of which has no surface disorder but a randomly chosen height. Our analysis will show that in these concatenated systems the $\mathcal{S}$-correlator gives rise to well-defined resonances in the reflection coefficients which are perfectly reproduced in a corresponding numerical study. At these resonant values the $\mathcal{S}$-correlator may strongly dominate over the lower-order $\mathcal{W}$-correlator such that a conventional description breaks down.

To show this not just by numerical evidence, but also by the corresponding analytical expressions, we significantly expand the existing theoretical framework presented in [107, 108]. This is necessary because the surface derivatives which enter the $\mathcal{S}$-correlator diverge at the steps in the surface profile and thus require a special treatment. Another important extension of the theory which we take into account is due to multiple scattering events between the propagating modes in the waveguide which yield a significant contribution beyond the single-scattering terms that have been considered so far. In this sense, our combined analytical-numerical study not only reveals a new effect, but also contributes to an extension of the underlying theory to the point where the analytical formulas which we derive provide predictions which quantitatively match with the numerical calculations that we perform independently.

4.2 Model

We consider a simple, however, non-trivial model consisting of a quasi-1D corrugated waveguide (or conducting wire) with discrete steps in the surface profile. This rough waveguide of length L and average width $d \ll L$ is attached to infinite leads of width d on the left and right (see Fig. 4.1). Flux is injected from the left and propagates through N_d open channels. The upper and lower surfaces of the rough waveguide are given by the functions $y_\uparrow = d/2 + \sigma\xi_\uparrow(x)$ and $y_\downarrow = -d/2 + \sigma\xi_\downarrow(x)$, respectively. The random functions $\xi_i(x)$ ($i = \uparrow, \downarrow$) describe the roughness of the surfaces and are assumed to be statistically homogeneous and isotropic, featuring zero mean, $\langle \xi_i(x) \rangle = 0$, and equal variances, $\langle \xi_i^2(x) \rangle = 1$. Altogether three different cases will be considered in terms of the symmetries of the boundary profiles with respect to the horizontal center axis at $y = 0$:

i. *symmetric* boundaries,

$$\xi_\uparrow(x) = -\xi_\downarrow(x) \, , \tag{4.1}$$

ii. *antisymmetric* boundaries,

$$\xi_\uparrow(x) = \xi_\downarrow(x) \, , \tag{4.2}$$

iii. *nonsymmetric* boundaries,

$$\xi_{\uparrow}(x) \neq \xi_{\downarrow}(x) \, . \tag{4.3}$$

Following the assumptions adopted in a few recent papers [24–27], the functions $\sigma\xi_i(x)$ are chosen as sequences of horizontal steps of constant width Δ and random heights, uniformly distributed in an interval $[-\delta/2, \delta/2]$ around the upper (lower) boundary of the attached leads. In our numerical analysis we set $d = 1$ and $\delta = 0.04$, resulting in a variance of the disorder, $\sigma^2 = \delta^2/12$, which is small compared to the width of the waveguide, $\sigma \ll d$.

Note that we have realized, in the above way, a scattering system which is truly random yet features very strong spatial correlations in its surface disorder since the waveguide exhibits a potential step at each integer multiple of the step-width Δ.

4.3 Analytical method

According to the theory developed in [107, 108], the correlations in the surface disorder enter the scattering properties of the system through two independent correlators. The first one is the binary correlator of the surface profile,

$$\mathcal{W}(x - x') = \langle \xi(x)\xi(x') \rangle \ , \tag{4.4}$$

which contains contributions only from the *amplitude* $\xi(x)$ and the *derivative* of the surface profile $\xi'(x)$. Correspondingly, the scattering mechanism that this correlator gives rise to is referred to as the *amplitude-gradient-scattering (AGS) mechanism*.

The other correlator contains scattering contributions which are independent of those in Eq. (4.4) and which are related to the square of the profile's derivative, $\xi'^2(x)$, in an effective potential description (see details in [107, 108]),

$$\begin{aligned} 2\,\mathcal{S}(x - x') &= \langle \mathcal{V}(x)\mathcal{V}(x') \rangle \\ &= \langle \xi'^2(x)\xi'^2(x') \rangle - \langle \xi'^2(x) \rangle^2 \, , \end{aligned} \tag{4.5}$$

with $\mathcal{V}(x) = \xi'^2(x) - \langle \xi'^2(x) \rangle$. The corresponding scattering process is thus referred to as the *square-gradient-scattering (SGS) mechanism*. We emphasize here that the validity of the identity $\langle \mathcal{V}(x)\mathcal{V}(x') \rangle/2 = \mathcal{W}''^2(x - x')$ used in different contexts (see, e.g., [29, 107, 108]) is restricted to Gaussian random processes and cannot be applied for the present step-like surface profiles. Indeed, as we will see below, this simplification would lead to a severe underestimation of the SGS mechanism in the present context.

In our further analysis it will not be binary correlators themselves which will be the key quantities, but rather their Fourier transforms $W(k_x)$ and $S(k_x)$,

$$W(k_x) = \int_{-\infty}^{\infty} \mathcal{W}(x)\, e^{-ik_x x}\, dx\,, \tag{4.6}$$

$$S(k_x) = \int_{-\infty}^{\infty} \mathcal{S}(x)\, e^{-ik_x x}\, dx\,, \tag{4.7}$$

which denote the *roughness-height* power spectrum and the *roughness-square-gradient* power spectrum, respectively. Here k_x is the longitudinal wavenumber which is determined by the transverse quantization condition

$$k_n = \sqrt{k^2 - (n\pi/d)^2}\,. \tag{4.8}$$

The index n stands for a specific open propagation channel with $n = 1, 2, \ldots, N_d$, where the total number of open modes is given by $N_d = \lfloor kd/\pi \rfloor$ and k denotes the scattering wavenumber.

For the scattering system in Fig. 4.1 the $\mathcal{W}$-correlator can be obtained analytically,

$$\mathcal{W}(x - x') = \left(1 - \frac{|x - x'|}{\Delta}\right) \Theta(\Delta - |x - x'|)\,, \tag{4.9}$$

which is strongly peaked for surface points x and x' which are closer to each other than the step width in the disorder, $|x - x'| < \Delta$, but zero for all larger distances, $|x - x'| > \Delta$.

For completeness and since it is a key parameter in [107, 108], we want to stress the fact that, if defining the correlation length R as the variance of the binary correlator $\mathcal{W}(x - x')$, the step width Δ and correlation length R are directly linked with each other, $R = \Delta/\sqrt{6}$. For the sake of simplicity we will use the step width Δ in all expressions in the following since it represents the quantity which we tune in our simulations and which is therefore the more natural parameter in our system.

The Fourier transform of $\mathcal{W}(x - x')$ then yields the analytical expression for the *roughness-height* power spectrum $W(k_x)$,

$$W(k_x) = \Delta \, \frac{\sin^2 (k_x \Delta/2)}{(k_x \Delta/2)^2} \, . \tag{4.10}$$

An important point to mention here is the following: Eqs. (4.9) and (4.10) implicitly assume that the rectangular steps in the profile boundary can be perfectly resolved by the scattering wave. However, due to the finite wavelength at which the scattering process takes place, also the resolution of the surface profile will always be finite. To accommodate this limited resolution, we introduce an effective smearing of the step profiles based on a Fermi-function $1/[1 + \exp(x/\rho)]$ (see appendix C for more details). The smoothness of this function is governed by the parameter ρ which leads to a smearing of a step profile over a region $\Delta x \approx 12\rho$ (see Fig. C.1 in the appendix for a corresponding illustration). If we now estimate that a scattering wave with a wavelength λ is associated with a resolution of $\Delta x \approx \lambda/2$, we obtain for the smearing parameter $\rho \approx \frac{\lambda}{24} \approx 0.03$. Employing this value for all further calculations, a comparison with the numerical data suggests that this simple estimate already captures our simulations remarkably well. Only in symmetric waveguides a reduced value of $\rho = 0.01$ yields better agreement.

Here we want to emphasize that, due to the limited resolution of waves at a finite wavelength, the propagating wave cannot distinguish between a (discontinuous) step-boundary and a smoothed version of the same profile (if the smoothing is on or below the same scale as the wavelength). We thus expect that our approach describes waveguides with a profile composed of equally spaced functions like, e.g., Gaussian ridges, equally well.

When incorporating the smoothness of the steps into the roughness-height power spectrum (4.10), we can again obtain a simple analytical expression which takes the following form (see appendix C for details),

$$W(k_x) = \frac{1}{\Delta}\frac{4\pi^2\rho^2}{\sinh^2(\pi k_x \rho)}\sin^2(k_x\Delta/2)\ . \tag{4.11}$$

For small values of ρ a Taylor series expansion is justified,

$$\frac{1}{\sinh^2(\pi k_x \rho)} \approx \frac{1}{\pi^2 k_x^2 \rho^2}\ , \tag{4.12}$$

yielding the result already obtained for infinitely sharp steps, Eq. (4.10).

The above approach involving a smearing of the step-disorder turns out to be essential when considering the *roughness-square-gradient* power spectrum $S(k_x)$. This is because, without the smearing, the corresponding expressions would diverge, as can easily be understood from the fact that the *gradient* turns into a delta function at the position of a step when an infinite resolution is assumed. This divergence is, however, conveniently tamed through the above procedure involving the Fermi-function, yielding the following analytical expression for $S(k_x)$ (see appendix C),

$$\begin{aligned} S(k_x) = \frac{1}{\Delta}\frac{k_x^2\pi^2}{72}\frac{(1+k_x^2\rho^2)^2}{\sinh^2(\pi k_x\rho)}\Bigg[&\frac{4}{5}\left(1+\frac{1}{2N_{\text{eff}}}\right)\Big(7+2\cos(k_x\Delta)\Big) \\ &+2\Big(1+\cos(k_x\Delta)\Big)\frac{1}{2N_{\text{eff}}}\frac{\sin^2\left[\left(N_{\text{eff}}+1/2\right)k_x\Delta\right]}{\sin^2(k_x\Delta/2)}\Bigg]\ . \end{aligned} \tag{4.13}$$

In addition to the smearing parameter ρ, the above expression contains also the integer number N_{eff} which determines the number of steps $2N_{\text{eff}}$ that are *effectively* involved in the scattering process. The notion of an effective number has been introduced here to take into account that the total number of steps in the waveguide, $2N = L/\Delta$, is typically significantly larger than the value $2N_{\text{eff}}$ which we find to reproduce our data. This difference, $N_{\text{eff}} \ll N$, can be attributed to the finite penetration depth of the propagating wave as a result of which the effective longitudinal dimension of the waveguide is greatly reduced. We shall thus determine the quantity N_{eff} through a direct comparison with the numerical data to be presented below. Note also that we have used ensemble averaging for the derivation of the above formulas (4.11) and (4.13) (to ensure convergence of Eq. (C.3) in the appendix) [109]. Recent work demonstrates, however, that an application of the predictions following from the two different correlators above yields good quantitative agreement also for individual disorder realizations as in single disordered waveguides [29].

A direct comparison of the expressions for the two correlators in (4.11) and (4.13) provides the insight that the SGS term $S(k_x)$ becomes *large* at exactly the same points at which the AGS term $W(k_x)$ *vanishes*. At these points, where $k_x\Delta = 2\pi M$ with M integer, the SGS term will thus dominate over the AGS term. As we will demonstrate below, this fact provides the key element for the occurrence of the pronounced resonances in reflection that we observe, and we will discuss how this resonance condition is realized for different symmetry classes. Note that these dominant SGS contributions in

$$\frac{\sin\left[(N_{\text{eff}}+1/2)k_x\Delta\right]}{\sin\left(k_x\Delta/2\right)} \tag{4.14}$$

would be suppressed if we applied the customary approximation (used, e.g., in [29, 107, 108]) that the defining expression for the SGS term, $\langle\mathcal{V}(x)\mathcal{V}(x')\rangle$, can be replaced by the simplified term $2\mathcal{W}''^2(x-x')$.

With the above expressions (4.11) and (4.13) we now have the key quantities at hand for the perturbation theory analysis of scattering in surface-disordered waveguides. For this analysis to be applicable, the perturbation induced by the surface disorder has to be weak, resulting in the following independent requirements,

$$\sigma \ll d\ , \quad R \ll 2L_n\ , \quad \Lambda_n = k_n d/(\pi n/d) \ll 2L_n\ . \tag{4.15}$$

Here, L_n is the *partial attenuation length* of the nth incoming mode (from the left) which takes into account both the scattering in *forward direction* (to the right) and in *backward direction* (to the left). The *cycle length* Λ_n is the distance between two successive reflections of the nth mode from the unperturbed surfaces. Under conditions (4.15) the waves are weakly attenuated over the correlation length R, the step width Δ and over the cycle length Λ_n. Clearly, the correlation length

	symmetric	antisymmetric	nonsymmetric
$\begin{pmatrix} A_{11} & A_{12} \\ A_{21} & A_{22} \end{pmatrix} =$	$\begin{pmatrix} 4\pi^4 & 0 \\ 0 & 64\pi^4 \end{pmatrix}$	$\begin{pmatrix} 0 & 16\pi^4 \\ 16\pi^4 & 0 \end{pmatrix}$	$\begin{pmatrix} 2\pi^4 & 8\pi^4 \\ 8\pi^4 & 32\pi^4 \end{pmatrix}$
$\begin{pmatrix} B_{11} & B_{12} \\ B_{21} & B_{22} \end{pmatrix} =$	$\begin{pmatrix} \frac{(3+\pi^2)^2}{18} & 0 \\ 0 & \frac{(3+4\pi^2)^2}{18} \end{pmatrix}$	$\begin{pmatrix} \pi^4/2 & 0 \\ 0 & 8\pi^4 \end{pmatrix}$	$\begin{pmatrix} \frac{(9+6\pi^2+10\pi^4)}{72\pi^4} & 20 \\ 20 & \frac{(9+24\pi^2+160\pi^4)}{72\pi^4} \end{pmatrix}$

Table 4.1: Matrices of constants $A_{nn'}$ and $B_{nn'}$ for the symmetric, antisymmetric and nonsymmetric waveguides considered in the text.

must be smaller than the waveguide length, $R \ll L$. When applying, in the above limit of weak disorder, the perturbative treatment following [107, 108], we obtain the mode-specific inverse attenuation lengths for scattering from any incoming mode n into any mode n' [108],

$$\frac{1}{L_{nn'}} = \frac{1}{L_{nn'}^{(b,AGS)}} + \frac{1}{L_{nn'}^{(f,AGS)}} + \frac{1}{L_{nn'}^{(b,SGS)}} + \frac{1}{L_{nn'}^{(f,SGS)}} . \tag{4.16}$$

All $L_{nn'}$ can be decomposed into backward (b) and forward (f) scattering contributions as well as into terms which are associated with the AGS and SGS mechanism of surface scattering. In their full, detailed form we thus obtain for the terms in Eq. (4.16),

$$\frac{1}{L_{nn'}^{(b,AGS)}} + \frac{1}{L_{nn'}^{(f,AGS)}} = \frac{\sigma^2}{d^6}\frac{A_{nn'}}{k_n k_{n'}}\Big[W(k_n + k_{n'}) + W(k_n - k_{n'})\Big] , \tag{4.17}$$

$$\frac{1}{L_{nn'}^{(b,SGS)}} + \frac{1}{L_{nn'}^{(f,SGS)}} = \frac{\sigma^4}{d^4}\frac{B_{nn'}}{k_n k_{n'}}\Big[S(k_n + k_{n'}) + S(k_n - k_{n'})\Big] . \tag{4.18}$$

Here the factors $A_{nn'}$ and $B_{nn'}$ depend on the symmetry between the two profiles $\xi_{\uparrow}(x)$ and $\xi_{\downarrow}(x)$ (see table 4.1), and the terms depending on $k_n + k_{n'}$ contribute to *backward scattering* whereas those depending on $k_n - k_{n'}$ result in *forward scattering*. The overall attenuation length of mode n can be obtained by means of the sum over all corresponding partial inverse mode-specific lengths $1/L_{nn'}$, $1/L_n = \sum_{n'=1}^{N_d} 1/L_{nn'}$.

As one can see from Eqs. (4.17) and (4.18), the mode attenuation lengths L_n essentially depend on the distinct correlators $\mathcal{W}(x)$ and $\mathcal{S}(x)$ through their Fourier transforms $W(k_x)$ and $S(k_x)$ derived above. The important point in this context is that $W(k_x)$ and $S(k_x)$ depend differently on the external parameters, in particular, on the wavenumber k_x and on the module width Δ. We may thus arrive at the situation that at specific values of the wavenumber the SGS-term in Eq. (4.18) ($\propto \sigma^4$) can be comparable to (or even larger than) the AGS-term in (4.17) ($\propto \sigma^2$). In particular, the points discussed above, where a peak value in $S(k_x)$ coincides with a zero of $W(k_x)$, can be expected to lead to interesting transmission characteristics.

To test this scenario explicitly, we performed extensive numerical simulations on transport through surface-disordered waveguides of all three symmetry classes.

4.4 Numerical method

Similar to the methods mentioned in section 3.3.3, we again employ the efficient "modular recursive Green's function method" (MRGM) [58, 59, 110] to numericall solve the Schrödinger equation for the Hamiltonian (in atomic units),

$$\hat{H} = -\frac{1}{2}\left(\frac{\partial^2}{\partial x^2} + \frac{\partial^2}{\partial y^2}\right) + V(x, y) , \tag{4.19}$$

on a discretized grid. The potential term V defines the surface potential which is infinite outside the waveguide and flat ($V = 0$) inside, corresponding to hard-wall boundary conditions. Since the scattering problem (4.19) is equivalent to the Helmholtz equation, our approach is not only suitable for electronic systems but can, e.g., also be applied to microwave systems as in [29, 111, 112], or quite generally to systems which satisfy a Helmholtz-like equation.

The MRGM is particularly advantageous for the present setup since the vertical steps in the disorder profile allow us to assemble the waveguide by connecting a large number of rectangular elements, which will be referred to as "modules". These modules are chosen to have equal width Δ, but different heights. The computation is based on a finite-difference approximation of the Laplacian and proceeds such that we first calculate the Green's functions for a number of modules with different heights. These Green's functions are then connected to each other by way of a matrix Dyson equation [59]. It is the different heights of the modules and additionally introduced random vertical shifts between them that give rise to the desired random sequence of vertical steps in the surface profile. To satisfy the additional symmetry imposed on the waveguide we arrange the modules such as to respect this specific symmetry.

The key element of our numerical approach is an "exponentiation" algorithm [24] which allows us to simulate transport through extremely long waveguides at moderate numerical costs. Rather than connecting individual modules with each other until the length of the waveguide is reached, we first connect several sequences of randomly assembled modules. In a subsequent step these "supermodules" are then randomly permuted and connected to each other to form a next generation of supermodules. Continuing this iterative procedure allows us to obtain the Green's functions of waveguides with a length that increases exponentially with the number of generations. For waveguides of moderate lengths we tested this supermodule technique against the conventional approach where the modules are assembled one after the other. We found that the disorder-averaged Green's functions obtained in these two ways do not show any noticeable difference from each other [24].

To calculate the desired transmission $(t_{nn'})$ and reflection amplitudes $(r_{nn'})$ for incoming flux from the left lead, we project the Green's function at the scattering wavenumber k onto the flux-carrying lead modes $n, n' \in \{1, \dots, N_d\}$ in the left and right lead, respectively. From these amplitudes we obtain the transmission from one mode to the other, $T_{nn'} = |t_{nn'}|^2$, as well as the total transmission through one mode, $T_n = \sum_{n'}^{N_d} |t_{nn'}|^2$, and the total transmission of the whole system, $T = \sum_{nn'}^{N_d} |t_{nn'}|^2$.

4.5 Comparison between analytical and numerical results

In order to compare the analytical predictions of equations (4.17) and (4.18) for the attenuation lengths with our numerical results for the waveguide transmission, we extract the values of the mode attenuation lengths from the numerical data through an automatized fitting procedure. To obtain accurate fits of the length dependence of the transmission we evaluate the transmission at up to 250 (symmetric waveguide), 200 (antisymmetric waveguide) and 80 (nonsymmetric waveguide) different length values in waveguides which reach a maximal length $L_{\max} = 2N\Delta$, with $N = 10^{10}$ (symmetric waveguide), $N = 10^{8}$ (antisymmetric waveguide) and $N = 10^{6}$ (nonsymmetric waveguide), respectively. To suppress effects which are due to individual disorder realizations we additionally average the transmission over 100 (symmetric and antisymmetric waveguides) and 50 (nonsymmetric waveguide) different disorder realizations. Our fits are then performed with the disorder-averaged transmission curves (details are provided below). To keep the system at a manageable degree of complexity and to perform a direct comparison with Eqs. (4.17) and (4.18), we restrict ourselves to the regime of two open waveguide modes, $N_d = 2$, by choosing the wavenumber k to be fixed at the value $k = 2.55\,\pi/d$. By varying the step width Δ in the surface disorder incrementally, we numerically scan through the module width dependence of the transmission (at each value of Δ an ensemble average over 50-100 waveguide realizations is performed).

We will now discuss the disordered waveguides with different symmetry separately, as both the predictions from Eqs. (4.17) and (4.18) as well as the procedure to extract the attenuation lengths are specific for each symmetry.

4.5.1 Symmetric profiles

In symmetric waveguides the up-down symmetry of the entire scattering structure, $\xi_{\uparrow}(x) = -\xi_{\downarrow}(x)$, results in the fact that modes of different symmetry cannot scatter into each other. For the two-mode waveguide considered here this means that the two modes $n\!=\!1,2$ scatter fully independently of each other with only *intra-mode* scattering (with $n = n'$) being relevant and *inter-mode* scattering (with $n \neq n'$) being entirely absent. Correspondingly, the only scattering mechanism that attenuates an incoming wave in mode n is back-scattering into the same mode (forward-scattering in the same mode does not attenuate the mode and inter-mode scattering is forbidden). For our analysis we therefore need to consider only the intra-mode back-scattering (b) length $L_{nn}^{(b)}$ which follows from Eqs. (4.17) and (4.18) [103],

$$\frac{1}{L_{11}^{(b)}} = 4\pi^4 \frac{\sigma^2}{d^6} \frac{W(2k_1)}{k_1^2} + \frac{(3+\pi^2)^2}{18} \frac{\sigma^4}{d^4} \frac{S(2k_1)}{k_1^2} \,, \tag{4.20}$$

$$\frac{1}{L_{22}^{(b)}} = 64\pi^4 \frac{\sigma^2}{d^6} \frac{W(2k_2)}{k_2^2} + \frac{(3+4\pi^2)^2}{18} \frac{\sigma^4}{d^4} \frac{S(2k_2)}{k_2^2} \,, \tag{4.21}$$

where $W(\cdot)$ and $S(\cdot)$ are defined by Eq. (4.11) and (4.13), respectively. Due to the decoupling of the two modes we are here in the 1D limit of single-channel scattering where all modes are localized and diffusion is absent (as in 1D bulk scattering systems [103]), resulting in an exponential decrease of the transmission $T(L)$ with waveguide length L,

$$\exp\langle \ln[T(L)] \rangle = \exp(-2L/\xi) \,. \tag{4.22}$$

For 1D scattering the localization length ξ is related to the mean free path as follows $\xi = 2l$ [103]. Identifying the mean free path for each mode with the specific backward scattering length $L_{nn}^{(b)}$, we obtain the desired relation $\exp\langle \ln[T_{nn}(L)] \rangle = \exp(-L/L_{nn}^{(b)})$ which we use to extract the backward scattering length $L_{nn}^{(b)}$ from the numerical data. The validity of this procedure is independently confirmed by the numerically determined length dependence of the transmission which follows the expected exponential decay very accurately (see Fig. 4.2(a)).

Following this analysis we extract from the disorder-averaged transmission the numerical values for $L_{nn}^{(b)}$ through the identity $\langle \ln T_{nn} \rangle = -L/L_{nn}^{(b)}$ and compare it to the corresponding analytical predictions in Eqs. (4.20) and (4.21). The

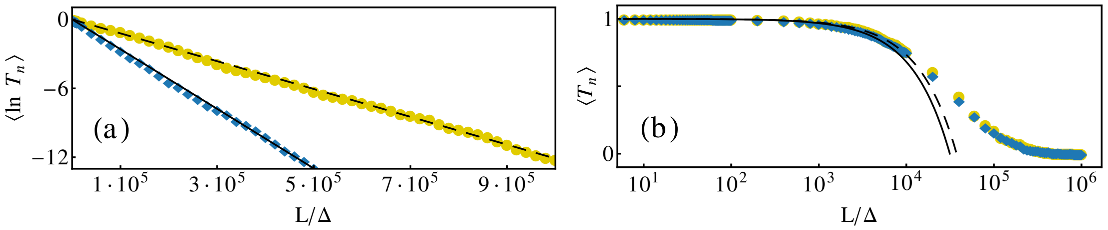

Figure 4.2: Illustration for how we extract the mode-specific attenuation lengths L_n from the numerical data in the case of (a) symmetric and (b) antisymmetric waveguides (for nonsymmetric waveguides the same procedure as in (b) is used and therefore not described separately): (a) In the symmetric case where all modes localize with their own specific localization length, we fit the expression $\langle \ln T_n \rangle = -L/L_n$ (see black lines) to the mean logarithm of the numerically obtained transmission $\langle \ln T_1 \rangle$ (yellow •) and $\langle \ln T_2 \rangle$ (blue ⧫), shown here versus the reduced length L/Δ (for $\Delta = 0.64$). (b) In the antisymmetric case we restrict ourselves to the ballistic regime, where the transmission of each mode decays along the following expression $\langle T_n \rangle = 1 - L/L_n$ (see black lines), which we use as a fitting curve for the mean numerically obtained transmission $\langle T_1 \rangle$ (yellow •) and $\langle T_2 \rangle$ (blue ⧫), shown here versus the reduced length L/Δ (for $\Delta = 1.53$). An automated fitting procedure yields mode-specific attenuation lengths L_n which show excellent agreement with our analytical estimates (see below). In the above figures, $\sigma \approx 0.01$ and $k = 2.55/\pi$ have been employed, respectively.

corresponding results for $1/L_{nn}^{(b)}$ as a function of Δ are shown in Fig. 4.3(a). We also plot the theoretical predictions given by Eqs. (4.20) and (4.21), respectively, as well as the AGS terms $1/L_{11}^{(b,AGS)}$ and $1/L_{22}^{(b,AGS)}$ alone. The agreement we find between the AGS terms and the numerical calculations is already remarkably good for most of the chosen parameters, such that the SGS contributions can be easily identified to be dominant at those specific parameter values where deviations from the AGS predictions occur (see vertical arrows in Fig. 4.3(a)). In full agreement with our theoretical analysis, we find that the values of the step width Δ where this happens are determined by the resonance condition $2k_n\Delta = 2\pi M$ (with M an integer), that we identified already earlier as those points where the contribution of the AGS terms vanishes while the SGS terms are maximal. Note that this condition leads to different resonance values for

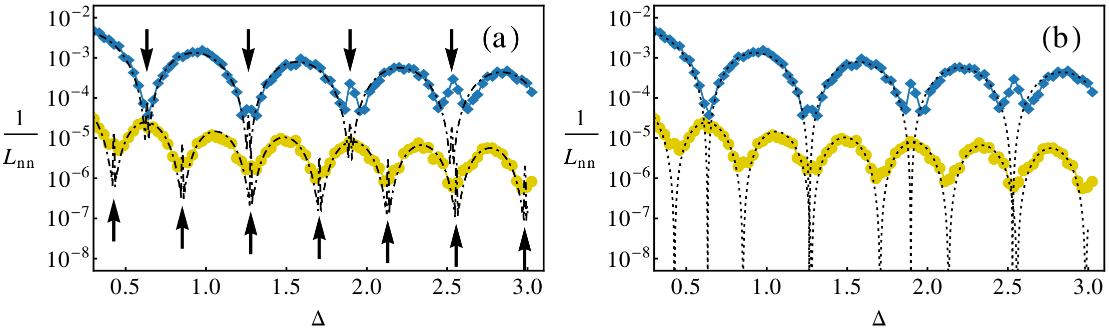

Figure 4.3: Inverse partial attenuation length $1/L_{nn}$ versus step width Δ, as obtained numerically for two-mode symmetric waveguides. $1/L_{11}$ (yellow ●) and $1/L_{22}$ (blue ♦) are shown. (a) Comparison with the analytical expressions (4.20) and (4.21) (both dotdashed) including both the AGS and the SGS terms. Note the very good agreement which we find between the numerical data and the analytical theory, in particular also for those resonant values $2k_n\Delta = 2\pi M$ where the SGS contributions dominate (marked by arrows). Panel (b) shows the AGS predictions alone, i.e., when the SGS mechanism is omitted (both dotted). For all data shown the following parameter values were used: $\rho = 0.01$, $N_{\text{eff}} = 25$, $\sigma \approx 0.01$ and $k = 2.55/\pi$.

each of the two modes with $n = 1, 2$,

$$\Delta = \frac{\pi}{k_n} M = \frac{\pi}{\sqrt{k^2 - (n\pi/d)^2}} M \approx \begin{cases} 0.426\, M & n = 1\,, \\ 0.632\, M & n = 2\,. \end{cases} \tag{4.23}$$

At these well-defined values we not only find that the theory solely based on the AGS terms deviates from the numerics (see Fig. 4.3(b)), but that the additional SGS terms fill the missing gaps in the theory very well in terms of resonant contributions to the inverse attenuation lengths $1/L_{nn}$ (see Fig. 4.3(a)). Since maxima in the inverse attenuation length correspond to maxima in the reflection (i.e., minima in the transmission) we may thus conclude that the SGS mechanism leads to reflection resonances in the systems under study. While these resonances are clearly discernible already in the symmetric waveguides, we will find that they are even more pronounced in the antisymmetric waveguides that we investigate in the next section.

4.5.2 Antisymmetric profiles

In the case of antisymmetric waveguide profiles we have $\xi_{\downarrow}(x) = \xi_{\uparrow}(x)$, i.e., the waveguide width is constant throughout the waveguide (see Fig. 4.1). The situation is more complicated than in symmetric waveguides as inter-mode scattering is allowed here. A proper description of transmission thus has to incorporate both the intra- and the inter-mode scattering contributions. For mode-specific values of the transmission we again have to ask which scattering events contribute: consider, e.g., the transmission of a mode into itself, T_{nn}. In a perturbative treatment this quantity is determined by all scattering mechanisms that scatter the incoming mode n into the other mode or reverse its direction of propagation. This happens both through forward-scattering from mode n into the second available mode $n' \neq n$ as well as through backward scattering into any of the two modes $n' = 1, 2$. The attenuation length extracted from the transmission T_{nn} thus has to be compared to the predictions for the attenuation length L_{nn} which is given as $1/L_{nn} = 1/L^{(f)}_{n\neq n'} + 1/L^{(b)}_{nn} + 1/L^{(b)}_{n\neq n'}$. To be specific, we find

$$\frac{1}{L_{11}} = 16\pi^4 \frac{\sigma^2}{d^6} \frac{1}{k_1 k_2} \Big[W(k_1 + k_2) + W(k_1 - k_2) \Big] + \frac{\pi^4}{2} \frac{\sigma^4}{d^4} \frac{1}{k_1^2} S(2k_1) \, , \tag{4.24}$$

$$\frac{1}{L_{22}} = 16\pi^4 \frac{\sigma^2}{d^6} \frac{1}{k_1 k_2} \Big[W(k_1 + k_2) + W(k_1 - k_2) \Big] + 8\pi^4 \frac{\sigma^4}{d^4} \frac{1}{k_2^2} S(2k_2) \, . \tag{4.25}$$

The remaining question at this point is how to extract the attenuation lengths L_{nn} from the numerical data for T_{nn} when modes do not just localize as in the symmetric case. In the presence of inter-mode scattering, the wave injected into a disordered waveguide first propagates ballistically, then scatters diffusively and eventually localizes at very long waveguide lengths. For the two-mode waveguide considered here the diffusive regime is, however, not well-pronounced such that the crossover region between ballistic scattering and localization is comparatively narrow. Since, additionally, in the localized regime always the mode with the higher localization length ξ dominates [24], extracting mode-specific attenuation lengths is best achieved in the ballistic regime where the transmission decreases linearly with the system length L, $\langle T_{nn}\rangle \approx 1 - L/L_{nn}$. We will use this relation to extract the attenuation lengths L_{nn} from the disorder-averaged numerical transmission values $\langle T_{nn}\rangle$ in the ballistic regime. In practice, we use the criterion $\langle T_{nn}\rangle \in [0.9, 1]$ to ensure that the requirement of ballistic transport is satisfied (see Fig. 4.2(b)).

Fig. 4.4 shows the numerically obtained results for $1/L_{nn}$, including a comparison with the predictions from equations (4.24) and (4.25). In panel (a), both modes are displayed, with yellow full circles corresponding to $n = 1$ and blue diamonds to $n = 2$, respectively. In the case of antisymmetric waveguides a direct comparison of the numerical results for the two different modes reveals immediately where the SGS mechanism is at work (see Fig. 4.4(a)): Since the terms in Eqs. (4.24) and (4.25) associated with the AGS mechanism are identical for $1/L_{11}$ and $1/L_{22}$, any difference between the two attenuation lengths can be expected to be due to the SGS mechanism. The numerical results reveal that around $\Delta \approx 2.5$ an extended region opens up in which the two modes decouple and their attenuation lengths are significantly different. To clarify whether this decoupling is, indeed, due to the SGS mechanism, we compare the numerical results with the corresponding analytical predictions in figures 4.4(b,c). The agreement we obtain is, again, excellent, allowing us to identify the contributions of the SGS mechanism in detail. First of all, we find that the decoupling of modes is, indeed, due to the SGS mechanism as it is accurately reproduced when the SGS terms are included. Secondly, the theoretical analysis also predicts that the SGS terms should give rise to small resonant enhancements of the inverse attentuation length at the resonant values $2k_n\Delta = 2\pi M$ (see arrows in figures 4.4(b,c)). Also these predictions are very well reproduced by the numerical data.

To corroborate the consistency of our above arguments on forward- and backward-scattering contributions we also investigated the total mode transmissions $T_n = \sum_{n'}^{N_d} |t_{nn'}|^2$, which are now different from the mode-to-mode transmissions T_{nm} due to inter-mode scattering. In the ballistic regime the T_n

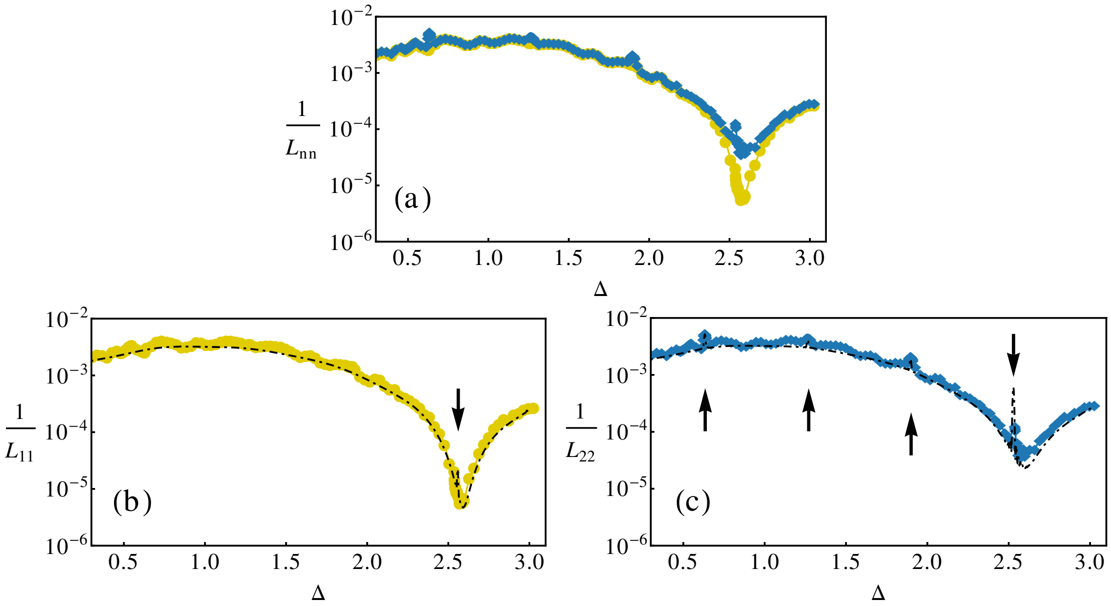

Figure 4.4: (a) Inverse partial attenuation length $1/L_{nn}$ versus the step width Δ, as obtained numerically for two-mode antisymmetric waveguides, with $1/L_{11}$ (yellow ●) and $1/L_{22}$ (blue ♦). We find very good agreement with the analytical expressions (4.24) and (4.25) that are included as dotdashed lines in panel (b) and (c), respectively (with $\rho = 0.03$, $N_{\text{eff}} = 25$, $\sigma \approx 0.01$ and $k = 2.55/\pi$). Arrows mark resonant values $2k_n\Delta = 2\pi M$ which indicate locally dominating SGS contributions.

should be determined by backward-scattering alone, since forward-scattering just redistributes the flux which is incoming in one mode over all available right-moving modes. Since, however, the right-moving modes are summed over in the expression for T_n, any influence of forward-scattering drops out in our perturbative treatment. Only when taking into account higher-order forward/backward-scattering events (as in the diffusive or localized regime) the influence of forward-scattering should be noticeable also on the T_n. In the ballistic regime, however, we should have $\langle T_n \rangle \approx 1 - L/L_n$, with $1/L_n = 1/L^{(b)}_{nn} + 1/L^{(b)}_{n\neq n'}$ such that the mode-specific attentuation lengths read as follows,

$$\frac{1}{L_1} = 16\pi^4 \frac{\sigma^2}{d^6} \frac{W(k_1+k_2)}{k_1 k_2} + \frac{\pi^4}{2} \frac{\sigma^4}{d^4} \frac{S(2k_1)}{k_1^2}\,, \tag{4.26}$$

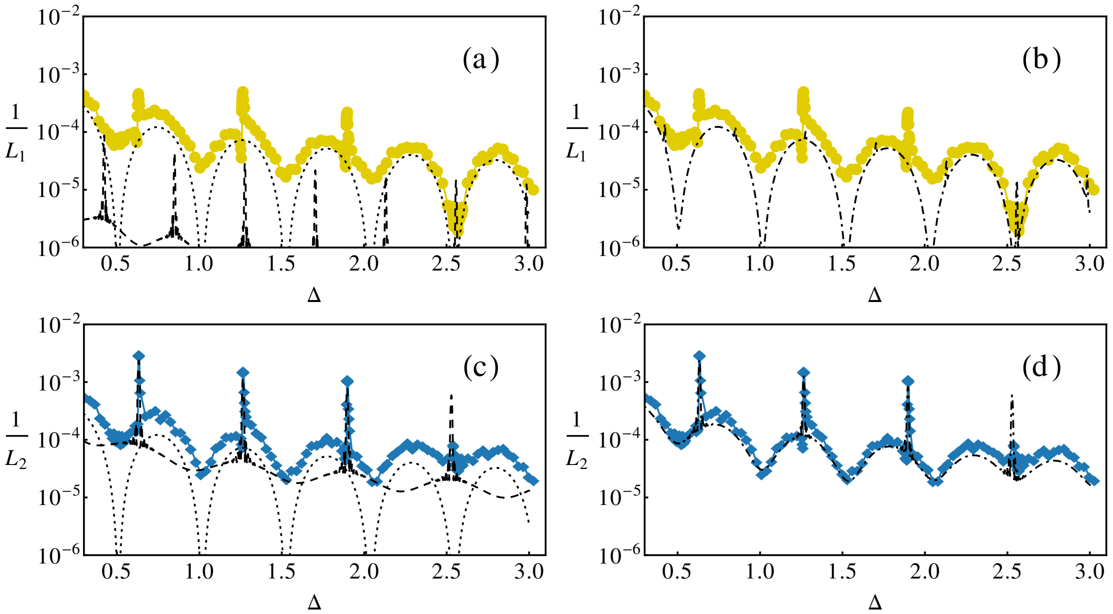

Figure 4.5: Inverse partial attenuation length $1/L_n$ versus step width Δ, as obtained numerically for two-mode antisymmetric waveguides ($\rho = 0.03$, $N_{\text{eff}} = 25$, $\sigma \approx 0.01$ and $k = 2.55/\pi$). Top row: The numerical results for $1/L_1$ (yellow ●) are compared in (a) with the AGS (dotted) and SGS (dashed) terms of Eq. (4.26) plotted separately. In (b) both scattering mechanisms are combined (dotdashed). Bottom row: Numerical values for $1/L_2$ (blue ⧫) are compared in (c) with the AGS (dotted) and SGS (dashed) terms of Eq. (4.27) plotted separately. In (d) both scattering mechanisms are combined (dotdashed). We find a quantitative agreement with the predictions for $1/L_2$ (panel (d)), while a sizeable discrepancy is observed between numerics and analytical curves for the first mode in (b).

$$\frac{1}{L_2} = 16\pi^4 \frac{\sigma^2}{d^6} \frac{W(k_1 + k_2)}{k_1 k_2} + 8\pi^4 \frac{\sigma^4}{d^4} \frac{S(2k_2)}{k_2^2} \, . \tag{4.27}$$

To extract the corresponding attenuation lengths L_n from our numerics, we use $\langle T_n \rangle \approx 1 - L/L_n$ as a prescription to obtain L_n in the ballistic regime, characterized by $\langle T_n \rangle \in [0.9, 1]$. The agreement which we find between the predictions for $1/L_n$ and our numerical results is, in parts, remarkably good (see Fig. 4.5). In particular, a comparison with the expression for $1/L_2 = 1/L_2^{(b,AGS)} + 1/L_2^{(b,SGS)}$ in Fig. 4.5(d) reveals an excellent agreement between theory and simulation. With the help of Fig. 4.5(c), it can be understood that the SGS mechanism contributes by way of two distinct effects: most obviously, we obtain peaks indicating enhanced resonant back-scattering in our system for $2k_2\Delta = 2\pi M$, with M integer. Note that these peaks in $1/L_2$ lead to back-scattering lengths which are about one order of magnitude larger than the (conventional) AGS background. The SGS mechanism can, however, also be identified as a finite contribution to the inverse scattering length at values $(k_1 + k_2)\Delta = 2\pi M'$, exactly where the AGS term in equation (4.27) vanishes. It is therefore the SGS mechanism which prevents a perfect transparency of the waveguide.

When comparing, however, the first mode data to Eq. (4.26), we find that the numerical curve cannot be fully reproduced by the corresponding analytical expression for $1/L_1$ (see Fig. 4.5(b)). While the AGS contribution $1/L_1^{(b,AGS)}$ is identical to $1/L_2^{(b,AGS)}$ in antisymmetric waveguides, the SGS contribution $1/L_1^{(b,SGS)}$ is a factor 16 *smaller* (see Fig. 4.5(a)). How can this be reconciled with the numerical finding that $1/L_1$ and $1/L_2$ are mostly equal?

We suspect higher-order terms in scattering (that should not be confused with higher orders in the boundary roughness strength σ) to be responsible for these deviations which go beyond the first order nature of the underlying theory, where the incident wave is assumed to scatter only once before leaving the scattering region. Our aim in the following will be to include such higher-order contributions based on the knowledge of the first-order scattering lengths. Consider here, e.g., the scattering length of the first mode, L_1, which, as we have assumed so far, is attenuated by back-scattering from the first mode into the first ($L_{11}^{(b)}$) and into the second mode ($L_{12}^{(b)}$), respectively. The next higher order contribution would be given by forward scattering into the second mode (governed by $L_{12}^{(f)}$), followed by back-scattering from the second mode into the first ($L_{21}^{(b)}$) or into the second mode ($L_{22}^{(b)}$). Based on the magnitude of the involved scattering lengths the forward-scattering $1 \leftrightarrow 2$ occurs much more frequently than a back-scattering event, i.e., the propagating wave undergoes forward scattering multiple times before it is backscattered (see figure 4.6). Consequently, the modes can be assumed to be almost equally distributed between mode 1 or 2 be-

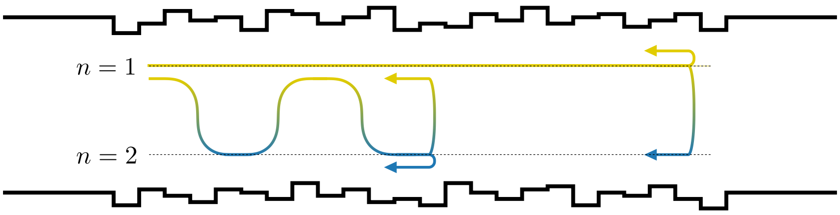

Figure 4.6: Illustration of scattering processes of different order. Two processes are shown that attenuate the forward moving first mode, $n = 1$. One process is of first order and consists just of a single back-scattering event from the first mode into any of the two backward-moving modes. However, since in the case we consider, forward-scattering $1 \leftrightarrow 2$ is dominant as compared to backscattering, it is much more likely that the first mode undergoes multiple scattering events in forward direction before backscattering occurs. Such terms can thus yield a sizeable contribution although they formally are of higher-order in the number of scattering events which they undergo.

fore back-scattering occurs. As a result, the back-scattering contribution should also be composed of both modes in equal shares. Since the forward-scattering occurs in series, the back-scattering in parallel, this translates into an additional *effective* second order term for the inverse scattering length,

$$\frac{1}{L^{(2,\text{eff})}} = \frac{1}{L^{(f)} + \frac{1}{\frac{1}{2}\left(\frac{1}{L^{(b)}_{21}} + \frac{1}{L^{(b)}_{22}} + \frac{1}{L^{(b)}_{12}} + \frac{1}{L^{(b)}_{11}}\right)}}\,, \tag{4.28}$$

with $L^{(f)} \equiv L^{(f)}_{12} = L^{(f)}_{21}$. Eq. (4.28) represents a simple qualitative estimate of second order contributions to the inverse scattering lengths, and we expect that this expression can be made more quantitative by employing a full-fledged diagrammatic theory. Note that this correction term does not feature an explicit mode dependence since the redistribution of the flux is the same for both propagating modes.

Based on the above, the total inverse scattering lengths can be written as the sum of the following contributions,

$$\begin{aligned} \frac{1}{L_n} &= \frac{1}{L^{(b)}_{nn}} + \frac{1}{L^{(b)}_{nn'\neq n}} + \frac{1}{L^{(2,\text{eff})}}\,, \\ &= \frac{1}{L^{(1)}_{n}} + \frac{1}{L^{(2,\text{eff})}}\,, \end{aligned} \tag{4.29}$$

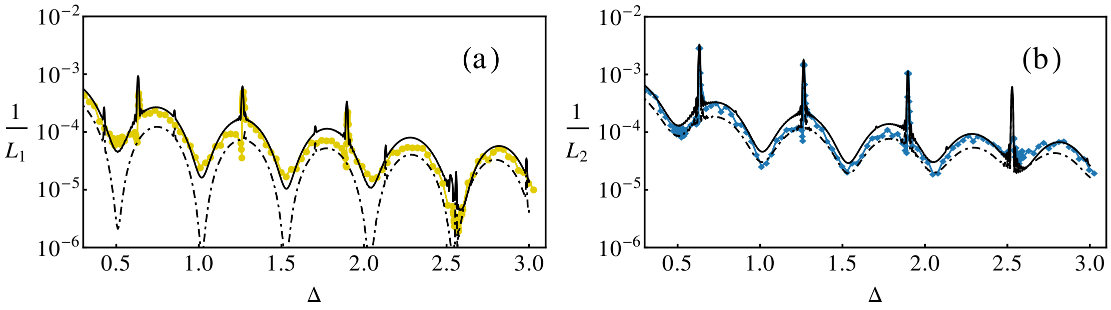

Figure 4.7: Inverse partial attenuation length $1/L_n$ versus step width Δ, as obtained numerically for two-mode antisymmetric waveguides ($\rho = 0.03$, $N_{\text{eff}} = 25$, $\sigma \approx 0.01$ and $k = 2.55/\pi$). The inverse attenuation lengths are shown in (a) for the first mode, $1/L_1$ (yellow •) and in (b) for the second mode $1/L_2$ (blue ♦). The analytical curves are displayed without (dotdashed) and including (solid) second order corrections of Eq. (4.28). Note the quantitative agreement that is achieved through the inclusion of higher-order scattering terms.

where the superscripts (i) denote the order of the contribution. A comparison of this result with the numerical data is shown in Fig. 4.7, yielding much better agreement than without the second-order contributions. In particular, we find (see Fig. 4.7(a)) that incorporating the new effective scattering length $1/L^{(2,\text{eff})}$ resolves the discrepancy we found earlier for the inverse attenuation length of the first mode, $1/L_1$. This result now also allows us to understand the similarity between the numerical data for $1/L_1$ and $1/L_2$ while the first-order SGS contributions are very different for these two modes: the reason is apparently the strong intermode coupling induced by efficient forward-scattering $L^{(f)}$ which lets the inverse attenuation length of the first mode $1/L_1$ inherit the behavior of the second mode $1/L_2$. Correspondingly, the reason for the decoupling between the modes in Fig. 4.7 at around $\Delta \approx 2.5$ can also now be identified: in this parameter window the intermode scattering strength is strongly reduced, allowing the different attenuation lengths to maintain their mode-specific values. Everywhere else (outside this parameter window) the behavior of $1/L_1$ is governed by $1/L_2$.

4.5.3 Nonsymmetric profiles

Nonsymmetric waveguides represent the most general case for waveguide symmetries since, in contrast to the previous sections, both boundaries are not restricted by any symmetry requirement, i.e., we have $\xi_{\uparrow}(x) \neq \xi_{\downarrow}(x)$. Turning at first to the partial attenuation lengths, table 4.1 and Eqs. (4.17) and (4.18) allow us to put forward the corresponding expressions for $1/L_{nn} = 1/L^{(f)}_{n\neq n'} + 1/L^{(b)}_{nn} + 1/L^{(b)}_{n\neq n'}$, which are given by

$$\begin{aligned} \frac{1}{L_{11}} &= 2\pi^4 \frac{\sigma^2}{d^6}\frac{1}{k_1^2} W(2k_1) + 8\pi^4 \frac{\sigma^2}{d^6}\frac{1}{k_1 k_2}\Big[W(k_1+k_2) + W(k_1-k_2)\Big] \\ &\quad +20\frac{\sigma^4}{d^4}\frac{1}{k_1^2} S(2k_1) + \frac{(9+6\pi^2+10\pi^4)}{72\pi^4}\frac{\sigma^2}{d^6}\frac{1}{k_1 k_2}\Big[S(k_1+k_2) + S(k_1-k_2)\Big]\,, \end{aligned} \tag{4.30}$$

$$\begin{aligned} \frac{1}{L_{22}} &= 32\pi^4 \frac{\sigma^2}{d^6}\frac{1}{k_1^2} W(2k_2) + 8\pi^4 \frac{\sigma^2}{d^6}\frac{1}{k_1 k_2}\Big[W(k_1+k_2) + W(k_1-k_2)\Big] \\ &\quad +20\frac{\sigma^4}{d^4}\frac{1}{k_1^2} S(2k_2) + \frac{(9+24\pi^2+160\pi^4)}{72\pi^4}\frac{\sigma^2}{d^6}\frac{1}{k_1 k_2}\Big[S(k_1+k_2) + S(k_1-k_2)\Big]\,. \end{aligned} \tag{4.31}$$

We can also immediately write down the corresponding total scattering lengths $1/L_n = 1/L^{(b)}_{nn} + 1/L^{(b)}_{n\neq n'}$, where forward-scattering, i.e., $W(k_1-k_2)$ and $S(k_1-k_2)$, is not considered since it does not attenuate the total transmission T_n of the corresponding mode,

$$\begin{aligned} \frac{1}{L_{1}} &= 2\pi^4 \frac{\sigma^2}{d^6}\frac{1}{k_1^2} W(2k_1) + 8\pi^4 \frac{\sigma^2}{d^6}\frac{1}{k_1 k_2} W(k_1+k_2) \\ &\quad +20\frac{\sigma^4}{d^4}\frac{1}{k_1^2} S(2k_1) + \frac{(9+6\pi^2+10\pi^4)}{72\pi^4}\frac{\sigma^2}{d^6}\frac{1}{k_1 k_2} S(k_1+k_2)\,, \end{aligned} \tag{4.32}$$

$$\begin{aligned} \frac{1}{L_{2}} &= 32\pi^4 \frac{\sigma^2}{d^6}\frac{1}{k_1^2} W(2k_2) + 8\pi^4 \frac{\sigma^2}{d^6}\frac{1}{k_1 k_2} W(k_1+k_2) \\ &\quad +20\frac{\sigma^4}{d^4}\frac{1}{k_1^2} S(2k_2) + \frac{(9+24\pi^2+160\pi^4)}{72\pi^4}\frac{\sigma^2}{d^6}\frac{1}{k_1 k_2} S(k_1+k_2)\,. \end{aligned} \tag{4.33}$$

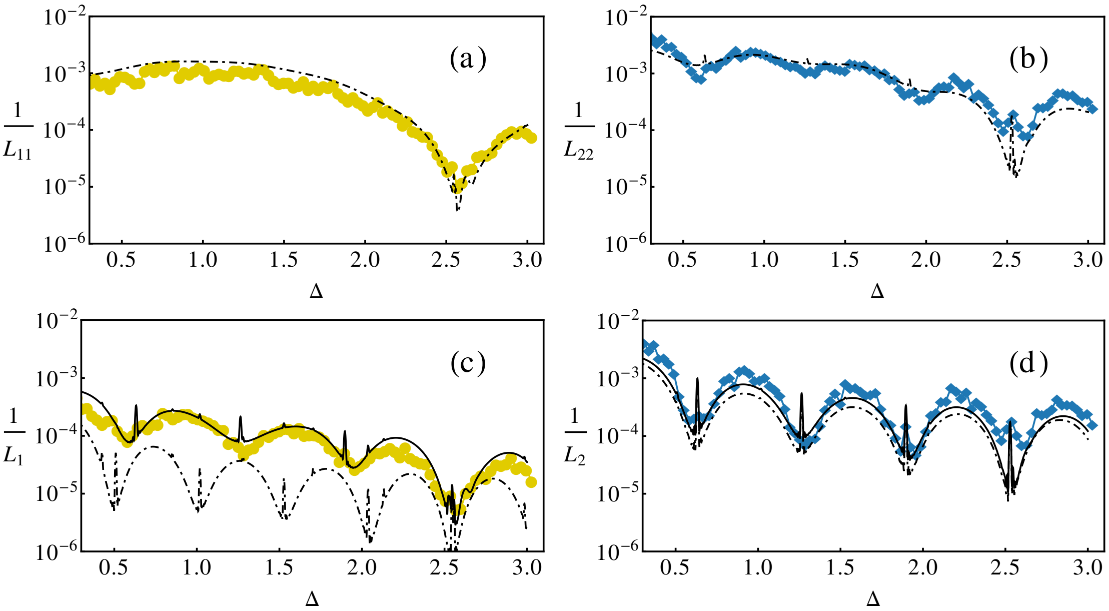

Figure 4.8: Inverse partial attenuation length $1/L_{nn}$ versus step width Δ, as obtained numerically for two-mode nonsymmetric waveguides ($\rho = 0.03$, $N_{\text{eff}} = 25$, $\sigma \approx 0.01$ and $k = 2.55/\pi$). Top row: The numerical results for (a) $1/L_{11}$ (yellow •) and (b) $1/L_{22}$ (blue ♦) are shown. The corresponding analytical expressions (4.30) and (4.31) are shown in black (dotdashed), indicating very good agreement with the numerical data. Bottom row: Here the numerical data for (c) $1/L_1$ (yellow •) and (d) $1/L_2$ (blue ♦) are compared with the corresponding analytical terms without (dotdashed) and including (solid) second order corrections. Even though nonsymmetric waveguides represent the most general of waveguide symmetries, we find a remarkably good agreement with our numerics.

As can be seen from these equations for $1/L_n$ and $1/L_{nn}$, intra- and intermode as well as the AGS and the SGS scattering lengths now all contribute to the scattering process, in contrast to symmetric or antisymmetric waveguides where the coefficient matrices $A_{nn'}$ and $B_{nn'}$ from table 4.1 feature zeros at symmetry-specific entries. This fact underlines the role of nonsymmetric waveguides as the most general case to study in surface-corrugated systems.

For comparison with the numerical data we determine the quantities $1/L_{nn}$ and $1/L_n$ by means of a fit to the transmission in the ballistic regime, $\langle T_{nn} \rangle \approx 1 - L/L_{nn}$ and $\langle T_n \rangle \approx 1 - L/L_n$, in complete analogy to antisymmetric waveguides in the preceding section. Fig. 4.8 shows a comparison between numerics and theory for nonsymmetric two-mode waveguides. Concentrating at first on $1/L_{nn}$ (first row in Fig. 4.8), we note that we find very good agreement between the theoretical and the numerical curves for both the first and the second mode. Similar to the corresponding results in antisymmetric waveguides, a peak at $\Delta \approx 2.5$ is clearly visible for $1/L_{22}$ and, more hidden, also in $1/L_{11}$. The other peaks emerging in the analytical expression for $1/L_{22}$ can also be found in our numerical data (Fig. 4.8(b)), albeit slightly more concealed than in the previous section. The positions of these resonances can again be determined from the resonance condition in Eq. (4.23).

Turning to the assessment of our results for $1/L_n$ we can now, with the knowledge from the last section, also take into account higher-order scattering contributions given by Eq. (4.28). Figures 4.8(c-d) show a comparison of the analytical expressions for the attenuation lengths $1/L_n$ with the numerical data. Note that here we also include the first order predictions as dotdashed lines. As found before in antisymmetric two-mode waveguides, $1/L_2$ is already captured very well by equation (4.33). The arc-structure driven by the AG scattering mechanism shows again a remarkable agreement with the numerical curve, the same is true at resonant points where we find dominating contributions of the SGS mechanism. As before, a more elaborate argument incorporating second-order terms in the scattering is needed for explaining the behavior of $1/L_1$ (Fig. 4.8(c)). Taking only first-order expressions from Eq. (4.32) into account results in theoretical predictions which deviate from our numerical data by about one order of magnitude. Moreover, the period of the oscillations in $1/L_1$ does not seem to coincide with the analytical predictions. Only after allowing for higher-order terms in $1/L_n$, i.e., where forward-scattering followed by back-scattering is taken into account by employing Eq. (4.28), an agreement can be reestablished (Fig. 4.8(c) solid line).

Note that the reflection resonances which we observe for nonsymmetric and symmetric waveguides are not as pronounced as in the case of antisymmetric waveguides. This can be understood by the fact that the cross-section of an antisymmetric waveguide remains constant throughout the entire waveguide length such that also the wavenumber k_x does not change in the course of propagation. As a consequence, the resonance condition $k\Delta = 2\pi M$, with M integer, can be fulfilled very accurately in antisymmetric waveguides, while for waveguides with different symmetries the resonance condition is fulfilled only on average.

CHAPTER 5

Surface scattering and band gaps in rough waveguides

In the previous chapter, we have shown that we could successfully put forward a quantitative theory to describe the transmission properties of a random yet specific surface profile by extending the surface scattering theory [107], in full agreement with our numerical simulations. This theory, however, allows to accomplish much more, namely to turn the problem around and *induce* desired transmission properties by *engineering* and *designing* the boundary $\xi(x)$. Also, even though we have seen that the surface-scattering theory may be applied to very long wires, here we may also test if it is fit to describe transport in very short systems. This challenging task was undertaken in collaboration with Otto Dietz, Ulrich Kuhl, Hans-Jürgen Stöckmann, Felix M. Izrailev, Nykolay M. Makarov as well as Florian Libisch [29]. My contribution to this work was to assist with the interpretation of the experimental data, especially in view of the analytical scattering theory.

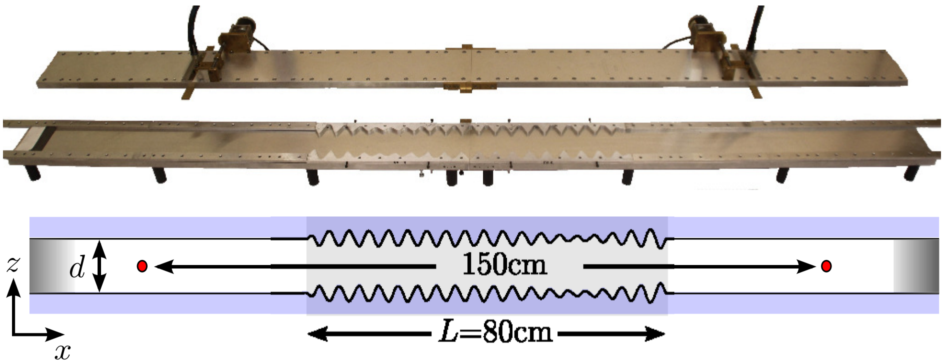

Figure 5.1: Experimental setup with exchangeable rough boundaries. The photo shows the considered waveguide with the surface disordered region in the center and the lifted top plate. Step motors are attached to the top plate to shift the input and output antenna in z-direction. Absorbers at both ends suppress reflection (indicated in the sketch below). This figure was taken from Ref. [29].

5.1 Strategy

In this work, the amplitude-scattering term was designed such that one finds a predetermined transmission gap, corresponding to large values of the attenuation length of the second mode, $1/L_2$, in a previously defined frequency interval $\Delta\nu$. From the specific form of the roughness-height power-spectrum

$$W(k_x) = \left| \int_{-\infty}^{\infty} \xi(x) e^{-ik_x x} \mathrm{d}x \right|^2 \equiv \mathcal{F}_{\mathrm{PS}} \left[\xi(x) \right] \ , \tag{5.1}$$

the inverse problem of finding the corresponding profile function $\xi(x)$, i.e.,

$$\xi(x) = \mathcal{F}_{\mathrm{PS}}^{-1} \left[W(k_x) \right] \ , \tag{5.2}$$

was solved by means of a convolution method (see Ref. [29]). The profile associated with the engineered transmission characteristics can be seen Fig. 5.1, which corresponds to a symmetric waveguide in a sense that the waveguide is symmetric with respect to the longitudinal waveguide axis. Note that, in contrast to the microwave channel in section 3.14, the present waveguide is not adiabatic.

In a two-mode, symmetric waveguide, both modes are not coupled[1] and, thus, each mode can be considered isolated; the only mechanism that can depopulate a given mode is thus by resonant intra-mode backscattering, described by the modal backscattering lengths

---

[1] Consider here, e.g., the effective model in Eqs. (A.24), with the relative boundary phase in Eq. (A.25) set to $\vartheta = \pi$. This immediately results in a diagonal Hamiltonian with vanishing coupling g.

$$\frac{1}{L_n^b} = \frac{1}{L_n^{\mathrm{b,AGS}}} + \frac{1}{L_n^{\mathrm{b,SGS}}} , \tag{5.3}$$

where the AGS (SGS) term is proportional to $W(2k_n)$ ($S(2k_n)$). Thus, since only two terms contribute, all gaps in the respective transmission spectrum outside the frequency range $\Delta\nu$ can be expected to originate from the square-gradient scattering mechanism for the specific profile (5.2), given by

$$S(k_x) = \mathcal{F}_{\mathrm{PS}}\left[\xi'^2(x)\right] . \tag{5.4}$$

If, however, square-gradient scattering is to be neglected, we would observe only the AGS gap in the respective transmission curve. The two terms that contribute to the attenuation length $1/L_2^{\mathrm{b}}$ are plotted in Fig. 5.2. Most notably, we see that if the wavenumber of the second mode, k_2, is approximately equal to $75\ \mathrm{m}^{-1}$, the AGS mechanism dominates (per construction), while in the small wavenumber limit, the SGS mechanism prevails.

5.2 Results

Experimental data obtain by the Stöckmann group in Marburg, as well as numerical results can be found in Fig. 5.3. Focussing on the transmission of the second mode, T_2, we observe the following basic structure: For low and high frequencies a transmission gap is observed, interrupted by a transmission plateau for intermediate frequencies. Since the profile was designed such that AGS mainly contributes to backscattering only in a short frequency range, the rightmost gap can be associated with the AGS mechanism (shown in blue color). Furthermore, we see in yellow a transmission gap that can be unambiguously attributed to the SGS mechanism – the AGS mechanism alone would only account for the dotted curve in Fig. 5.3. This data we put forward here provides

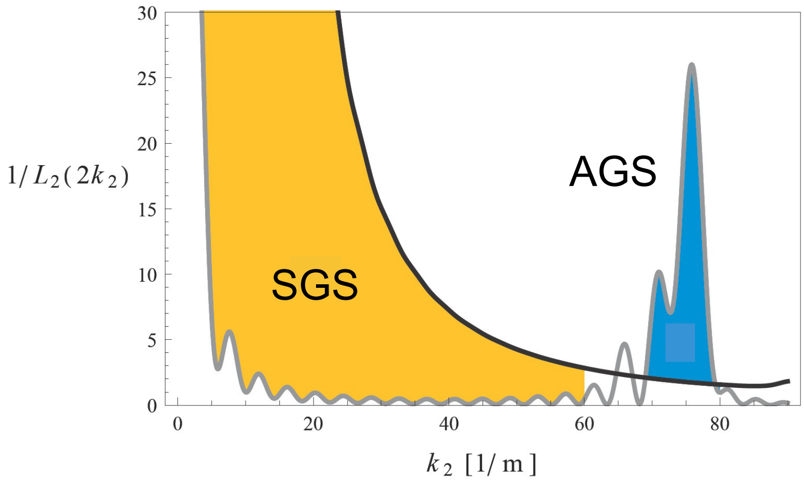

Figure 5.2: The inverse backscattering lengths $1/L_2^{b,AGS}$ (gray curve) and $1/L_2^{b,SGS}$ (black curve) for the second mode, $n = 2$ are shown. The corresponding power spectra are calculated directly from the rough boundaries shown in Fig. 5.1. Regions of dominating SGS and AGS mechanisms are shaded. This figure and caption was taken from Ref. [29].

further unambiguous proof that a theory neglecting the SGS contribution cannot fully account for all major ingredients in surface scattering.

Finally, one may notice a shift in the wavenumber of the transmission characteristics in Fig. 5.3 between theory (solid black line) and the experiment (grey line). This shift can be attributed to a value of the surface roughness strength σ that is too large (here, σ is almost 10% of the wire width). Since the analytical theory employed here is perturbative in σ, we have numerically recalculated the transmission curves for a waveguide with a surface roughness strength that is reduced by 50%. Then, a much better agreement is obtained between the numerics and analytical predictions (see Ref. [29] for details).

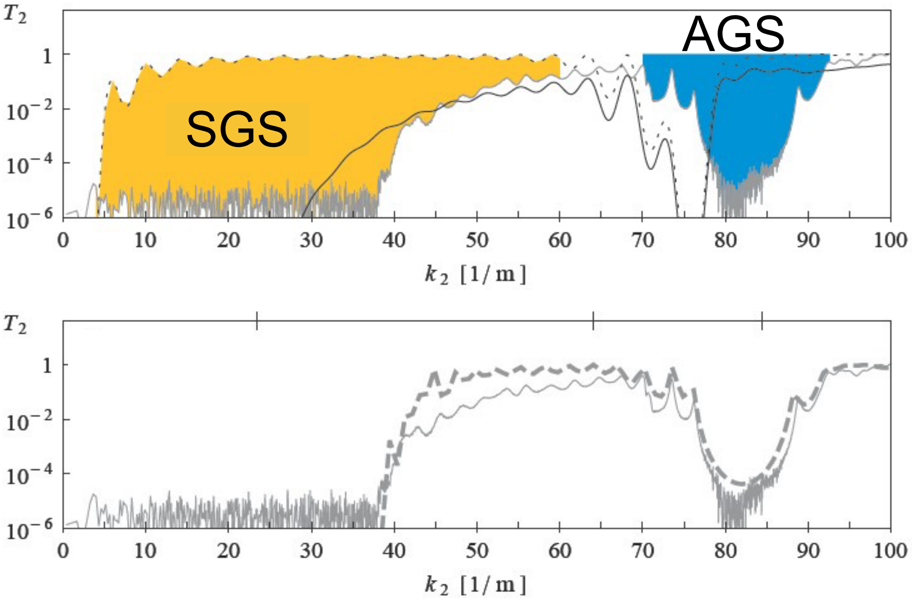

Figure 5.3: Top: Measured transmittance T_n (gray curve), for the second mode ($n = 2$). The corresponding theoretical prediction is shown as solid black curve (see Ref. [29] for details). For the dotted line the SGS is neglected explicitly. The colored areas indicate the gaps caused by the dominating scattering mechanism: in blue (yellow) regions the AGS (SGS) mechanism prevails. Bottom: comparison between the measured (solid) and numerical (dashed) transmission intensity. This figure and caption was taken from Ref. [29].

CHAPTER 6

Conclusion and outlook

In summary, we have investigated how waveguides with boundary modulations can be successfully utilized to control wave transmission and reflection by engineering both their shape and their absorbing potential.

More precisely, we have demonstrated how the encircling of an exceptional point can be fully realized in two-mode waveguides while staying faithful to the full dynamical nature of this problem. The emergence of inherent non-adiabatic contributions allowed us to build an asymmetric mode-switch that has been realized successfully in a corresponding microwave experiment, and that may be used in real-world applications to obtain direction-dependent modal transport. In this way, we have devised a notably platform-independent approach to mode switching that is implementable not just for microwaves, but readily applicable also to light, acoustic or matter waves. In particular, we emphasize that our strategy provides a general concept for devices such as those reported recently on photonic mode conversion [65]. Rather than a breaking of reciprocity [70], we show here that a successful working principle for robust and efficient mode switching in waveguides is given through an effective encircling of exceptional points. Future work may focus on the implementation of our concept on the nanoscale, like, e.g., in photonic systems as in Ref. [65] or exciton-polariton devices as implemented in Ref. [23]. Furthermore, our restrictions to two-mode waveguides may be lifted, leading, potentially, to exceptional points of higher orders [45], and would allow the implementation of generalized transition schemes like the stimulated Raman adiabatic passage (STIRAP) [18].

In the second part of this thesis, we have investigated dissipationless waveguides that feature a step-like surface disorder supporting two propagating modes [28]. Our study reveals a resonant enhancement of wave reflection in these systems, an effect which has, to the best of our knowledge, not yet been observed earlier, despite the popularity of the employed waveguide model. To manifest this effect we performed extensive numerical calculations using a waveguide model with symmetric, antisymmetric and nonsymmetric random profiles, respectively. We show that this previously neglected contribution is very robust and survives ensemble-averaging of the surface roughness. At the resonance conditions, which we obtain fully analytically, we find up to an order-of-magnitude enhancements of the reflection. Not only do our results constitute the first evidence of these resonances in waveguides, but they also provide the first unambiguous signatures of the square-gradient scattering mechanism in waveguides with arbitrary symmetries. The very good agreement which we find between numerical and analytical results provides a solid basis for a general understanding of wave transmission through waveguides with surface roughness. Combined with the joint microwave experiment that showed the importance of the square-gradient scattering mechanism in symmetric waveguides [29], this knowledge may be particularly important in view of experimental possibilities to engineer the transmission characteristics of waveguides through their surface profiles [113, 114].

APPENDIX A

Effective 2×2 model derivation

A.1 Model

Wave propagation with frequency ω in a 2D waveguide is described by the complex scattering state $\varphi(x, y, t) = \phi(x, y)e^{-i\omega t}$ satisfying the Helmholtz equation

$$\Delta\phi(x, y) + \varepsilon(x, y)\frac{\omega^2}{c^2}\phi(x, y) = 0 \; , \tag{A.1}$$

with the speed of light c and the complex dielectric function ε which is modelled by $1 + i\eta/k$ in the waveguide's interior. Here, $k = \omega/c$ denotes the wavenumber. The imaginary part of ε with the dissipation coefficient η describes the losses originating from the interaction with the top and bottom waveguide walls or an absorbing material in the waveguide itself [115]. We emphasize that the applicability of Eq. (A.1) is not limited to the electromagnetic domain, but may also describe the propagation of, e.g., sound or matter waves.

A.2 Floquet-Bloch picture

In the following we will consider a metallic waveguide, which implies Dirichlet boundary conditions at the waveguide boundary. Considering periodic functions both at the lower and the upper waveguide boundary, at $y = \xi_{\downarrow}(x)$ and

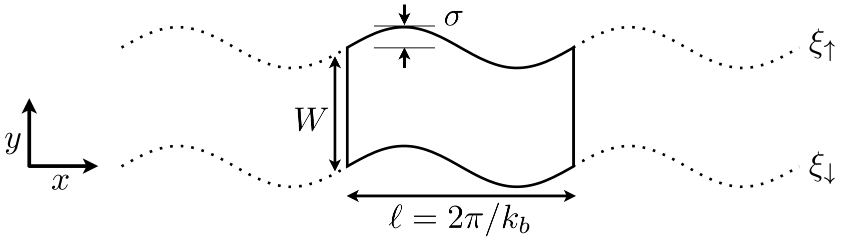

Figure A.1: A periodic waveguide with width W, boundary wavenumber k_b and undulation amplitude σ. A single unit cell of length $\ell = 2\pi/k_b$ is highlighted by solid lines.

$y = \xi_\uparrow(x)$, respectively, these conditions thus become

$$\phi\Big(x, \xi_i(x)\Big) = 0\ , \quad i = \downarrow, \uparrow\ ,$$

$$\xi_\downarrow(x) = \sigma \sin k_b x \ \text{ and } \ \xi_\uparrow(x) = W + \sigma \sin(k_b x + \vartheta)\ , \tag{A.2}$$

where k_b and σ denote the boundary wavenumber and amplitude, respectively; W is the waveguide width and the constant parameter $\vartheta \in (-\pi, \pi]$ corresponds to the phase shift between the upper and lower boundary. For example, $\vartheta = 0$ corresponds to a periodic waveguide with constant width W (see Fig. A.1 for an illustration).

In a uniform waveguide with no losses, i.e., $\sigma = \eta = 0$, the propagating waves are given by the modes

$$\phi_n(y) = \sin\left(\frac{n\pi}{W} y\right) e^{ik_n x}, \quad k_n = \sqrt{k^2 - \left(\frac{n\pi}{W}\right)^2}\ , \quad n = 1, 2, \ldots \tag{A.3}$$

We assume that there are only two propagating modes with $n = 1$ and 2, which determine the wavenumber interval as $2 < kW/\pi < 3$. In a periodic waveguide, when $\sigma > 0$, the propagating modes are described by the Bloch solutions

$$\phi(x, y) = \Lambda(x, y)\, e^{iKx}, \tag{A.4}$$

where $\Lambda(x, y)$ is an x-periodic function with period $\ell = 2\pi/k_b$, i.e., $\Lambda(x + \ell, y) = \Lambda(x, y)$. The Bloch wavenumber K is defined up to an integer multiple of the boundary wavenumber k_b, i.e., $K \pmod{k_b}$. In this work, we study effects related to a degenerate (EP) Bloch wavenumber K, and our first goal is to find values of the parameters corresponding to the EP degeneracy.

A.3 Perturbative approach

To accomplish this task we consider the boundary wavenumber equal to

$$k_b = k_r + \delta \ , \tag{A.5}$$

where the resonant wavenumber k_r, at which modes 1 and 2 strongly scatter into each other, is given by

$$k_r = k_1 - k_2 \ , \tag{A.6}$$

and δ is the detuning parameter. When $\sigma = \eta = \delta = 0$, we have $k_b = k_r$ and a superposition of the two corresponding modes (A.3) propagating in the positive x-direction can be written as

$$\phi^0(x,y) = \Lambda^{(0)}(x,y)e^{ik_1x} \tag{A.7}$$

with

$$\Lambda^{(0)}(x,y) = a_1 \sin\left(\frac{\pi}{W}y\right) + a_2 \sin\left(\frac{2\pi}{W}y\right) e^{-ik_rx} \tag{A.8}$$

and arbitrary coefficients a_1 and a_2. Here, the function $\Lambda^{(0)}(x,y)$ is x-periodic with period $\ell_0 = 2\pi/k_r$. Expression (A.7) can be interpreted as a degenerate Bloch mode of multiplicity two with the wavenumber $k_1 = k_2 \pmod{k_r}$. This is a diabolical point (DP) degeneracy (typical for Hermitian systems) at which only the Bloch wavenumbers merge, while the mode functions remain different, see, e.g., Ref. [1].

In this section, we find the first-order approximation for Bloch modes when the boundary amplitude σ, the detuning parameter δ and the dissipation coefficient η are small quantities of the same order. These Bloch modes are small perturbations of (A.7) and, thus, can be written in the form (A.4) with

$$\Lambda(x,y) = \Lambda^{(0)}(x,y) + \Lambda^{(1)}(x,y), \quad K = k_1 + s, \tag{A.9}$$

where $\Lambda^{(1)}(x,y)$ and s are small corrections of the same order as σ, δ and η, see, e.g., Ref. [116]. Using Eq. (A.9) in (A.4), we obtain the Bloch mode in the form

$$\phi(x,y) = [\Lambda^{(0)}(x,y) + \Lambda^{(1)}(x,y) + isx\Lambda^{(0)}(x,y)]e^{ik_1x}, \tag{A.10}$$

where the second-order small terms in σ, δ and η and in any of their products were neglected. Substituting (A.10) into (A.1) and neglecting again all second-order terms, we get the equation

$$\Lambda^{(1)}_{xx} + 2ik_1\Lambda^{(1)}_x + \Lambda^{(1)}_{yy} + \left(\frac{\pi}{W}\right)^2 \Lambda^{(1)} + 2is(\Lambda^{(0)}_x + ik_1\Lambda^{(0)}) + ik\eta\Lambda^{(0)} = 0 \ , \quad \text{(A.11)}$$

with $f_n \equiv \frac{\partial}{\partial n} f$ and $f_{nn} \equiv \frac{\partial^2}{\partial n^2} f$. Note that zero-order terms are canceled in (A.11) because $\Lambda^{(0)}$ is a solution of the unperturbed problem.

In the first-order approximation, we can transfer the boundary conditions (A.2) to $y = 0$ and $y = W$ by expanding ϕ in Taylor series as

$$\begin{aligned} 0 &= \phi + \phi_y \sigma \sin k_r x + O(\sigma^2) \quad \text{at} \quad y = 0 \ , \\ 0 &= \phi + \phi_y \sigma \sin(k_r x + \vartheta) + O(\sigma^2) \quad \text{at} \quad y = W \ . \end{aligned} \quad \text{(A.12)}$$

Using Eq. (A.10) in (A.12), and taking into account that $\Lambda^{(0)} = 0$ at $y = 0$ and W, we obtain

$$\begin{aligned} \Lambda^{(1)} &= -\sigma\Lambda^{(0)}_y \sin k_r x \quad \text{at} \quad y = 0, \\ \Lambda^{(1)} &= -\sigma\Lambda^{(0)}_y \sin(k_r x + \vartheta) \quad \text{at} \quad y = W \ , \end{aligned} \quad \text{(A.13)}$$

where second-order terms were neglected. The function $\Lambda(x, y)$ must be x-periodic with period

$$\ell = \frac{2\pi}{k_b} = \ell_0 + \ell_1\delta + O(\delta^2), \quad \ell_0 = \frac{2\pi}{k_r}, \quad \ell_1 = -\frac{2\pi}{k_r^2} \ . \quad \text{(A.14)}$$

Using Eq. (A.9), the first-order periodicity condition for $\Lambda(x, y)$ yields

$$\left(\Lambda^{(1)}\right)_{x=0} = \left(\Lambda^{(0)}_x \ell_1\delta + \Lambda^{(1)}\right)_{x=\ell_0} \ , \quad \text{(A.15)}$$

where we used $\Lambda^{(0)}(x = 0, y) = \Lambda^{(0)}(x = \ell_0, y)$. Similarly, the periodicity condition for the derivative Λ_x yields

$$\left(\Lambda^{(1)}_x\right)_{x=0} = \left(\Lambda^{(0)}_{xx} \ell_1\delta + \Lambda^{(1)}_x\right)_{x=\ell_0} \ . \quad \text{(A.16)}$$

The linearized equation (A.11) can now be solved for s and Λ_0. For this purpose, we multiply it with $\sin\left(\frac{\pi}{W}y\right)$ and integrate with respect to x and y,

$$\begin{aligned}\int_0^W \int_0^{\ell_0} \Big[\Lambda^{(1)}_{xx} + 2ik_1\Lambda^{(1)}_x + \Lambda^{(1)}_{yy} + \left(\frac{\pi}{W}\right)^2 \Lambda^{(1)} \\ + 2is(\Lambda^{(0)}_x + ik_1\Lambda^{(0)}) + ik\eta\Lambda^{(0)}\Big] \sin\left(\frac{\pi}{W}y\right) \mathrm{d}x\mathrm{d}y = 0\ .\end{aligned} \tag{A.17}$$

The first three terms should be integrated using (A.13), (A.15) and (A.16) to get rid of the derivatives of the unknown function $\Lambda^{(1)}$. The resulting terms containing $\Lambda^{(1)}$ cancel out, yielding the equation

$$\begin{aligned}0 = &\int_0^W \int_0^{\ell_0} \left[2is\left(\Lambda^{(0)}_x + ik_1\Lambda^{(0)}\right) + i\eta k_b\Lambda^{(0)}\right] \sin\left(\frac{\pi}{W}y\right) \mathrm{d}x\mathrm{d}y \\ &- \ell_1\delta \int_0^W \left[\Lambda^{(0)}_{xx}(\ell_0, y) + 2ik_1\Lambda^{(0)}_x(\ell_0, y)\right] \sin\left(\frac{\pi}{W}y\right) \mathrm{d}y \\ &- \sigma\frac{\pi}{W} \int_0^{\ell_0} \left[\Lambda^{(0)}_y(x, W)\sin\left(k_r x + \vartheta\right) + \Lambda^{(0)}_y(x, 0)\sin\left(k_r x\right)\right] \sin\left(\frac{\pi}{W}y\right) \mathrm{d}x\ .\end{aligned} \tag{A.18}$$

Then, using the explicit form of $\Lambda^{(0)}$ from (A.8) and of ℓ_0 and ℓ_1 from (A.14) yields, dropping a common factor of $k_r/\left(2\pi W k_1\right)$,

$$\left(\frac{i\eta}{2}\frac{k}{k_1} - s\right) a_1 + i\frac{\sigma}{k_1}(e^{i\vartheta} + 1)\frac{\pi^2}{W^3}\, a_2 = 0\ . \tag{A.19}$$

A similar integration using the factor $\sin\left(\frac{2\pi}{W}y\right) e^{ik_r x}$ instead of $\sin\left(\frac{\pi}{W}y\right)$ in Eq. (A.17), yields

$$-i\frac{\sigma}{k_2}(e^{-i\vartheta} + 1)\frac{\pi^2}{W^3}\, a_1 + \left(\delta + i\frac{\eta}{2}\frac{k}{k_2} - s\right) a_2 = 0\ . \tag{A.20}$$

A nontrivial solution (a_1, a_2) of system (A.19) and (A.20) exists if and only if the determinant vanishes, i.e.,

$$\left(s - i\frac{\eta}{2}\frac{k}{k_1}\right)\left(s - \delta - i\frac{\eta}{2}\frac{k}{k_2}\right) - \frac{2\pi^4}{W^6}\frac{\sigma^2}{k_1 k_2}\left(1 + \cos\vartheta\right) = 0\ . \tag{A.21}$$

The roots s of this equation and the corresponding solution (a_1, a_2) determine the corrections to the Bloch modes in Eqs. (A.4), (A.8) and (A.9). Note that, in the absence of dissipation, $\eta = 0$, our analysis fully reproduces the results obtained in Ref. [117].

A.4 Effective 2×2 model

In the next step, we derive the effective two-level Schrödinger equation corresponding to the propagation of the two nearly resonant Bloch modes. For this purpose, we write the solution (A.4) given by (A.8) and (A.9) as

$$\begin{aligned} \phi(x,y) &\approx \left(a_1 \sin\left(\frac{\pi}{W}y\right) + a_2 \sin\left(\frac{2\pi}{W}y\right) e^{-ik_r x}\right) e^{i(k_1+s)x} \\ &= \frac{c_1(x)}{\sqrt{k_1}} \sin\left(\frac{\pi}{W}y\right) + \frac{c_2(x)}{\sqrt{k_2}} \sin\left(\frac{2\pi}{W}y\right) e^{-ik_r x} , \end{aligned} \tag{A.22}$$

where

$$\begin{aligned} c_1(x) &= a_1\sqrt{k_1} e^{-i(\pi-\vartheta)/4} e^{-i(\delta-s)x} , \\ c_2(x) &= a_2\sqrt{k_2} e^{i(\pi-\vartheta)/4} e^{-i(\delta-s)x} , \end{aligned} \tag{A.23}$$

satisfy the Schrödinger equation

$$i\frac{\partial}{\partial x}\begin{pmatrix} c_1 \\ c_2 \end{pmatrix} = H \begin{pmatrix} c_1 \\ c_2 \end{pmatrix} , \quad H = \begin{pmatrix} \delta - i\frac{\eta}{2}\frac{k}{k_1} & B\sigma \\ B\sigma & -i\frac{\eta}{2}\frac{k}{k_2} \end{pmatrix} , \tag{A.24}$$

with

$$B = \sqrt{2\left(1+\cos\vartheta\right)}\frac{\pi^2}{W^3}\frac{1}{\sqrt{k_1 k_2}} . \tag{A.25}$$

The eigenvalue E of the Hamiltonian (A.24) is related to the Bloch wavenumber K via Eq. (A.23) and Eqs. (A.5), (A.6) and (A.9) as

$$E = \delta - s = \delta + k_1 - K = k_b + k_2 - K . \tag{A.26}$$

A.5 Non-uniform absorption

So far, we have considered a uniform dissipation with a constant parameter η. To engineer the waveguide's mode-dependent transmission such that one mode suffers large loss, while the other mode propagates (approximately) undamped, we now extend the model to allow absorption that is distributed non-uniformly along the waveguide.

Manipulating loss in a waveguide design implies, however, that the loss parameter is position-dependent, $\eta = \eta(x, y)$. In order to keep the Floquet-Bloch formalism valid, we consider periodic losses with the period of the boundary modulation $\ell = 2\pi/k_b$, i.e.,

$$\eta = \eta_0 \tilde{\eta}(x, y), \quad \tilde{\eta}(x + \ell, y) = \tilde{\eta}(x, y) \;, \tag{A.27}$$

where $\tilde{\eta}(x, y)$ is a given function describing the loss distribution and the real parameter η_0 controls the loss intensity. Performing the derivation as for uniform absorption, integrals of the form

$$\Gamma_{nm} = \frac{1}{\pi W} \frac{k k_b}{\sqrt{k_n k_m}} \int_0^\ell \int_0^W \tilde{\eta}(x, y) \sin\left(\frac{n\pi}{W} y\right) \sin\left(\frac{m\pi}{W} y\right) e^{-i(k_n - k_m)x} \mathrm{d}x \mathrm{d}y \tag{A.28}$$

now appear, leading to the Hamiltonian

$$H = \begin{pmatrix} \delta & B\sigma \\ B\sigma & 0 \end{pmatrix} - i\frac{\eta_0}{2} \begin{pmatrix} \Gamma_{11} & \Gamma_{12} \\ \Gamma_{12}^* & \Gamma_{22} \end{pmatrix} . \tag{A.29}$$

Note that we have changed the integration limit from ℓ_0 to ℓ and k_r to k_b in Eq. (A.28), which is justified within a first order perturbation approach, taking into account the exact period of the boundary modulation. In case of constant losses, i.e., $\tilde{\eta}(x, y) = 1$, we obtain $\Gamma_{n \neq m} = 0$ and $\Gamma_{nn} = \frac{k}{k_n}$, returning to Eq. (A.24).

A very efficient way to engineer the mode-specific absorption is to choose its spatial distribution according to the Hermitian dyadic product $v_2 v_2^\dagger$. Here, v_2 is one of the two eigenvectors of the system in the absence of absorption, with eigenvalue E_2, i.e.,

$$H_0 v_2 = E_2 v_2 \;, \quad H_0 = \begin{pmatrix} \delta & B\sigma \\ B\sigma & 0 \end{pmatrix} . \tag{A.30}$$

Introducing the composite Hamiltonian,

$$H = H_0 - i\frac{\eta}{2} v_2 v_2^\dagger \;, \tag{A.31}$$

with the anti-Hermitian dissipative term $-i\frac{\eta}{2} v_2 v_2^\dagger$, one can see that the first eigenstate v_1 does not dissipate at all due to the orthogonality condition $v_2^\dagger v_1 =$

0, in contrast to the second eigenstate v_2 leading to a decay rate $\propto \exp\left(-\frac{\eta}{2}x\right)$. In fact, this procedure is the optimal way in which a dissipation asymmetry for a 2-mode system can be introduced.

While the dyadic form of Γ_{nm} for the losses in the effective 2×2 description is very efficient, the practical demands of the experiment (like a finite extent of the absorber elements) require the use of Eq. (A.28) for the description of this scenario. To achieve a similar efficiency in the case of these finite absorbers, the elements are concentrated directlyj at the nodes of the second mode. A modified version of this approach is also implemented in the experimental microwave setup (see Fig. 3a,b in the main text and section 3.2.4 below).

A.6 EP structure

The Hamiltonian in Eq. (2.1) presented in the main text is obtained from Eq. (A.24) by identifying $g = B\sigma$ and $\gamma_n = \eta k/k_n$, $n = 1, 2$. In terms of η, k and k_n, it possesses the eigenvalue spectrum

$$E_{1,2} = \frac{\delta}{2} - i\frac{\eta}{4}\left(\frac{k}{k_1} + \frac{k}{k_2}\right) \pm \frac{1}{2}\sqrt{\Delta}\,, \quad \Delta \equiv \left(\delta - i\frac{\eta}{2}\left(\frac{k}{k_1} - \frac{k}{k_2}\right)\right)^2 + 4g^2\,. \tag{A.32}$$

The degenerate state $E_1 = E_2$ appears when both the real and imaginary part of Δ vanish simultaneously, yielding

$$g_{\mathrm{EP}} = \pm\frac{\eta}{4}\left|\frac{k}{k_1} - \frac{k}{k_2}\right|\,, \quad \delta_{\mathrm{EP}} = 0\,. \tag{A.33}$$

Therefore, in the first approximation, the EP degeneracy appears for the waveguide with periodic boundary of amplitude $\sigma = g_{\mathrm{EP}}/B$ and resonant wavenumber $k_b = k_r$.

APPENDIX B

Transitionless quantum driving

B.1 Effective model

We start with the effective Schrödinger equation

$$i\dot{\psi} = H_0\psi \ , \quad \dot{} \equiv \partial_x \ , \tag{B.1}$$

$$H_0 = \begin{pmatrix} \delta & e^{-i\phi(\vartheta)}|B(\vartheta)|\sigma(x) \\ e^{i\phi(\vartheta)}|B(\vartheta)|\sigma(x) & 0 \end{pmatrix} \ , \tag{B.2}$$

with $|B(\alpha)| = \sqrt{2\left(1+\cos\vartheta\right)}\frac{\pi^2}{W^3}\frac{1}{\sqrt{k_1k_2}}$ and $\phi(\alpha) = \mathrm{Arg}(B) = \left(\vartheta - \pi\right)/2$. For reasons that will become clearer later, we allow the off-diagonal entries to be complex numbers. In the following we will omit function arguments and include them only if necessary. Also, we choose the angle ϑ to be independent of x. With the eigenvalues given by

$$\lambda_\pm = \frac{1}{2}\left(\delta \mp \Delta\right) \ , \quad \text{with} \quad \Delta \equiv \sqrt{\delta^2 + 4|B|^2\sigma^2} \ , \tag{B.3}$$

we proceed by transforming into the (instantaneous) eigenbasis U, $\psi \to U\tilde{\psi}$, given by

$$U = \begin{pmatrix} \cos\theta/2 \; e^{-i\phi} & -\sin\theta/2 \; e^{-i\phi} \\ \sin\theta/2 & \cos\theta/2 \end{pmatrix} \ , \quad \text{with} \quad \tan\theta = 2|B|\frac{\sigma}{\delta} \ . \tag{B.4}$$

In this basis, the Schrödinger equation (B.1) reads

$$i\dot{\tilde{\psi}} = \left(U^\dagger H_0 U - iU^\dagger \dot{U}\right)\tilde{\psi}\ , \quad U^\dagger H_0 U = \begin{pmatrix} \lambda_+ & 0 \\ 0 & \lambda_- \end{pmatrix}\ , \tag{B.5}$$

describing the dynamics in the eigenframe. For the system to evolve adiabatically, the non-adiabatic contributions $-iU^\dagger\dot{U}$ have to by much smaller than the eigenvalues, $U^\dagger H_0 U$.

B.2 Transitionless quantum driving

Employing the strategy of Berry [61,62], this non-adiabatic term can be removed completely by changing the initial Hamiltonian H_0,

$$U^\dagger H_0 U \quad\rightarrow\quad U^\dagger H_0 U + iU^\dagger \dot{U}\ , \quad \text{i.e.}\ , \tag{B.6}$$

$$H_0 \quad\rightarrow\quad H_0 + H_1\ , \tag{B.7}$$

with

$$H_1 \equiv i\dot{U}U^\dagger = i\frac{\dot{\theta}}{2}\begin{pmatrix} 0 & -e^{-i\phi} \\ e^{i\phi} & 0 \end{pmatrix}\ , \quad \dot{\theta} = 2|B|\,\frac{\left(\delta\dot{\sigma} - \dot{\delta}\sigma\right)}{(\delta^2 + 4|B|^2\sigma^2)}\ . \tag{B.8}$$

Substituting H_0 with expression Eqn. (B.7), we have in the original basis

$$i\dot{\psi} = \begin{pmatrix} -k_1 & e^{-i\phi}\left(|B|\sigma - i\dot{\theta}/2\right) \\ e^{i\phi}\left(|B|\sigma + i\dot{\theta}/2\right) & -k_1 - \delta \end{pmatrix}\psi, \tag{B.9}$$

yielding the exact adiabatic dynamics in the eigenbasis U,

$$i\dot{\tilde{\psi}} = U^\dagger H_0 U\tilde{\psi} = \begin{pmatrix} \lambda_+ & 0 \\ 0 & \lambda_- \end{pmatrix}\tilde{\psi}\ . \tag{B.10}$$

B.3 Implementation

The question now is if the resulting Hamiltonian $H = H_0 + H_1$ is physical and can be realized in the waveguide system considered in this thesis. We thus have to incorporate additional terms into the off-diagonals, and have to compare this to a Hamiltonian with unknown parameters, i.e., the oscillation amplitude σ', detuning δ' and boundary phase shift ϑ':

$$\begin{pmatrix} \delta & |B(\vartheta)|\sigma - i\frac{\dot{\theta}}{2} \\ |B(\vartheta)|\sigma + i\frac{\dot{\theta}}{2} & 0 \end{pmatrix} \overset{!}{=} \begin{pmatrix} \delta' & e^{-i\phi(\vartheta')}|B(\vartheta')|\sigma' \\ e^{i\phi(\vartheta')}|B(\vartheta')|\sigma' & 0 \end{pmatrix}, \tag{B.11}$$

i.e., we require $|B(\vartheta')|\sigma' + i\frac{\dot{\theta}}{2} \overset{!}{=} e^{i\phi(\vartheta)}|B(\vartheta)|\sigma$. Note that here we have transferred the phase of the off-diagonals on the right hand side into the state ψ (see section A.4). This equation can readily be solved for the unknown quantities σ', δ' and ϑ', yielding

$$\begin{aligned} \vartheta' &= \arctan\left(\frac{\dot{\theta}}{2|B(\vartheta)|\sigma}\right), \\ \delta' &= \delta, \\ \sigma' &= \frac{\sqrt{4|B(\vartheta)|^2\sigma^2 + \dot{\theta}^2}}{2|B(\vartheta')|}. \end{aligned} \tag{B.12}$$

Since both σ' and ϑ' depend on $\sigma = \sigma(x)$ and $\delta = \delta(x)$ through $\dot{\theta} = \dot{\theta}\left(\sigma(x), \delta(x)\right)$, now not only the oscillation amplitude, but also the relative boundary phase varies with x.

APPENDIX C

Square-gradient scattering from step boundaries

C.1 Step-profile $\xi(x)$

In order to describe an effective smoothing of a step-like waveguide boundary due to a finite resolution capacity of the propagating wave, we consider a profile $\xi(x)$ which consists of $2N+1$ steps of width Δ and random heights α_n that feature zero mean and unit variance,

$$\xi(x) = \sum_{n=-N}^{N} \alpha_n \, \Pi_\rho(x - n\Delta) \; . \tag{C.1}$$

The smoothing of the steps is modelled by assuming $\Pi_\rho(x)$ to be the sum of two Fermi-functions $F_\rho(x)$,

$$\Pi_\rho(x) = F_\rho(x-\Delta) - F_\rho(x) = \frac{1}{1+e^{(x-\Delta)/\rho}} - \frac{1}{1+e^{x/\rho}} \; , \tag{C.2}$$

with the parameter ρ controlling the smearing of the steps, corresponding to the finite resolution of the propagating wave. In the limit of $\rho \to 0$, i.e., if we assume perfect resolution, the unit box function $\Theta(x) - \Theta(x-\Delta)$ is obtained (see figure C.1).

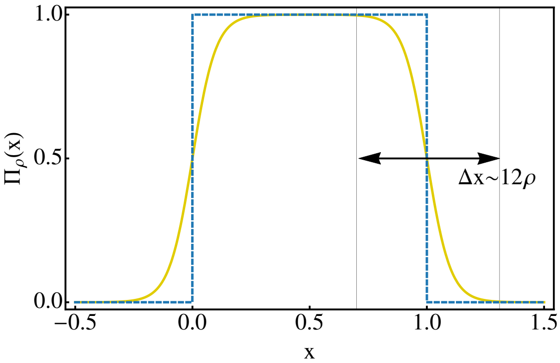

Figure C.1: Plot of the smoothed step-function $\Pi_\rho(x)$ which represents the building block for the waveguide boundaries employed in the present paper. A comparison of $\Pi_{\rho=0.05}(x)$ (yellow solid line) and $\Pi_{\rho=0}(x)$ (blue dashed line) is shown, with step-width $\Delta = 1$. The smeared out region $\Delta x \sim 12\rho$ used in the estimate in section 4.3 is indicated by grey vertical lines, as determined by the condition $|\Pi_\rho(\Delta \pm 6\rho) - \Pi_0(\Delta \pm 6\rho)| \sim 2.5 \times 10^{-3}$.

C.2 Roughness-height power spectrum $W(k)$

To calculate $W(k) = \int_{-\infty}^{\infty} \exp(-ikx')\langle\xi(x)\xi(x+x')\rangle dx'$, we employ the Wiener-Khinchin theorem [109],

$$\int_{-\infty}^{\infty} e^{-ikx'}\langle f(x)f(x+x')\rangle dx' = \lim_{L\to\infty}\frac{1}{L}\left\langle\left|\tilde{f}_{L/2}(k)\right|^2\right\rangle , \tag{C.3}$$

where $\tilde{f}_{L/2}(k)$ denotes the truncated Fourier transform,

$$\tilde{f}_{L/2}(k) \equiv \int_{-L/2}^{L/2} e^{-ikx} f(x)dx , \tag{C.4}$$

which in the limit of $L \to \infty$ becomes the Fourier transform $\tilde{f}(k) \equiv \int_{-\infty}^{\infty} \exp(-ikx)f(x)dx$. The angular brackets $\langle\cdots\rangle$ denote ensemble averaging. For our step-profile $\xi(x)$ we obtain the following expressions,

$$\begin{aligned}\tilde{\xi}_{L/2}(k) &= \sum_{n=-N}^{N} \alpha_n \int_{-L/2}^{L/2} \Pi_\rho(x-n\Delta)e^{-ikx}dx \\ &= \sum_{n=-N}^{N} \alpha_n e^{-ikn\Delta} \int_{-L/2-n\Delta}^{L/2-n\Delta} \Pi_\rho(x)e^{-ikx}dx .\end{aligned} \tag{C.5}$$

In our numerics we employ a constant number of modules but allow for a varying module width Δ, the waveguide length L is thus given by $L = 2N\Delta$. Equation (C.5) therefore reads

$$\begin{aligned}\tilde{\xi}_{L/2}(k) &= \sum_{n=-N}^{N} \alpha_n e^{-ikn\Delta} \int_{-(N+n)\Delta}^{(N-n)\Delta} \Pi_\rho(x) e^{-ikx} dx &\text{(C.6)}\\ &\approx \sum_{n=-N}^{N} \alpha_n e^{-ikn\Delta} \underbrace{\int_{-\infty}^{\infty} \Pi_\rho(x) e^{-ikx} dx}_{\tilde{\Pi}_\rho(k)} = \tilde{\Pi}_\rho(k) \sum_{n=-N}^{N} \alpha_n e^{-ikn\Delta}\,. &\text{(C.7)}\end{aligned}$$

Here, we approximate the truncated Fourier transform in equation (C.6) with $\tilde{\Pi}_\rho(k)$, such that it is independent of the summation index n and can thus be pulled it in front of the summation. For the parameters employed in the present paper this step is very well justified and only leads to a vanishingly small error.

The roughness-height power spectrum $W(k) = \lim_{L\to\infty} \frac{1}{L}\langle|\tilde{\xi}_{L/2}(k)|^2\rangle$ consequently becomes

$$\begin{aligned}W(k) &= \lim_{N\to\infty} \frac{1}{2N\Delta} \left\langle \left| \tilde{\Pi}_\rho(k) \sum_{n=-N}^{N} \alpha_n e^{-ikn\Delta} \right|^2 \right\rangle \\ &= \frac{|\tilde{\Pi}_\rho(k)|^2}{\Delta} \lim_{N\to\infty} \frac{1}{2N} \sum_{n=-N}^{N} \sum_{m=-N}^{N} \underbrace{\langle \alpha_n \alpha_m \rangle}_{\alpha_n^2 \delta_{nm}} e^{-ik(n-m)\Delta} \\ &= \frac{|\tilde{\Pi}_\rho(k)|^2}{\Delta} \lim_{N\to\infty} \frac{1}{2N} \sum_{n=-N}^{N} \alpha_n^2 = \frac{1}{\Delta} |\tilde{\Pi}_\rho(k)|^2. &\text{(C.8)}\end{aligned}$$

Note that we assume here that the random heights are uncorrelated, i.e., the products $\langle\alpha_n\alpha_m\rangle$ vanish for $n \neq m$. The expression $\tilde{\Pi}_\rho(k)$ can be calculated analytically,

$$\begin{aligned}\tilde{\Pi}_\rho(k) &= \int_{-\infty}^{\infty} e^{-ikx} \left(F_\rho(x-\Delta) - F_\rho(x)\right) dx \\ &= \underbrace{\tilde{F}_\rho(k)}_{\left(i\frac{\pi\rho}{\sinh(\pi k\rho)} + \pi\delta(k)\right)} \cdot \underbrace{\left(e^{-ik\Delta} - 1\right)}_{\left(-2ie^{-ik\Delta/2}\sin(k\Delta/2)\right)}\,. &\text{(C.9)}\end{aligned}$$

Since we evaluate $W(k)$ at finite k values we omit the delta function $\delta(k)$ in the following, yielding finally

$$W(k) = \frac{1}{\Delta} \frac{4\pi^2\rho^2}{\sinh^2(\pi k\rho)} \sin^2(k\Delta/2)\,. \qquad \text{(C.10)}$$

C.3 Square-gradient power spectrum $S(k)$

For the squared gradient of $\xi(x)$ we have

$$\xi'(x)^2 = \sum_{n=-N}^{N} \sum_{m=-N}^{N} \alpha_n \alpha_m \Pi'_\rho(x - n\Delta)\Pi'_\rho(x - m\Delta) \; . \tag{C.11}$$

Under the assumption that the smearing parameter ρ fulfils the relation $\rho \lesssim \Delta/12$, the product $\Pi'_\rho(x - n\Delta)\Pi'_\rho(x - m\Delta)$ is only finite if $n = m$, $n = m + 1$ and $n = m - 1$, respectively, i.e.,

$$\begin{aligned}\Pi'_\rho(x - n\Delta)\Pi'_\rho(x - m\Delta) \;\; \approx \;\; & \delta_{n,m} F'_\rho\Big(x - (n+1)\Delta\Big) F'_\rho\Big(x - (m+1)\Delta\Big) \\ & + \delta_{n,m} F'_\rho\Big(x - n\Delta\Big) F'_\rho\Big(x - m\Delta\Big) \\ & -\delta_{n-1,m} F'_\rho\left(x - n\Delta\right) F'_\rho\Big(x - (m+1)\Delta\Big) \\ & -\delta_{n+1,m} F'_\rho\Big(x - (n+1)\Delta\Big) F'_\rho\left(x - m\Delta\right) \; ,\end{aligned} \tag{C.12}$$

resulting in

$$\begin{aligned}\xi'(x)^2 \;\; \approx \;\; & \sum_{n=-N}^{N} \alpha_n^2 \Big[F'^2_\rho\left(x - (n+1)\Delta\right) + F'^2_\rho\left(x - n\Delta\right) \Big] \\ & -\alpha_n\alpha_{n+1} F'^2_\rho\left(x - (n+1)\Delta\right) - \alpha_n\alpha_{n-1} F'^2_\rho\left(x - n\Delta\right) \; .\end{aligned} \tag{C.13}$$

To calculate the square-gradient power spectrum $S(k)$ we have, with $V(x) = \xi'^2(x) - \langle \xi'^2(x) \rangle$,

$$\begin{aligned} S(k) \;\; &= \;\; \frac{1}{2}\int_{-\infty}^{\infty} e^{-ikx'} \langle V(x)V(x + x')\rangle dx' \\ &= \;\; \frac{1}{2}\int_{-\infty}^{\infty} e^{-ikx'} \langle \xi'^2(x)\xi'^2(x + x')\rangle dx' - \pi\langle \xi'^2(x)\rangle^2 \delta(k) \; , \end{aligned} \tag{C.14}$$

where we again employ the Wiener-Khinchin theorem equation (C.3). Identifying $\xi'^2(x)$ with $f(x)$, we have

$$\begin{aligned} \tilde{f}(k) \;\; &= \;\; \int_{-\infty}^{\infty} e^{-ikx} \xi'^2(x) dx \\ &= \;\; \underbrace{\int_{-\infty}^{\infty} e^{-ikx} F'^2_\rho(x) dx}_{\frac{1}{6}k\pi\frac{(1+k^2\rho^2)}{\sinh(\pi k\rho)}} \sum_{n=-N}^{N} e^{-ikn\Delta} \left[\alpha_n^2 \left(1 + e^{-ik\Delta}\right) - \alpha_n\alpha_{n+1} e^{-ik\Delta} - \alpha_n\alpha_{n-1} \right] \end{aligned} \tag{C.15}$$

In analogy to the reasoning for equation (C.10), we neglect the additional contribution at $k = 0$. The square-gradient roughness spectrum $S(k) = \lim_{L\to\infty} \frac{1}{L}\langle|\tilde{f}_{L/2}(k)|^2\rangle$ thus becomes

$$S(k) = \frac{1}{\Delta}\frac{k^2\pi^2}{72}\frac{(1+k^2\rho^2)^2}{\sinh^2(\pi k\rho)}\Omega(k\Delta)\ , \tag{C.16}$$

with the auxiliary function $\Omega(x)$,

$$\begin{aligned}\Omega(x) &= \lim_{N\to\infty}\frac{1}{2N}\left\langle\left|\sum_{n=-N}^{N} e^{-inx}\left[\alpha_n^2\left(1+e^{-ix}\right) - \alpha_n\alpha_{n+1}e^{-ix} - \alpha_n\alpha_{n-1}\right]\right|^2\right\rangle \\ &= \lim_{N\to\infty}\left[\frac{4}{5}\left(1+\frac{1}{2N}\right)\left(7+2\cos(x)\right) + 2\left(1+\cos(x)\right)\frac{1}{2N}\frac{\sin^2\left[(N+\frac{1}{2})x\right]}{\sin^2(x/2)}\right]\ .\end{aligned} \tag{C.17}$$

Bibliography

[1] Klaiman, S., Günther, U. & Moiseyev, N. Visualization of branch points in PT-symmetric waveguides. *Physical Review Letters* **101**, 080402 (2008).

[2] Rüter, C. E. *et al.* Observation of parity – time symmetry in optics. *Nature Physics* **6**, 192–195 (2010).

[3] Xu, X.-W., Liu, Y.-x., Sun, C.-P. & Li, Y. Mechanical PT symmetry in coupled optomechanical systems. *Physical Review A* **92**, 013852 (2015).

[4] Moiseyev, N. *Non-Hermitian quantum mechanics* (Cambridge University Press, Cambridge; New York, 2011).

[5] Liertzer, M. *et al.* Pump-Induced Exceptional Points in Lasers. *Physical Review Letters* **108**, 173901 (2012).

[6] Brandstetter, M. *et al.* Reversing the pump dependence of a laser at an exceptional point. *Nature communications* **5**, 4034 (2014).

[7] Guo, A. *et al.* Observation of PT-symmetry breaking in complex optical potentials. *Physical Review Letters* **103**, 093902 (2009).

[8] Lin, Z. *et al.* Unidirectional invisibility induced by PT-symmetric periodic structures. *Physical Review Letters* **106**, 213901 (2011).

[9] Berry, M. V. Physics of nonhermitian degeneracies. *Czechoslovak Journal of Physics* **54**, 1039–1047 (2004).

[10] Rotter, I. A non-Hermitian Hamilton operator and the physics of open quantum systems. *Journal of Physics A: Mathematical and Theoretical* **42**, 153001 (2009).

[11] Heiss, W. D. The physics of exceptional points. *Journal of Physics A: Mathematical and Theoretical* **45**, 444016 (2012).

[12] Born, M. & Fock, V. Beweis des Adiabatensatzes. *Zeitschrift für Physik* **51**, 165–180 (1928).

[13] Latinne, O. *et al.* Laser-induced degeneracies involving autoionizing states in complex atoms. *Physical Review Letters* **74**, 46–49 (1995).

[14] Lefebvre, R., Atabek, O., Šindelka, M. & Moiseyev, N. Resonance coalescence in molecular photodissociation. *Physical Review Letters* **103**, 123003–123003 (2009).

[15] Atabek, O. *et al.* Proposal for a laser control of vibrational cooling in Na2 using resonance coalescence. *Physical Review Letters* **106**, 173002 (2011).

[16] Kvitsinsky, A. & Putterman, S. Adiabatic evolution of an irreversible two level system. *Journal of Mathematical Physics* **32**, 1403–1407 (1991).

[17] Uzdin, R., Mailybaev, A. A. & Moiseyev, N. On the observability and asymmetry of adiabatic state flips generated by exceptional points. *Journal of Physics A: Mathematical and Theoretical* **44**, 435302 (2011).

[18] Graefe, E. M., Mailybaev, A. A. & Moiseyev, N. Breakdown of adiabatic transfer of light in waveguides in the presence of absorption. *Physical Review A* **88**, 033842 (2013).

[19] Gilary, I., Mailybaev, A. A. & Moiseyev, N. Time-asymmetric quantum-state-exchange mechanism. *Physical Review A* **88**, 010102 (2013).

[20] Leclerc, A., Jolicard, G. & Killingbeck, J. P. Discussion of the adiabatic hypothesis in control schemes using exceptional points. *Journal of Physics B: Atomic, Molecular and Optical Physics* **46**, 145503 (2013).

[21] Kaprálová-Žďánská, P. R. & Moiseyev, N. Helium in chirped laser fields as a time-asymmetric atomic switch. *The Journal of Chemical Physics* **141**, 014307 (2014).

[22] Dembowski, C. *et al.* Encircling an exceptional point. *Physical Review E* **69**, 056216 (2004).

[23] Gao, T. *et al.* Observation of non-Hermitian degeneracies in a chaotic exciton-polariton billiard. *Nature* **526**, 554–558 (2015).

[24] Feist, J., Bäcker, A., Ketzmerick, R., Burgdörfer, J. & Rotter, S. Nanowires with surface disorder: Giant localization length and dynamical tunneling in the presence of directed chaos. *Physical Review B* **80** (2009).

[25] Feilhauer, J. & Moško, M. Coexistence of diffusive resistance and ballistic persistent current in disordered metallic rings with rough edges: Possible origin of puzzling experimental values. *Physical Review B* **88** (2013).

[26] Garcıá-Martıń, A., Torres, J. A., Sáenz, J. J. & Nieto-Vesperinas, M. Transition from diffusive to localized regimes in surface corrugated optical waveguides. *Applied Physics Letters* **71**, 1912 (1997).

[27] García-Martín, A., Governale, M. & Wölfle, P. Magnetic-field effects on the transport properties of one-sided rough wires. *Physical Review B* **66**, 233307 (2002).

[28] Doppler, J. *et al.* Reflection resonances in surface-disordered waveguides: strong higher-order effects of the disorder. *New Journal of Physics* **16**, 053026 (2014).

[29] Dietz, O. *et al.* Surface scattering and band gaps in rough waveguides and nanowires. *Physical Review B* **86**, 201106(R) (2012).

[30] Bender, C. Making sense of non-Hermitian Hamiltonians. *Rep. Prog. Phys* **947** (2007).

[31] Cao, H. & Wiersig, J. Dielectric microcavities: Model systems for wave chaos and non-Hermitian physics. *Reviews of Modern Physics* **87**, 61–111 (2015).

[32] Regensburger, A. *et al.* Parity–time synthetic photonic lattices. *Nature* **488**, 167–171 (2012).

[33] Feng, L. *et al.* Experimental demonstration of a unidirectional reflectionless parity-time metamaterial at optical frequencies. *Nature Materials* **12**, 108–113 (2013).

[34] Feng, L. *et al.* Demonstration of a large-scale optical exceptional point structure. *Optics Express* **22**, 1760–1760 (2013).

[35] Peng, B. *et al.* Loss-induced suppression and revival of lasing. *Science* **346**, 328–332 (2014).

[36] Feng, L., Wong, Z. J., Ma, R.-M., Wang, Y. & Zhang, X. Single-mode laser by parity-time symmetry breaking. *Science* **346**, 972–975 (2014).

[37] Hodaei, H., Miri, M.-A., Heinrich, M., Christodoulides, D. N. & Khajavikhan, M. Parity-time–symmetric microring lasers. *Science* **346**, 975–978 (2014).

[38] Dridi, G., Guérin, S., Jauslin, H. R., Viennot, D. & Jolicard, G. Adiabatic approximation for quantum dissipative systems: Formulation, topology, and superadiabatic tracking. *Physical Review A* **82**, 022109 (2010).

[39] Berry, M. V. Optical polarization evolution near a non-Hermitian degeneracy. *Journal of Optics* **13**, 115701 (2011).

[40] Berry, M. V. & Uzdin, R. Slow non-Hermitian cycling: exact solutions and the Stokes phenomenon. *Journal of Physics A: Mathematical and Theoretical* **44**, 435303 (2011).

[41] Milburn, T. J. *et al.* General description of quasiadiabatic dynamical phenomena near exceptional points. *Physical Review A* **92**, 052124 (2015).

[42] Menke, H., Klett, M., Cartarius, H., Main, J. & Wunner, G. State flip at exceptional points in atomic spectra. *Physical Review A* **93**, 013401 (2016).

[43] Kato, T. *Perturbation Theory for Linear Operators* (Springer, Berlin, 1966).

[44] Heiss, W. D. Exceptional points of non-Hermitian operators. *Journal of Physics A: Mathematical and General* **37**, 2455–2464 (2004).

[45] Demange, G. & Graefe, E.-M. Signatures of three coalescing eigenfunctions. *Journal of Physics A: Mathematical and Theoretical* **45**, 025303 (2012).

[46] Keck, F., Korsch, H. J. & Mossmann, S. Unfolding a diabolic point: a generalized crossing scenario. *Journal of Physics A: Mathematical and General* **36**, 2125 (2003).

[47] Mailybaev, A. A., Kirillov, O. N. & Seyranian, A. P. Geometric phase around exceptional points. *Physical Review A* **72**, 014104 (2005).

[48] Berglund, N. & Gentz, B. *Noise-induced phenomena in slow-fast dynamical systems a sample-paths approach* (Springer, London, 2006).

[49] Neishtadt, A. On stability loss delay for dynamical bifurcations. *Discrete and Continuous Dynamical Systems - Series S* **2**, 897–909 (2009).

[50] Dembowski, C. *et al.* Experimental observation of the topological structure of exceptional points. *Physical Review Letters* **86**, 787–790 (2001).

[51] Lee, S.-B. *et al.* Observation of an exceptional point in a chaotic optical microcavity. *Physical Review Letters* **103**, 134101 (2009).

[52] Doppler, J. *et al.* Dynamically encircling exceptional points in a waveguide: asymmetric mode switching from the breakdown of adiabaticity (currently under review, 2016).

[53] Allen, L. & Eberly, J. H. *Optical resonance and two-level atoms* (Dover, New York, 1987).

[54] Arnold, V. I. *Catastrophe Theory* (Springer, Berlin, Heidelberg, 1992).

[55] Suominem, K.-A. & Garraway, B. Population transfer in a level-crossing model with two time scales. *Physical Review A* **45**, 375–386 (1992).

[56] Malinovsky, V. S. & Krause, J. L. General theory of population transfer by adiabatic rapid passage with intense, chirped laser pulses. *The European Physical Journal D-Atomic, Molecular, Optical and Plasma Physics* **14**, 147–155 (2001).

[57] Seyranian, A. P., Kirillov, O. N. & Mailybaev, A. A. Coupling of eigenvalues of complex matrices at diabolic and exceptional points. *Journal of Physics A: Mathematical and General* **38**, 1723 (2005).

[58] Rotter, S., Weingartner, B., Rohringer, N. & Burgdörfer, J. Ballistic quantum transport at high energies and high magnetic fields. *Physical Review B* **68** (2003).

[59] Libisch, F., Rotter, S. & Burgdörfer, J. Coherent transport through graphene nanoribbons in the presence of edge disorder. *New Journal of Physics* **14**, 123006 (2012).

[60] Storn, R. & Price, K. Differential Evolution – A Simple and Efficient Heuristic for global Optimization over Continuous Spaces. *Journal of Global Optimization* **11**, 341–359 (1997).

[61] Berry, M. V. Transitionless quantum driving. *Journal of Physics A: Mathematical and Theoretical* **42**, 365303 (2009).

[62] Chen, X., Lizuain, I., Ruschhaupt, A., Guéry-Odelin, D. & Muga, J. G. Shortcut to adiabatic passage in two- and three-level atoms. *Physical Review Letters* **105**, 123003 (2010).

[63] Paul, K. & Sarma, A. K. Shortcut to adiabatic passage in a waveguide coupler with a complex-hyperbolic-secant scheme. *Physical Review A* **91**, 053406 (2015).

[64] Dietz, O., Kuhl, U., Stöckmann, H.-J., Makarov, N. M. & Izrailev, F. M. Microwave realization of quasi-one-dimensional systems with correlated disorder. *Physical Review B* **83**, 134203 (2011).

[65] Feng, L. *et al.* Nonreciprocal light propagation in a silicon photonic circuit. *Science* **333**, 729–733 (2011).

[66] Baets, R., Freude, W., Melloni, A., Popović, M. & Vanwolleghem, M. Comment to "Nonreciprocal Light Propagation in a Silicon Photonic Circuit". *arXiv:1110.2647 [physics]* (2011).

[67] Petrov, A. *et al.* Comment on "Nonreciprocal Light Propagation in a Silicon Photonic Circuit" in Science 333, 729-733 (2011). *arXiv:1110.5748 [physics]* (2011).

[68] Yu, Z., Joannopoulos, J. D. & Fan, S. Is one-way modal conversion sufficient for optical isolation? *arXiv:1110.4140 [physics]* (2011).

[69] Fan, S. *et al.* Comment on "Nonreciprocal light propagation in a silicon photonic circuit". *Science* **335**, 38–38 (2012).

[70] Jalas, D. *et al.* What is — and what is not — an optical isolator. *Nature Photonics* **7**, 579–582 (2013).

[71] Wolf, E. & DeSanto, J. A. *Progress in optics*, vol. 23 (North-Holland, Amsterdam, 1986).

[72] Bass, F. G. & Fuks, I. M. *Wave scattering from statistically rough surfaces.* No. v. 93 in International series in natural philosophy (Pergamon Press, Oxford; New York, 1979).

[73] Maradudin, A. A. & Lockwood, D. J. (eds.) *Light Scattering and Nanoscale Surface Roughness.* Nanostructure Science and Technology (Springer, Boston, 2007).

[74] Tsang, L. & Kong, J. A. *Scattering of electromagnetic waves. Advanced topics.* Wiley series in remote sensing (Wiley, New York, 2001).

[75] Medwin, H. & Clay, C. S. *Fundamentals of acoustical oceanography.* Applications of modern acoustics (Academic Press, Boston, 1998).

[76] Li, C., Kattawar, G. W. & Yang, P. Effects of surface roughness on light scattering by small particles. *Journal of Quantitative Spectroscopy and Radiative Transfer* **89**, 123–131 (2004).

[77] Gan, L. & Li, Z. Designs and experiments on infrared two-dimensional silicon photonic crystal slab devices. *Frontiers of Optoelectronics* **5**, 21–40 (2012).

[78] Roberts, P. J. *et al.* Loss in solid-core photonic crystal fibers due to interface roughness scattering. *Optics Express* **13**, 7779 (2005).

[79] Chaikina, E. I., Stepanov, S., Navarrete, A. G., Méndez, E. R. & Leskova, T. A. Formation of angular power profile via ballistic light transport in multimode optical fibers with corrugated surfaces. *Physical Review B* **71** (2005).

[80] Minh-Chau Phan-Huy *et al.* Surface Roughness and Light Scattering in a Small Effective Area Microstructured Fiber. *Journal of Lightwave Technology* **27**, 1597–1604 (2009).

[81] Maker, A. J. & Armani, A. M. Low-loss silica-on-silicon waveguides. *Optics Letters* **36**, 3729 (2011).

[82] Lee, K. K. *et al.* Effect of size and roughness on light transmission in a Si/SiO2 waveguide: Experiments and model. *Applied Physics Letters* **77**, 1617 (2000).

[83] Zayats, A. V., Smolyaninov, I. I. & Maradudin, A. A. Nano-optics of surface plasmon polaritons. *Physics Reports* **408**, 131–314 (2005).

[84] Maradudin, A. A. (ed.) *Structured Surfaces as Optical Metamaterials* (Cambridge University Press, Cambridge, 2011).

[85] Fishman, G. & Calecki, D. Surface-induced resistivity of ultrathin metallic films: A limit law. *Physical Review Letters* **62**, 1302–1305 (1989).

[86] Meyerovich, A. E. & Stepaniants, A. Quantized systems with randomly corrugated walls and interfaces. *Physical Review B* **60**, 9129–9144 (1999).

[87] Chopra, K. L. *Thin film phenomena* (R. E. Krieger Pub. Co, Huntington, N.Y, 1979).

[88] Makarov, N. M., Moroz, A. V. & Yampol'skii, V. A. Classical and quantum size effects in electron conductivity of films with rough boundaries. *Physical Review B* **52**, 6087–6101 (1995).

[89] Zhang, S., Levy, P. M. & Fert, A. Conductivity and magnetoresistance of magnetic multilayered structures. *Physical Review B* **45**, 8689–8702 (1992).

[90] Han, M. Y., Özyilmaz, B., Zhang, Y. & Kim, P. Energy Band-Gap Engineering of Graphene Nanoribbons. *Physical Review Letters* **98** (2007).

[91] Huber, T. E., Nikolaeva, A., Gitsu, D., Konopko, L. & Graf, M. J. Role of boundary roughness in the electronic transport of Bi nanowires. *Journal of Applied Physics* **104**, 123704 (2008).

[92] Akguc, G. B. & Gong, J. Conductance properties of rough quantum wires with colored surface disorder. *Physical Review B* **78** (2008).

[93] Feist, J. *et al.* Nanowires with Surface Disorder: Giant Localization Lengths and Quantum-to-Classical Crossover. *Physical Review Letters* **97** (2006).

[94] Ferry, D. K., Goodnick, S. M. & Bird, J. *Transport in Nanostructures* (Cambridge University Press, Cambridge, 2009), 2 edn.

[95] Freylikher, V. D., Makarov, N. M. & Yurkevich, I. V. Strong one-dimensional localization in systems with statistically rough boundaries. *Physical Review B* **41**, 8033–8036 (1990).

[96] Hochbaum, A. I. *et al.* Enhanced thermoelectric performance of rough silicon nanowires. *Nature* **451**, 163–167 (2008).

[97] Martin, P., Aksamija, Z., Pop, E. & Ravaioli, U. Impact of Phonon-Surface Roughness Scattering on Thermal Conductivity of Thin Si Nanowires. *Physical Review Letters* **102** (2009).

[98] Isabella, O., Krč, J. & Zeman, M. Modulated surface textures for enhanced light trapping in thin-film silicon solar cells. *Applied Physics Letters* **97**, 101106 (2010).

[99] Chizhova, L. A. *et al.* Vectorial velocity filter for ultracold neutrons based on a surface-disordered mirror system. *Physical Review E* **89** (2014).

[100] Sánchez-Gil, J. A., Freilikher, V., Yurkevich, I. & Maradudin, A. A. Coexistence of Ballistic Transport, Diffusion, and Localization in Surface Disordered Waveguides. *Physical Review Letters* **80**, 948–951 (1998).

[101] Sánchez-Gil, J. A., Freilikher, V., Maradudin, A. A. & Yurkevich, I. V. Reflection and transmission of waves in surface-disordered waveguides. *Physical Review B* **59**, 5915–5925 (1999).

[102] Yannopapas, V., Stefanou, N. & Modinos, A. Effect of Stacking Faults on the Optical Properties of Inverted Opals. *Physical Review Letters* **86**, 4811–4814 (2001).

[103] Beenakker, C. W. J. Random-matrix theory of quantum transport. *Reviews of Modern Physics* **69**, 731–808 (1997).

[104] Mello, P. A. & Kumar, N. *Quantum Transport in Mesoscopic Systems* (Oxford University Press, 2004).

[105] Andreev, A. V., Agam, O., Simons, B. D. & Altshuler, B. L. Quantum Chaos, Irreversible Classical Dynamics, and Random Matrix Theory. *Physical Review Letters* **76**, 3947–3950 (1996).

[106] Gornyi, I. V. & Mirlin, A. D. Wave function correlations on the ballistic scale: Exploring quantum chaos by quantum disorder. *Physical Review E* **65**, 025202(R) (2002).

[107] Izrailev, F., Makarov, N. & Rendón, M. Manifestation of the roughness-square-gradient scattering in surface-corrugated waveguides. *Physical Review B* **73**, 155421 (2006).

[108] Rendón, M., Makarov, N. M. & Izrailev, F. M. Ballistic, diffusive, and localized transport in surface-disordered systems: Two-mode waveguide. *Physical Review E* **83**, 051124 (2011).

[109] Kay, S. & Marple, S. Spectrum analysis - A modern perspective. *Proceedings of the IEEE* **69**, 1380–1419 (1981).

[110] Rotter, S., Tang, J.-Z., Wirtz, L., Trost, J. & Burgdörfer, J. Modular recursive Green's function method for ballistic quantum transport. *Physical Review B* **62**, 1950–1960 (2000).

[111] Rotter, S., Libisch, F., Burgdörfer, J., Kuhl, U. & Stöckmann, H.-J. Tunable Fano resonances in transport through microwave billiards. *Physical Review E* **69**, 046208 (2004).

[112] Rotter, S., Kuhl, U., Libisch, F., Burgdörfer, J. & Stöckmann, H.-J. Fano resonances and decoherence in transport through quantum dots. *Physica E: Low-dimensional Systems and Nanostructures* **29**, 325–333 (2005).

[113] West, C. S. & O'Donnell, K. A. Observations of backscattering enhancement from polaritons on a rough metal surface. *Journal of the Optical Society of America A* **12**, 390 (1995).

[114] Bellani, V. *et al.* Experimental Evidence of Delocalized States in Random Dimer Superlattices. *Physical Review Letters* **82**, 2159–2162 (1999).

[115] Jackson, J. D. *Classical electrodynamics* (Wiley, New York, 1999), 3rd edn.

[116] Seyranian, A. P. & Mailybaev, A. A. *Multiparameter stability theory with mechanical applications* (World Scientific, Singapore, 2003).

[117] Asfar, O. R. & Nayfeh, A. H. The Application of the Method of Multiple Scales to Wave Propagation in Periodic Structures. *SIAM Review* **25**, 455–480 (1983).

Acknowledgements

First and foremost, I would like to thank my supervisor Stefan Rotter for his trust and for encouraging me to pursue a PhD, his continued guidance, as well as for always finding the time for clarifying discussions even during very stressful times. Furthermore, I want to express my gratitude for the opportunity to carry out a research visit in Brazil, which helped me to move the EP project forward decisively.

I am also highly indebted to Alexei A. Mailybaev for his help during the many challenging stages of this thesis, his willingness to answer numerous questions at unorthodox times, and his great hospitality at the IMPA in Rio de Janeiro. Beyond the joint research, climbing the Sugar Loaf together in addition to the (sometimes brutal) hiking trips made our collaboration even more memorable.

I would also like to thank all members of the Rottergroup, especially Philipp Ambichl, Stephan Burkhardt, Adrian Girschik, Thomas Hisch and Matthias Liertzer, not only for their valuable input on science and coding matters, but also for all the non-scientific conversations and activities that made my PhD-years pleasant and rewarding on so many levels.

Special thanks go to Florian Libisch, who developed the numerical code on which most of this thesis depended on, and who was eager to help with all the code-related problems I have encountered in the course of my research. Adrian Girschik deserves a second mentioning here for his great effort on implementing (and debugging!) the many additional features in the `greens_code` that I naively requested.

Additionally, I am deeply grateful to Heike Höller and Sylvia Riedler for assisting me with all the administrative workload, and to all the additional people with whom I've had the fortune to publish with: Julian Böhm, Otto Dietz, Johannes Feist, Catherine A. Holmes, Felix M. Izrailev, Dmitry O. Krimer, Ulrich Kuhl, Nykolay M. Makarov, José A. Méndez-Bermúdez, Thomas J. Milburn, Nimrod Moiseyev, Stefano Portolan, Peter Rabl and Hans-Jürgen Stöckmann.

Finally, I want to thank my parents as well as Johanna for their support throughout my studies and during all the tough periods that emerged within the past years.

Jörg Doppler

Curriculum Vitae

Vally-Weigl-Gasse 2/3/19
1100 Vienna
Austria
☎ *+43 699 1140 7659*
✉ *joerg.doppler@gmail.com*

Education

since 07/2012 **Doctoral studies (Technical Sciences)**, *Vienna University of Technology*, Vienna, Austria.

01/2015 **Guest researcher**, *Institute for Pure and Applied Mathematics*, Rio de Janeiro, Brazil.
Invited by Prof. Alexei A. Mailybaev

2009–2012 **Master studies (Technical Physics)**, *Vienna University of Technology*, Vienna, Austria.
Graduation with distinction

2010–2011 **Exchange semester**, *Swiss Federal Institute of Technology (ETHZ)*, Zürich, Switzerland.

2006–2009 **Bachelor studies (Technical Physics)**, *Vienna University of Technology*, Vienna, Austria.
Graduation with distinction

1997–2005 **Grammar school**, *BG18 Klostergasse*, Vienna, Austria.
Graduation with distinction

Work experience

since 07/2012 **Research assistant**, *Vienna University of Technology*, Institute for Theoretical Physics, Vienna, Austria.
Supervised by Prof. Stefan Rotter

2005–2006 **Paramedic**, *Johanniter-Unfall-Hilfe*, Vienna, Austria.
Community service

2003–2007 **Assembly-line work**, *Agrana*, Tulln, Austria.
Summer jobs

Scholarships and grants

2012-2013	Participant of TUtheTOP 2012/13, the high-potential program of the Vienna UT
2011-2012	Grant of the Austrian Science Fund (FWF)
2010-2011	Achievement scholarship of the Vienna UT
2010-2011	Erasmus scholarship (ETHZ)
2008-2009	Achievement scholarship of the Vienna UT

Master thesis

title	*DFT studies of graphene intercalation systems: graphene/Ni/Ir and graphene/Ag/Re*
supervisor	Prof. Josef Redinger, Institute for Applied Physics, Vienna UT
year	2012

Publications

2016 **Dynamically encircling exceptional points in a waveguide: asymmetric mode switching from the breakdown of adiabaticity**
J. Doppler, A. A. Mailybaev, J. Böhm, U. Kuhl, A. Girschik, F. Libisch, T. J. Milburn, P. Rabl, N. Moiseyev, and Stefan Rotter (currently under review)

2015 **General dynamical description of quasi-adiabatically encircling exceptional points**
T. J. Milburn, J. Doppler, C. A. Holmes, S. Portolan, S. Rotter and P. Rabl – Phys. Rev. A **92**, 052124

2014 **Reflection resonances in surface-disordered waveguides: strong higher-order effects of the disorder**
J. Doppler, J. A. Méndez-Bermúdez, J. Feist, O. Dietz, D. O. Krimer, N. M. Makarov, F. M. Izrailev and S. Rotter – New J. Phys. **16**, 053026

2013 **Hybridization of graphene and a Ag monolayer supported on Re(0001)**
M. Papagno, P. Moras, P. M. Sheverdyaeva, J. Doppler, A. Garhofer, F. Mittendorfer, J. Redinger and C. Carbone – Phys. Rev. B **88**, 235430

An artificially lattice mismatched graphene/metal interface: graphene/Ni/Ir(111)
D. Pacilé, P. Leicht, M. Papagno, P. M. Sheverdyaeva, P. Moras, C. Carbone, K. Krausert, L. Zielke, M. Fonin, Y. S. Dedkov, F. Mittendorfer, J. Doppler, A. Garhofer and J. Redinger – Phys. Rev. B **87**, 035420

2012 **Surface scattering and band gaps in rough nanowires and waveguides**
O. Dietz, H.-J. Stöckmann, U. Kuhl, F. M. Izrailev, N. M. Makarov, J. Doppler, F. Libisch and S. Rotter – Phys. Rev. B **86**, 201106(R)

Talks and posters

07/2015 **General description of quasi-adiabatic dynamical phenomena near exceptional points**
T. J. Milburn, J. Doppler, C. A. Holmes, S. Portolan, A. Girschik, F. Libisch, A. A. Mailybaev, P. Rabl and S. Rotter – Talk at "Quantum (and Classical) Physics with Non-Hermitian Operators", Jerusalem, Israel

04/2015 **Using exceptional points to engineer the modal transmission characteristics of waveguides**
J. Doppler, A. A. Mailybaev, A. Girschik, F. Libisch, T. J. Milburn, P. Rabl and S. Rotter – Talk at the "10th IR-On Workshop", Traunkirchen, Austria

09/2013 **Quantitative description of coherent transport through surface-disordered wires**
J. Doppler, O. Dietz, J. A. Méndez-Bermúdez, J. Feist, F. Libisch, D. O. Krimer, N. M. Makarov, F. M. Izrailev, H.-J. Stöckmann, U. Kuhl and S. Rotter – Poster at "Advances in Quantum Chaotic Scattering: From (Non-)Linear Waves to Few-Body Systems", Dresden, Germany

08/2012 **Reflection resonances in waveguides with rough surface profiles: Identifying signatures of a new scattering mechanism**
J. Doppler, F. M. Izrailev, J. A. Méndez-Bermúdez, J. Feist and S. Rotter – Talk at the "8th International Workshop on Disordered Systems", Benasque, Spain

03/2012 **DFT study of the electronic structure of graphene/Ag(111)/Re(0001)**
J. Doppler, A. Garhofer, F. Mittendorfer and J. Redinger – Talk at the "Frühjahrstagung der Deutschen Physikalischen Gesellschaft", Berlin, Germany